Automated Scaling Region of Interest with Iterative Edge Preserving in Forward-Backward Time-Stepping

Juliana Binti Nawawi

A thesis submitted

In fulfilment of the requirements for the degree of Master of Engineering

(Electronics Engineering)

Faculty of Engineering
UNIVERSITI MALAYSIA SARAWAK
2019

DECLARATION

The work presented in this thesis, to the best of my knowledge and belief, original and my own work, except as acknowledged in the text. The thesis has not been accepted for any degree and is not concurrently submitted in candidature for any other degree.

Name : Juliana Binti Nawawi

Date : 16 May 2019

DEDICATION

Dedicated to my beloved parents

ACKNOWLEDGEMENT

All praises and thanks to Allah the Almighty for giving me the opportunity and strength to successfully undergone this wonderful journey pursuing my Master degree. I am blessed to be surrounded with many great people who being supportive throughout the years to complete this research work.

I would like to express my sincere and greatest gratitude to my supervisors, Dr Shafrida Sahrani and Ir Dr Kismet Ak Hong Ping for their patience, continuous guidance and valuable advises in seeking proper methods in research as well as for their encouragement while struggling with difficulties.

I am also indebted to the Applied Electromagnetic Research Group members for sharing knowledge and ideas in realizing the research possible to be implemented. Dr Ng Shi Wei and Mr. Yong Guang have helped me a lot in understanding the FBTS algorithm and code. Thanks to the former Head of the Electrical and Electronic Engineering Department, Dr Norhuzaimin Julai and Microwave Lab technicians in providing research facilities to acquire data for analysis.

Finally, special thanks go to my mother and late father for their unconditional love, constant prayers, unstinted support and nurturing me into a person of what I am today. They have always been my strength, my guide and my inspiration. Not forgotten to my family members and close friends who have been supportive and helped me getting through hard moments especially in dealing with the loss of my late father in my first-year study.

Thanks again to those who have been directly or indirectly involved in completing this research work and thesis.

ABSTRACT

The thesis reported on a deterministic inverse scattering method in time-domain to reconstruct dielectric profiles of an unknown embedded object within its peripheral region. Image reconstruction of geometrically simple objects taken after breast profiles and lung(s) model are solely done by simulation executed in single computing. In effort to alleviate the nonlinearity problem of inverse scattering, the inversion technique has been integrated with varied types of techniques to improve the inversion solution. The extended algorithm would only increase the computational cost, nevertheless would never eliminate the nonlinearity problem that degrade the inversion solution. The reconstruction process started in a coarse region which then rescaled down according to object geometry configuration. This is accomplished by combining an inversion technique of Forward-Backward Time-Stepping (FBTS) with an Automated Scaling Region of Interest (AS-ROI) method. Edge preserving techniques comprises of edge preserving regularization and anisotropic diffusion are integrated into the combined FBTS and AS-ROI to further increase the accuracy level in the profiles' intensity. Accuracy of reconstructed object is validated by using mean squared error (MSE), relative error (RE) and Euclidean distance (ED) that measure the precision in terms of pixels' intensity, size and localization. Results exhibited significant improvement in the accuracy level of reconstructed images with a combined method of FBTS and AS-ROI. AS-ROI has successfully increased the pixels precision in relative to FBTS about 10.33% for breast model and 25.17% for lung model. The accuracy increment by AS-ROI is due to better fields penetration as exterior pixels are replaced with background layer of low profiles. In the combined rescaled and regularized method in FBTS, edge preserving smoothing filter and regularization are alternately imposed on the improved reconstructed profiles by AS-

ROI. Therefore, the accuracy is further increased to 18.58% and 40.68%, respectively for breast and lung model. In term of size estimation, average error in object's radius is analogous to accuracy level measured in MSE. It indicates that efficiency of AS-ROI is highly relied upon the accuracy of FBTS estimation in reconstructing image profiles prior to rescaling process. Apart from that, accuracy in size estimation differ for varied shapes due to number of pixels at the boundary. Average RE is 61.94% for a circular shape in breast model, meanwhile attains RE of 4.17% for a U-shape object. The highest RE for a single circular tumour's size in lung model is 62.5%. However, object localization by AS-ROI is 100% for a circular and U-shape object in breast model. Nevertheless, AS-ROI attains an average ED of 2.3 for lung model. Computational time decreases accordingly with the reduced number of pixels involved after the rescaling process. Reduction in the computational time is 13.06% for breast model, nonetheless 28.74% for lung model. Significant time reduction observed for lung model is benefited from considerable number of pixels that has been removed from the original image. The inclusion of edge preserving techniques into the combined AS-ROI with FBTS however has slightly increase the computational time about 5.87% and 4.69% for breast and lung model, respectively. Nevertheless, it compensates the computational cost for higher accuracy of image profiles' intensities.

Keywords: Automated Scaling Region of Interest (AS-ROI), edge preserving techniques, Forward-Backward Time-Stepping (FBTS), image reconstruction, inverse scattering

Penskalaan Automatik Rantau Kepentingan
***dengan Pemuliharaan Sempadan Berulang dalam* Forward-Backward Time-Stepping**

ABSTRAK

Tesis ini melaporkan kaedah serakan songsang yang bersifat tentu dalam domain masa untuk membina profil dielektrik objek yang tidak diketahui dalam rantau sempadan objek tersebut. Pembinaan imej bagi objek dengan geometri mudah yang diambil daripada profil dielektrik payudara dan model paru-paru (paru) dilakukan dengan simulasi yang dilaksanakan dalam pengkomputeran tunggal. Dalam usaha untuk mengurangkan masalah ketidakstabilan bagi serakan songsang, teknik penyongsangan telah disepadukan dengan pelbagai jenis teknik untuk memperbaiki penyelesaian penyongsangan. Pertambahan algoritma hanya akan meningkatkan kos pengiraan, namun tidak akan menghapuskan ketidakstabilan yang akan menjejasan penyelesaian teknik penyongsangan. Proses pembinaan profil bermula di dalam rantau dengan anggaran kasar dan kemudian dikecilkan mengikut konfigurasi geometri objek. Ini dicapai dengan menggabungkan teknik songsangan Forward-Backward Time-Stepping (FBTS) *dengan kaedah Penskalaan Automatik Rantau Kepentingan* (AS-ROI). *Kaedah pemuliharaan sempadan dalam imej terdiri daripada penormalan pemuliharaan sempadan dan penyebaran* anisotropic *diintegrasikan ke dalam gabungan* FBTS dan AS-ROI *untuk meningkatkan tahap ketepatan dalam keamatan profil. Ketepatan objek yang telah dibina disahkan dengan menggunakan ralat min kuasa dua* (MSE), *ralat relatif* (RE) *dan jarak* Euclidean (ED) *yang mengukur kejituan dari segi keamatan piksel, saiz dan petempatan. Keputusan menunjukkan peningkatan ketara dalam tahap ketepatan untuk imej yang telah dibina dengan kaedah gabungan* FBTS *dan* AS-ROI. AS-ROI *telah berjaya meningkatkan ketepatan piksel sebanyak* 10.33% *untuk model payudara dan* 25.17% *bagi model paru berbanding* FBTS.

Peningkatan dalam ketepatan oleh AS-ROI *adalah disebabkan kadar penembusan medan yang lebih baik kerana piksel luaran digantikan dengan lapisan dasar yang mempunyai nilai profil rendah. Di dalam gabungan kaedah penskalaan dan penormalan di dalam* FBTS*, penapis pemuliharaan sempadan dan penormalan diaplikasikan kepada imej yang telah dibina dan ditambah baik oleh* AS-ROI*. Oleh itu, ketepatan meningkat kepada* 18.58% *dan* 40.68%*, masing-masing untuk model payudara dan paru. Dari segi penganggaran saiz, purata ralat bagi radius objek adalah berkadaran dengan tahap ketepatan yang diukur dalam* MSE*. Ini bermaksud kecekapan* AS-ROI *sangat bergantung kepada ketepatan pengiraan* FBTS *dalam membina semula profil imej sebelum proses pengecilan rantau pembinaan profil. Selain itu, ketepatan dalam penganggaran saiz berbeza untuk bentuk yang berlainan disebabkan jumlah piksel pada sempadan bentuk tersebut. Purata* RE *adalah* 61.94% *untuk bentuk bulat dalam model payudara, manakala objek berbentuk* U *mencapai* RE *sebanyak* 4.17%*. Nilai* RE *tertinggi untuk saiz sebiji tumor bulat dalam model paru adalah* 62.5%*. Namun begitu, ketepatan lokasi objek dengan* AS-ROI *adalah* 100% *untuk objek bulat dan bentuk* U *di dalam model payudara. Walau bagaimanapun,* AS-ROI *mencapai purata* ED *sebanyak* 2.3 *untuk model paru. Masa yang diambil untuk pemprosesan berkurangan selaras dengan pengurangan jumlah piksel yang terlibat selepas proses pengecilan rantau pembinaan profil. Pengurangan pemprosesan masa adalah* 13.06% *untuk model payudara, manakala* 28.74% *untuk model paru. Pengurangan masa yang ketara diperhatikan untuk model paru adalah disebabkan banyak piksel yang dibuang daripada imej asal. Penerapan teknik pemeliharaan sempadan ke dalam gabungan* AS-ROI *dan* FBTS *walau bagaimanapun telah meningkatkan sedikit masa pengiraan lebih kurang* 5.87% *dan* 4.69% *masing-masing untuk model payudara dan paru. Walau bagaimanapun,*

gabungan tersebut menyeimbangkan peningkatan kos pengiraan untuk mencapai ketepatan profil yang lebih tinggi.

***Kata kunci*:** *Penskalaan Automatik Rantau Kepentingan* (AS-ROI), *kaedah pemuliharaan sempadan,* Forward-Backward Time-Stepping (FBTS), *pembinaan imej, serakan songsang*

TABLE OF CONTENTS

LIST OF TABLES

LIST OF FIGURES

LIST OF ABBREVIATIONS

2D	Two-Dimensional
3D	Three-Dimensional
ABC	Absorbing Boundary Condition
ADI	Alternative Direction Implicit
AS-ROI	Automatic-Scaling Region of Interest
CFL	Courant Friedrichs Lewy
CPML	Convolutional Perfectly Matched Layer
CSI	Contrast Source Inversion
DART	Discrete Algebraic Reconstruction Technique
DE	Differential Evolution
DEI	Despeckling Evaluation Index
ED	Euclidean Distance
FBTS	Forward Backward Time-Stepping
FCC	Face-Centered-Cubic
FDTD	Finite-Difference Time-Domain
GA	Genetic Algorithm
GPR	Ground Penetrating Radar
HIE	Hybrid Implicit-Explicit
IMSA	Iterative Multi Scaling Approach
MOM	Moments of Method
MRI	Magnetic Resonance Imaging
MSE	Mean Squared Error

NIE	New Integral Equation
ODEs	Ordinary Differential Equations
OGG	Overset Grid Generation
PML	Perfectly Matched Layer
PSO	Particle Swam Optimization
RE	Relative Error
ROI	Region of Interest
SAR	Synthetic Aperture Radar
SOM	Subspace-Based Optimization Method
TCIA	The Cancer Imaging Archive
TE	Transverse Electric
TM	Transverse Magnetic

CHAPTER 1

INTRODUCTION

1.1 Inverse scattering

There are many situations where there is a need to interpret an unknown object with limited known data for deduction. This can be described as inverse problems, which arise in medical field to reconstruct internal structure of human body [1, 2], non-destructive testing to detect cracks or quality of material structure [3], geophysical prospecting [4] that can be applied to find oil mines or other green resources, as well as for archaeology [5]. In these mentioned examples, none of required information can be directly obtained from the object as in forward problem. Nevertheless, it is indirectly measured as the unknown object or scatterer [1] is embedded inside of a substance. Inverse problem can be described as to portray image contrast and geometry of an embedded scatterer by manipulating the electromagnetic fields from which it originates, as illustrated in Figure 1.1.

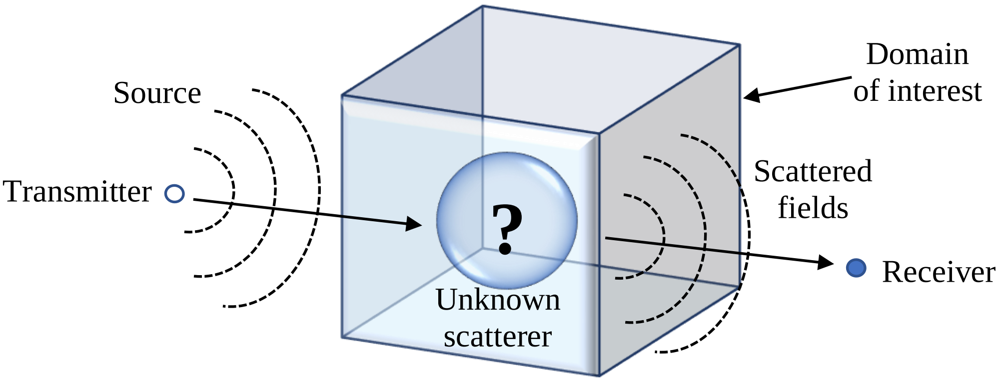

Figure 1.1: Portray physical properties with partially known fields

[1] The unknown object is also defined as scatterer in this thesis

Figure 1.2 summarizes few related matters to inverse scattering. Inverse problem can be classified into two categories; inverse obstacle scattering (impenetrable medium) and inverse medium scattering (penetrable medium) in which geometry and material properties are sought [6, 7]. Unknown scatterer to be solved with inverse scattering is categorized by its dimensional size in relative to incident field wavelength [8]. Extended scatterer is to define object of at least similar size to incident field wavelength. Point-like scatterer is referring to object that is physically smaller than the wavelength.

Inverse scattering method, as the name implies, generally initiated with results which refers to partially known scattered fields originated from the unknown object, to find causes of the result that is the unknown object itself. Obviously, it is rather ill-posed in nature due to the fact that one has to characterize the object's physical properties merely based on fields measurements outside the object and numerical assumption from optimization process. Some information of the physical properties may not be retrieved entirely at the receiving points that encircling the object. The result could be either in good solution or just trapped in local minima due to lack of stability.

Being ill-posed or extremely dependent on the data solution would cause small agitations due to noise during measurement process of the actual object yields overwhelmingly volatile outcome [9]. On top of that, the solution is characterized by nonlinear relation between the scattered fields and dielectric profiles [10]. The term ill-posed is defined by Jacques Salomon Hadamard's rules [9], in which instability of inverse scattering cannot be eliminated even it is combined with other algorithms for better solution [11].

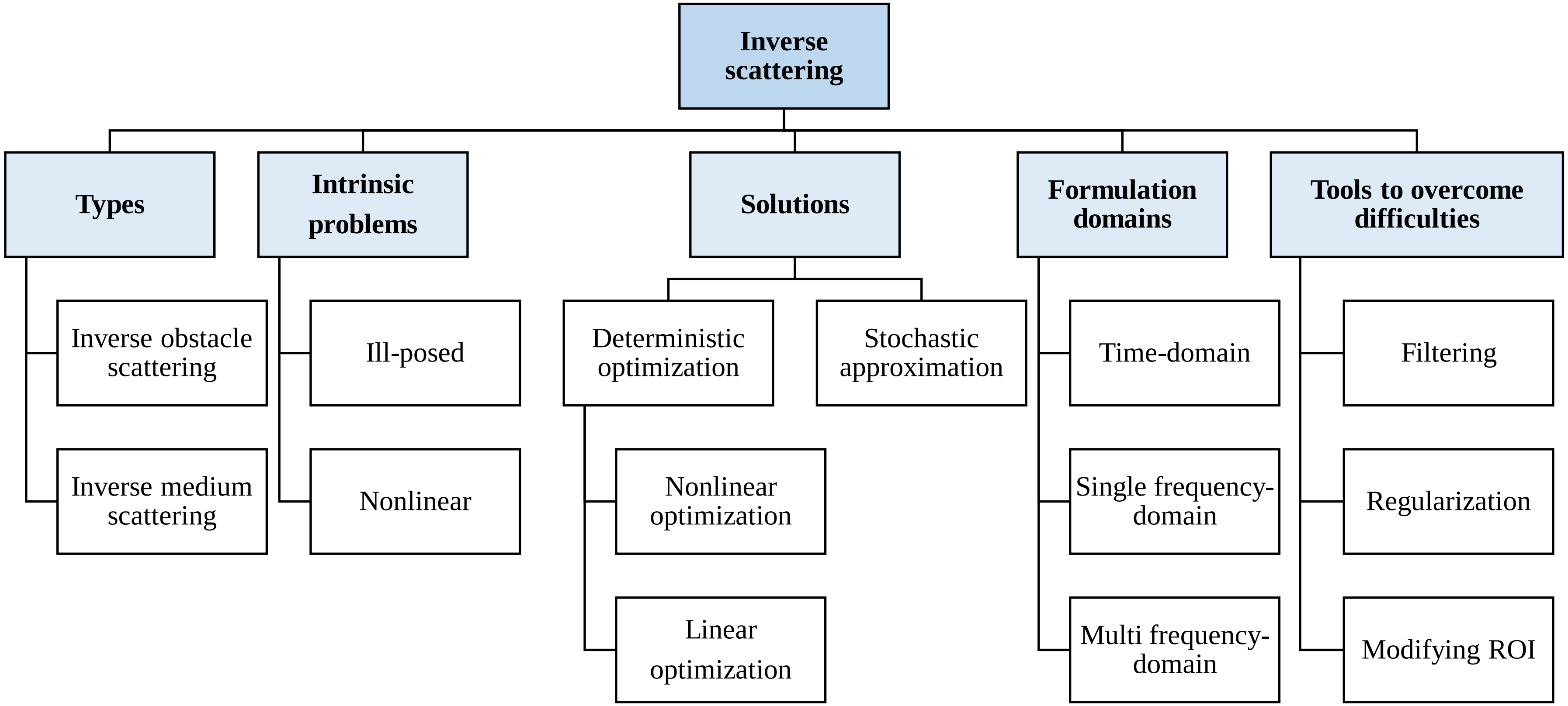

Figure 1.2: Overview of inverse scattering

1.1.1 Deterministic Inversion Solution

Inverse scattering problem can be unravelled either with deterministic or stochastic solutions. Regardless of optimization solutions utilized for the inversion, the effectiveness relies on its ability to minimize the cost functional, complexity level, appropriate number of parameters involved, as well as convergence criterion [12]. Classical methods that have been well-developed over past decades can be categorized as deterministic algorithm divided into nonlinear and linear solutions, which still widely discussed in recent years [12].

Deterministic solution is quite synonym to nonlinear optimization, in which some of the proposed methods are gradient based method [11, 13], Contrast Source Inversion (CSI) [14], Subspace-Based Optimization Method (SOM) [15, 16] and New Integral Equation (NIE) method [17]. The process is initiated by assigning initial guess values as an estimation for the object's profiles, in which some are empirically determined [11, 13], roughly determined [15, 17] and some are calculated [14]. The solution progresses iteratively towards convergence. Conventional deterministic gradient based method compares measured scattered fields outside the sought objects to be determined with computed scattered fields originates from artificial object for optimization [18, 19]. Conjugate gradient method and Polak–Ribière Polyak search directions are employed in most deterministic solutions to determine the object profiles [11, 13, 14, 16, 17]. Most deterministic solutions solve forward problem to obtain scattered fields at each iteration, nevertheless is not required in CSI thus reduce the complexity and computational burden [14].

There are two obvious limitations with deterministic solution. First, there ought to be priori knowledge of the scatterer such as its material type and profiles boundary [16, 20]. Estimation in initial guess must be approximate to the actual object contrast setting [16, 17, 21]. This could be unrealistic under certain circumstances, considering that the sought object is supposed to be unknown. Secondly, most algorithms are implemented in iterative manner which might suffer from high computational burden particularly for higher dimensional problem [16, 17, 20, 21]. However, the end results are often quite promising despite its limitations.

Linear or weak scattering method is based on approximation of the scatterer to linearize the relation between the scattered fields and object profiles. Conservative linear methods are Born or Rytov approximations, that attain the linear relation by assuming very low contrast between layers of object and background with low and high frequency, respectively [8]. These methods only can provide rough estimation on the object.

1.1.2 Stochastic Inversion Solution

State of art to solve inverse scattering problem is by stochastic method or known as population-based optimization to find global minimum in inversion technique. It overcome limitation of deterministic algorithm in which eliminate dependency on the properties of the unknown scatterer [12, 22]. Some proposed stochastic methods to solve inverse scattering problem are Genetic Algorithm (GA) [23, 24], Particle Swam Optimization (PSO) [23, 25] and Differential Evolution (DE) [25].

It can provide dielectric properties[2] contrast distribution even in complex shape other than locate the scatterer based on probability [23]. Global minimum is searched for to reduce probability of being trapped in false solution. The convergence can be achieved faster since solution is searched in several points in each iteration [22]. Stochastic approach has been proven robust to noise and able to overcome nonlinear optimization limitation, which does

[2] Dielectric properties is a synonym of dielectric profiles or image contrast, comprising relative permittivity and conductivity

not require close approximation of initial guess to obtain good reconstruction results [23, 26]. The overall process does not require gradient and direction as in nonlinear optimization.

However, some may have limitations such as optimization untimely converged and poorly performed for local search which found in GA [27]. Study by [24] which previously utilizes gradient based method [28, 29] also proved that GA unable to supersede the gradient based method particularly for inhomogeneous media with large unknowns. DE which found superior than PSO in terms of speed and accuracy in shape reconstruction [25], nevertheless has no tools to extract and apply global information of the search space [30].

1.1.3 Formulation Domain for Solution Implementation

Formulation to solve inverse scattering can be implemented in continuous time-domain or frequency-domain. Several frequency-domain inversion approaches have shown quite satisfying results subjectively or numerically proven [2, 31]. Advantage of single frequency or monochromatic source in inversion technique is that it can reduce difficulties and complexities in reconstructing dispersive model [2]. Finding from [32] in brain stroke monitoring suggests that, large bandwidth provides insignificant contribution in the result, since useful bandwidth for brain image reconstruction is narrow. However, major limitation of solution in frequency-domain is extreme nonlinearity at high frequency to attain better resolution of image profiles [19].

Study by [33] proposed multi-frequency technique to overcome resolution problem of monochromatic source with continual procedure from low to high frequency. Time-domain obviously has a lot to offer than frequency-domain approach since it operates at broad range of frequencies which in turn provides abundant valuable information. This can be seen in [34], which has demonstrated that the time-domain results are much better than multi-frequency technique. However, despite abundant time-dependant data that can be exploited with time-domain approach, computational cost required for its implementation is much higher. It is a major trade-off between amount of data that can be obtained and the computational cost. Nevertheless, computational cost can be greatly reduced with the implementation in parallel computing [35, 36].

1.2 Overview of Research Work

Despite promising advantages offered by stochastic optimization method, this research work shall utilize well-developed time-domain nonlinear optimization technique namely as Forward Backward Time-Stepping (FBTS), which is deterministic and still an active area to discover. FBTS utilizes gradient-based method that is conceptually similar to modified gradient method by [13], in which the optimization requires solving forward and inverse scattering problem in each iteration to minimize error of fields data. The optimization is locally convergence in which requires proper initial guess to guide the solution. Calculations are implemented in Finite-Difference Time-Domain (FDTD) that discretizes partial differential of Maxwell's equations, which to virtually measure the scattering electromagnetic fields due to scatterer.

FBTS algorithm was pioneered by Takenaka et al. since 1997 [28] with focus research in inversion resolved by deterministic solution in time-domain for nondispersive object [18, 37–40], dispersive object [19, 41], and stochastic solution in time-domain [24]. Recent advancement in FBTS algorithm only manipulate the knowledge of total fields and eliminate the needs of detail information on incident fields in the reconstruction region [21, 24, 42].

Essential of this research is exploiting the limitation of nonlinear optimization inversion technique in which boundary of sought object is of priori known, and the fact that limiting the unknowns that described the object can alleviate the ill-posedness problem [11, 26, 43]. In this research context, limiting the unknowns means segmenting object's region within its peripheral for reconstruction.

Iterative Multi Scaling Approach (IMSA) is a segmentation technique that rescale the size of ROI in multiple stages [11, 44–46]. The zooming process is carried out multiple times until the peripheral object is defined. The resolution level is increased accordingly to the iterative rescaling process. It is very intriguing to incorporate tools which not only can reduce the ill-posedness, nevertheless less complicated to be implemented. There is no documented study to the extent of researcher's knowledge that has applied Adaptive K-means clustering method to point out scatterer location and its peripheral at single iteration in deterministic nonlinear optimization inversion technique.

1.3 Research Problem

FBTS system is divided into two parts, where the first part (direct scattering problem) is to generate measured scattering data which based on actual and estimated input object. Rough image will be used as a priori-estimated input to its second part (inverse scattering problem) to generate the reconstructed object which then utilized to compute its corresponding calculated scattering data in subsequent iterations. Inverse scattering problem of FBTS is highly relying on a correct estimation of the local context to reduce the cost functional value.

Local minimum in the cost functional is sought which guided by proper initial guess. This can lead to the creation of artifacts and resulting distorted reconstructed output image on condition that improper initial guess is applied or arbitrary error occurs during estimating electrical properties in the preceding reconstruction process, as discussed in previous section.

Therefore, it can be said that FBTS is intrinsically nonlinear or instable such that any error or changes in the input process shall produce substantial error on the output.

It is proven in a research study by [10] that the applied low pass filter in both measured and calculated scattering data in inverse scattering problem was more robust to noise in image reconstruction [37]. However, any extended algorithm fused inside FBTS must yields secondary effect, in terms of computational time and space memory allocation, as more processes involved. On top of that, nonlinearity or instability of the inversion solution cannot be eliminated despite being combined with tools to improve the inversion solution. The extended algorithm only able alleviate the effect of nonlinearity problem [11]. Being highly nonlinear would increase the possibility of the solution trapped in local minima, in which can be assessed by the accuracy of the reconstructed image profiles [9, 21].

This research work therefore shall focus on implementing an Automated Scaling Region of Interest (AS-ROI) in FBTS, which can zoom in to object's size and location for image reconstruction. The rescaling process of AS-ROI is intended to overcome the nonlinearity problem, as the level of nonlinearity is proportional to the size of problem or the number of pixels to be reconstructed [11, 21]. AS-ROI is also combined with edge preserving techniques to smooth unnecessary artifacts of the object in the spatial domain. Since the reconstruction area is reduced and with smaller number of pixels involved, such method is anticipated to operate in a timely manner other than improving object's accuracy. Further elaboration of the proposed technique will be discussed in Chapter 3. Appropriate image quality metric will be applied to evaluate the efficacy of the combined algorithms in the image reconstruction.

1.4 Research Objectives

The aim of this research is to reconstruct object profiles within its estimated radius based on object size and location. In order to achieve the research aim, objectives for this research work are as follows:

a) To formulate an algorithm for an Automated Scaling Region of Interest (AS-ROI) that can rescale down the image reconstruction area approximately to object's geometry to reduce the nonlinearity problem and computational cost.

b) To evaluate the combined algorithm of the FBTS, AS-ROI and edge preserving techniques in minimizing relative change of mean squared error (MSE) between dielectric properties in actual and reconstructed object.

c) To validate the consistency of the combined algorithm of the FBTS, AS-ROI and edge preserving techniques in improving the accuracy of reconstructed object with respect to the actual in lung(s) model.

1.5 Scope of Research

The research is motivated by limitations of cancer imaging modalities due to the fact that current surgical procedures are generally still incapable to completely remove the tumour due to the insufficient margin detected. About 20% to 70% patients have to undergo for additional surgeries to remove the excess tumour [47]. Precise detection of tumour delineation would minimize the risk of recurrence. Other than sensitivity, specificity and accuracy, another crucial factors to elevate microwave imaging's profile is to have non-ionizing radiation imposed on patients and cost effective [48], which can be offered with inverse scattering method.

Method and findings from this research work therefore can be beneficial for image acquisition in medical field, such that it could assist radiologist or doctor in detecting tumour or cancerous region. The research work is solely done by simulating the scattering problems of electromagnetic waves towards numerical breast and lung(s) tissues models. Breast model is not represented in its actual form in this research work, nevertheless its dielectric profiles are taken to form simple shapes of objects. Tissues of both breast and lung(s) models are assumed to be homogeneous, which contrast to human tissues. Actual tissue layers are inhomogeneous in nature and may infiltrated to each other. Models are nondispersive which are independent of frequency changes. All numerical models involved are immersed in free space as a coupling medium. Geometrical information as well as dielectric profiles levels of unknown object or scatterer are of interest in this research.

Simulations are carried out in single computing platform, and hence objects ought to be small in size considering times taken for measurement and limited memory capacity to accommodate data for simulations. Algorithms involved in the research work were written in C++ language. Visual C++ is a platform used to obtain the numerical values of reconstructed image along with its field parameters. These numerical values which actually the image profiles then converted into spatial images by using MATLAB code. Evaluation on the cost functional along with the accuracy of the generated images are also executed via MATLAB software.

In inverse scattering method, the type of object that need to be detected has to be specified beforehand. Otherwise, the interpretation would be ambiguous with vast options has to be made. On top of that, it helps to estimate the initial guess of dielectric profiles. Either too high or too low of dielectric profiles guess would cause the optimization trapped in local minima.

In general, the research work is a combination of gradient based optimization FBTS, AS-ROI method as well as edge preserving techniques as shown in Figure 1.3, to improve the accuracy of the reconstructed object in terms of image pixels. Image pixels in this case is referring to dielectric properties value of the object. Ideal condition is assumed for all analyses that the measurement process is not fluctuated by noise. The main focus of the research work is to study the proposed work to overcome the nonlinearity problem of inverse scattering in noiseless condition.

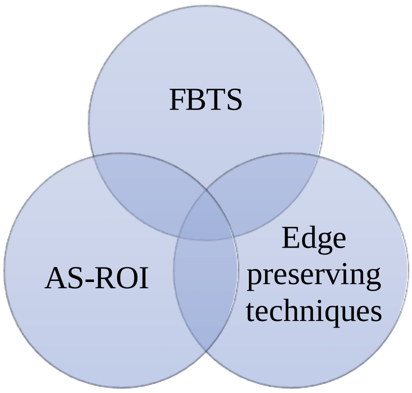

Figure 1.3: Proposed techniques of research work

In AS-ROI, Adaptive K-means clustering is used to zoom in to object's region. Once location and size of object has been estimated, object's area is segmented from the initial image reconstruction region with the rest are regularized to background's dielectric values. Therefore, image reconstruction process only occurs within the segmented area, which is expectant able to improve accuracy as well as to reduce the computational cost. In reality with current technology, the process can be considered as tissues segmental resection for ex-vivo dielectric spectroscopy. In contrast to reality, resection is only performed once tissues area has been recognized as cancerous. Nonetheless in this research, segmental resection or AS-ROI is performed for the sake of dielectric properties measurement to determine the malignancy. Boundary is a clear limitation of nonlinear optimization inversion technique.

AS-ROI in FBTS is fused with edge preserving regularization and anisotropic diffusion filter, which alternately applied on gradients obtained by Polak-Ribière-Polyak [18, 49] and image gradients. It would help to smooth while preserve the edges of reconstructed object. The edge preserving process, however, only employed on relative permittivity image while conductivity is only optimized by AS-ROI in FBTS. Therefore, it reduces the number of parameters involved, since each dielectric property needs its own parameter settings, which is formidable task to be determined. In addition, incorrect parameter estimation would cause errors in the reconstruction solution. Parameters in edge preserving techniques includes regularization coefficient, gradient threshold, potential function and number of iteration to initiate the process. These parameters value are determined empirically once the original ROI rescaled down to object's size. Optimal values are evaluated based on image similarity index by using MSE between the reconstructed and actual object.

1.6 Contribution of the Research

Innovative aspect for the research work is threefold. Firstly, Automatic-Scaling Region of Interest (AS-ROI) is designed to extract object's region automatically during iterative reconstruction based on the estimated location and size. It incorporates Adaptive K-means clustering method as a segmentation tool to point out object's region in single iteration with single resolution level. In contrast to this contribution, IMSA which also has the same function is executed in multi stages in multi-resolution level [11, 44–46]. However, AS-ROI requires sufficient details of reconstructed image for segmentation purpose to be instigated in early iterations of reconstruction. Computational cost can be reduced by AS-ROI since less number of pixels are involved. High accuracy of reconstructed object significantly contributes to the solution speed.

Secondly, edge preserving techniques are integrated with FBTS once the reconstruction area has been segmented. Edge preserving regularization is usually imposed on the solution [13, 18, 29, 50]. Nevertheless, in this contribution regularization is applied on both solution and reconstructed image profiles by means of edge preserving regularization and anisotropic diffusion, respectively. As for the regularization on the solution, it is only applied on relative permittivity despite that it commonly applied on all profiles available [13, 18, 29, 50]. However, the regularized relative permittivity is unaffected by the unregularized conductivity.

Thirdly, the feasibility of the proposed work is studied on lung(s) area which reconstructed based on related literatures. The analyses are extended from breast to lung(s) phantom model due to lung cancer has the highest mortality rate in comparison to other cancers. The highest statistic is not only reported in Malaysia, nonetheless occurred worldwide [51, 52]. Lung(s) phantom model was never been studied to be reconstructed by FBTS. Therefore, several phantom models are empirically tested in terms of sizes and level of contrast between its layers, since the minimal value for the lung(s) size and contrast difference that can cause nonlinearity are not known prior to the analysis. The purpose is to obtain the optimal size and contrast difference of lung(s) phantom model to reduce the nonlinearity problem.

1.7 Thesis Outlines

This thesis comprises of five chapters in total including **Chapter 1**, which covers the background of this research work particularly on the overall view of inverse scattering in terms of its solutions. Research problem, objectives and scope of research are also included.

Chapter 2 discusses FBTS, FDTD along with algorithms or tools that have been applied in other research works to mitigate the ill-posedness and nonlinearity problem of inverse scattering. Adjunct algorithms are divided into three sections, each of which discussing potentials and drawbacks of common methods to be incorporated with inversion technique encompasses filtering, regularization and reconstruction region segmentation.

Chapter 3 addresses the methodological processes and theoretical formulations of algorithms utilized in the research to enhance the quality of object reconstruction and at the same time ameliorate the computational cost. Methods that have been explained involving three techniques: FBTS, Automated Scaling Region of Interest (AS-ROI) and edge preserving techniques. Model properties characterization is also presented.

Chapter 4 emphasizes on the analysis of results obtained by using algorithms discussed in Chapter 3. Results are categorized into two aspects: comprises reconstruction by combined method of FBTS with AS-ROI and reconstruction by regularized FBTS with AS-ROI.

Chapter 5 summarizes and concludes the obtained results. Suggestions for future works based on current research limitations are also discussed.

CHAPTER 2

LITERATURE REVIEW

Advancements to alleviate ill-posedness and nonlinearity problem of inverse scattering for image reconstruction until recent years falls between three categories, comprises of filtering, regularization and segmentation of reconstruction region in which focusing on the object to search. Based on thorough review on literatures, regularization is frequently proposed in most approaches to overcome the above mentioned intrinsic problem of inverse scattering. These three categories of adjunct algorithms to optimization method shall be emphasized in this chapter.

This chapter shall be divided into three parts. The first part in Section 2.1 discusses on Forward-Backward Time-Stepping (FBTS), the applications and advancements that have been made to upgrade the conventional FBTS until recent years. The second part in Section 2.2 deliberates on the Finite-Difference Time-Domain (FDTD). The third part in Section 2.3 up to 2.5 elaborates on adjunct algorithms that can be integrated into the FBTS system to improve the inversion technique. The adjunct algorithms of optimization describe on related studies on edge preserving smoothing filter and regularization for denoising purpose along with reconstruction region segmentation by means of multiscaling process.

2.1 Forward-Backward Time-Stepping

Forward-Backward Time-Stepping (FBTS) is a deterministic inversion technique to solve inverse scattering problem in which the cost function is locally minimized. This technique was introduced by Takenaka et al. in 1997 [28]. The function is to estimate geometrical characteristics of a lossy or lossless unknown object embedded in known medium by exploiting the electromagnetic scattering fields radiated from the object. Lossy is referring to a condition that electromagnetic fields can penetrate and propagate into sought object to be detected with certain amount of its power dissipated during the process. In contrast to lossy, lossless is an ideal situation in which the received electromagnetic fields would be equal to the transmitted fields in its intensity level. Both object and background medium can be either homogeneous or inhomogeneous in its profiles' values. The geometrical traits of an unknown object therefore can be estimated by reconstructing the electrical profiles distribution in relative to the object scattered fields.

In efforts to reconstruct the electrical profiles, it requires priori knowledge in a form of initial guess. Proper values of initial guess can guide the optimization solution from being trapped in local minima or so called as premature convergence [21]. On condition that the solution trapped in undesired local minima, the optimization shall not progress to obtain the optimal result [18]. Hence the resulting reconstructed profiles may not be resembled to the actual object.

The optimization process is carried out by means of minimizing the cost function that requires direct problem solution in each iteration. Cost function is the difference between measured and calculated scattered fields obtained from the solution of direct problem. Measured and calculated scattered fields are radiated from actual and estimated object profiles, respectively. Measured fields in the FBTS research context are virtually measured since the whole algorithm is computationally implemented. Direct problem solution is a process of estimating the accumulated scattered fields at the receiving antennas with given object profiles.

Conjugate gradient method with Polak-Ribière-Polyak search directions [13, 29] are employed in the optimization to determine the object profiles. Convergence criterion for the optimization are varied according to researcher's preferences based on the imaging application and desired image quality, which can reached up to 2000 iterations [37].

Formulations of the optimization solution are solved in time-domain by using Finite-Difference Time-Domain (FDTD) that discretizes partial differential of Maxwell's equations. Type of wave mode that characterize the electromagnetic waves propagation in most FBTS research works is the Transverse Magnetic (TM) mode due to its simplicity to be formulated. Transverse Electric (TE) mode on the other hand has more terms in the cost functional [53]. Consequently, it has more Fréchet derivatives to solve the optimization problem with conjugate gradient method which increase the complexity.

The object profiles can be either homogenous or inhomogeneous in nature. Most models utilized in FBTS are considered non-dispersive and only a few research works analysed on the dispersive models [19, 41]. Dispersive is referring to dependency of electrical profiles values with frequencies. Variety of the background medium, however, is never discussed in any paper related to FBTS in which free space is employed as the background.

2.1.1 Applications of FBTS

Most of the FBTS researches were applied in breast imaging to localize tumour. Analyses on a simple non-dispersive two-dimensional (2D) breast phantom model of high contrast in breast composition was reported in [29]. The 2D non-dispersive realistic breast model which derived from Magnetic Resonance Imaging (MRI) image were presented in [54] which have shown the efficacy of FBTS to detect the embedded tumour precisely. It also able to distinguish composition layers of breast constitutes of skin, fatty tissues and fibroglandular with a convergence criterion of 250 iterations. Three-dimensional (3D) heterogeneous and non-dispersive breast model based MRI image was analysed in [1]. The resultant image exhibited reasonable accuracy in reconstructing a 10mm tumour however, deteriorated for 5mm tumour. It was also found that the reduced contrast in dielectric profiles also contributed to poor reconstructed image.

Extended study of the 2D non-dispersive realistic breast model was analysed with Chebyshev filtered FBTS in [37]. The model has high contrast level between fat and fibroglandular layers nevertheless has low contrast between fibroglandular and fat layers. It showed high accuracy in estimating internal structure of breast profiles with 5mm tumour, and additionally has potential to reconstruct dense breast image. Later study by [35] has shown the ability of FBTS to reconstruct tumour in 4mm size. The Chebyshev filtered FBTS in [55] exhibited its ability to eliminate noise in homogeneous breast model nevertheless losing certain amount of measured data due to the filtering effect. Therefore, the researchers recommended to combine band-pass and low-pass filters to avoid missing information in the future work.

Other than being applied for breast tumour detection, FBTS was also studied to reconstruct a 3D air-filled cavity [56], air-filled wooden cylinder [57] and soil characterization presented in [36] which emphasizing on the acceleration of an FBTS algorithm. A 2D lossless cylinder of inhomogeneous electrical profiles was analysed in [53]. A spatial image of lossless dielectric cylinder image with contaminated transient fields was reconstructed by Chebyshev filtered FBTS in [10]. Recent studies [18, 38–40, 49, 58] concerning on reconstructing objects of simple geometries with the dielectric profiles taken from a homogeneous breast model embedded in homogeneous background. Based on satisfactory outcomes reported in the aforementioned research studies, FBTS has great potential to be analysed against variety of imaging applications.

2.1.2 Modified Version of FBTS with Extended Algorithms

Adjunct algorithms to overcome intrinsic problem of inverse scattering and stabilize the optimization solution of FBTS were presented in several research papers. Regularization is a common approach to assist FBTS in order to achieve better solution. The findings of a combined edge preserving regularization in FBTS can be referred from early research work in [29], which later further developed to be an automated version of edge preserving regularization in [18, 49]. A technique to update the threshold parameter of regularization based on the occurrence of edge was also briefly explained in [18].

Other regularization scheme was analysed in [40] which employed a Tikhonov regularization. However, numerical measures on the accuracy of reconstructed object was not presented. The method was also studied in [18] to compare edge preserving regularization and Tikhonov regularization which found that the latter technique produces oversmoothed effect on the reconstructed electrical profiles. Total variation regularization was studied in [39] showed higher accuracy for the regularized case of relative permittivity. Conductivity on the other hand had higher error compared to the nonregularized case as the optimization process approaching the convergence criterion.

Filter is another common tool that can stabilize the FBTS solution under condition of contaminated scattered fields. Chebyshev lowpass filter was integrated into FBTS that have been discussed in paper [37, 55]. Contaminated model was also analysed with Elliptical filtered FBTS in [38]. The geometrical of buried object was successfully characterized and missing information on the measured data was not reported. Preliminary study of this research work in [58] did not utilize the median filter against noisy condition. However, it was analysed under ideal setting to overcome ill-posedness and nonlinearity of inverse problem. The result exhibited great improvement on both relative permittivity and conductivity images which verified by mean squared error (MSE) measure.

In terms of expediting the inversion process of FBTS, researches in [56] employed a source group method which uses the concept of multiple transmission of electromagnetic fields to reconstruct a three-dimensional air-filled cavity. The research was motivated by expensive computational due to the increase number of transmitter to provide more information of sought object in a form of total scattered fields. The implementation of FBTS with parallel computing was analysed in [57] which found that computational time can be greatly reduced compared to the conventional FBTS. Due to the time reduction with parallel computing, it was utilized in later study to reconstruct a three-dimensional breast model [1]. In [36], researches have introduced a random boundaries concept in which reduces the computational time about 22%.

Iterative Multi Scaling Approach (IMSA) is another technique that was proven able to reduce the computational cost [11, 43]. Nevertheless, it also elevates the accuracy of the reconstructed profiles by FBTS due to the increment in resolution degree which provide more detailed information [11, 43]. The reconstruction process with IMSA is only performed on the selected pixels which are identified to be part of the object at higher resolution degree. Rationally it would reduce the number of pixels to be processed corresponds to the reduction of reconstruction area. Therefore, times taken and memory for storage are reduced accordingly. The rescaling process is carried out multiple times until it reached the desired target area based on the stationary condition.

Current advancement made in FBTS was to eliminate the need of information on incident fields [21, 24, 42]. It only requires total electric fields that tangential to the surface in which the conventional cost functional of FBTS was reformulated. Nonetheless, optimization problem was also solved by using conjugate gradient method and Polak-Ribière-Polyak search directions which similar to the conventional method. Another recent progression made on FBTS algorithm is its integration with an Overset Grid Generation (OGG) that overlap static main and sub-mesh as detailed in [59]. The results exhibited potential to reconstruct object profiles.

In terms of expediting the inversion process of FBTS, researches in [56] employed a source group method which uses the concept of multiple transmission of electromagnetic fields to reconstruct a three-dimensional air-filled cavity. The research was motivated by expensive computational due to the increase number of transmitters to provide more information of sought object in a form of total scattered fields. The implementation of FBTS with parallel computing was analysed in [57] which found that computational time can be greatly reduced compared to the conventional FBTS. Due to the time reduction with parallel computing, it was utilized in later study to reconstruct a three-dimensional breast model [1]. In [36], researches have introduced a random boundaries concept in which reduces the computational time about 22%. Table 2.1 summarizes several studies that have incorporate adjunct tool(s) to improve the FBTS solution.

Table 2.1: Summary of FBTS evolution

Authors	Tool(s)	Contribution(s)
Yong et. al. [18]	Edge preserving regularization	Parameters of edge preserving regularization were updated automatically which correspond to FBTS parameters. The proposed technique was proven superior in terms of accuracy level measured by MSE than Tikhonov regularization in [40].

Table 2.1 continued

Authors	Tool(s)	Contribution(s)
Jamali et. al. [39]	Total variation regularization	The combination of TVR with FBTS was first studied in the paper. The results showed that the regularized case of conductivity by the combined technique was poorly reconstructed than the FBTS.
Nawawi, Sahrani, Ping, Awang Mat & Abang Zaidel [58]	Median filter	The incorporation of spatial filter into FBTS was first studied in the paper. Increment in the accuracy level indicates that the applied filter towards the reconstructed image profiles has assist the optimization in mitigating the nonlinearity problem of inverse scattering.
Moriyama, Oliveri, Salucci & Takenaka [11]	Chebyshev lowpass filter and IMSA	The applied Chebyshev filter was proven robust to noisy fields, however did not contribute in enhancing the accuracy of reconstructed image with noiseless fields. It indicates that the applied analog filter on fields does not assist the optimization process in mitigating the nonlinearity problem, which contrast to finding in [58]. The rescaling of reconstruction area by IMSA on the other hand has successfully elevates the accuracy of the reconstructed profiles, as the number of problems reduced.

Table 2.1 continued

Authors	Tool(s)	Contribution(s)
Qiu, Zhou, Takenaka & Tanaka [56]	Source group method	Source group method is designed to transmit multiple signals from several transmitters for image reconstruction. It was proven considerably faster than the conventional FBTS that only allow single signal transmission at a time from fixed antenna position. Due to variant in transmitter position, it reduces the necessity of increasing the number of transmitters to collect detailed information on object geometry at various angles.
Moriyama, Yamaguchi, Ping, Tanaka & Takenaka [57]	Parallel computing	In parallel computing, fields and its respective adjoint fields are concurrently calculated by slave computers. Groups of fields and adjoint fields are evenly distributed among slave computers with Message Passing Interface. Consequently, computational time is greatly reduced to 16.67% in comparison to FBTS that implemented in singe computer.
Zhou & Zhang [36]	Random boundaries	It is designed to process only selected fields and its corresponding adjoint fields at random boundaries. Reduction in the data has successfully reduce the computational time about 22%. However, accuracy of the reconstructed object was never discussed.

2.2 Finite-Difference Time-Domain

Finite-Difference Time-Domain (FDTD) is utilized as a solver to a direct problem of an FBTS inversion technique that model the electromagnetic scattering process. The technique which substitute Maxwell's curl equations into central finite difference form was presented by Yee in 1966 [60]. Computation is performed by calculating electric (E_x, E_y and E_z) and magnetic (H_x, H_y and H_z) fields of all grid cells in a Cartesian scheme with a leapfrog manner. Fields of future time are computed based on prior fields in which simulated over finite number of time steps that march on in time.

All related studies to FBTS were implemented in FDTD. Figure 2.1 illustrates grid cells of FDTD in Transverse Electric (TE) and Transverse Magnetic (TM) modes [60]. It shows the distribution of electric and magnetic fields along the Cartesian axis. Δx and Δy indicate the size of grid cell in the x and y direction. In Maxwell's equations, time derivative for the electric fields relies on the spatial derivative of magnetic fields and vice versa [61]. These derivatives are converted into finite differences by discretization, in which the discretized fields are shifted by half time and half space.

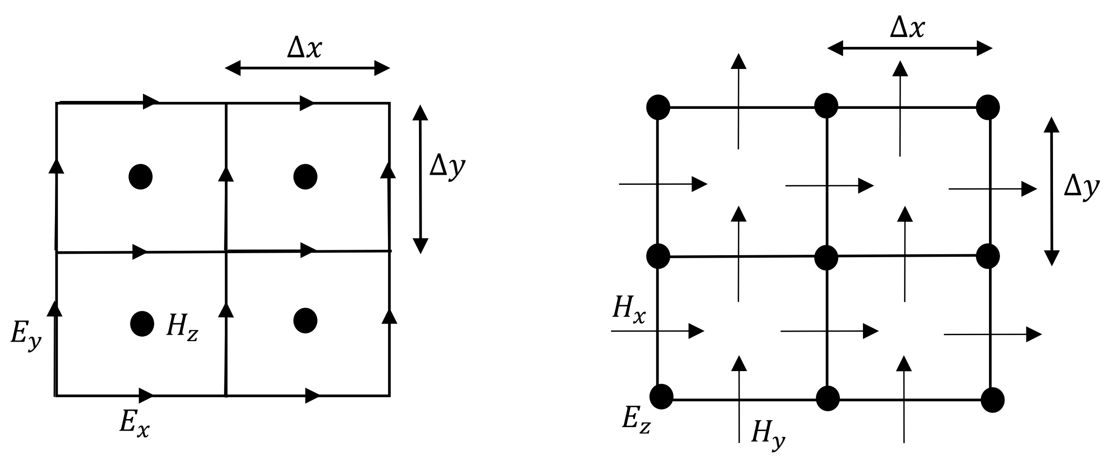

(a) Transverse Electric (TE) Mode (b) Transverse Magnetic (TM) Mode

Figure 2.1: Two-dimensional Yee grid cell of FDTD [60]

The computation of each field is solved with leap-frog method and determined by central difference approximation of two adjacent grid cells in spatial domain. TM mode is selected in most FBTS research works since dielectric profiles distribution in z-direction is of interest to reconstruct the unknown problem.

2.2.1 Cell Size Determination

According to researchers in [62], resolution degree or a maximum size of FDTD cell is commonly ranging from 10 to 15 cells per minimum wavelength. Minimum wavelength is referring to a medium wavelength. This requirement is made to obtain optimal accuracy of fields calculation on FDTD [63]. Other than standard practise in determine the cell size, the selection of cell size is also governed by the geometry features of an object to be reconstructed [62]. Geometry features include the dimension of object and its dielectric profiles [64].

Standard formulation to calculate wavelength in a free space λ_o propagation is given in Equation (2.1), with c and f are velocity of light and frequency, respectively.

$$\lambda_o = \frac{c}{f} \tag{2.1}$$

Frequency remains unchanged as the electromagnetic waves propagate across varied mediums. Speed of electromagnetic waves varies accordingly to the frequency under the case of dispersive medium or object. The wavelength value on the other hand is always changes and characterized by the object profiles regardless whether the medium is dispersive or non-dispersive.

The wavelength value (symbolized as λ_m) of a medium in related to dielectric profiles (ε_r is relative permittivity) at a given frequency of f (assumed to be the highest frequency applied) is expressed as in Equation (2.2) [64].

$$\lambda_m = \frac{c}{f\sqrt{\varepsilon_r}} \tag{2.2}$$

From the equation, the wavelength value of electromagnetic waves that propagates across a medium is inversely proportional to the frequency and relative permittivity. Therefore, the wavelength would be small at high frequency or high relative permittivity. Based on basic requirement of cell size which has been mentioned earlier, the maximum cell dimension in spatial cartesian can be calculated with Equation (2.3) [62].

$$\Delta x = \Delta y = \frac{\lambda_m}{10} \tag{2.3}$$

The cell size is linearly proportional to the wavelength. Small wavelength therefore requires small cell size dimension. In many FBTS studies, spatial cell size of 1mm at 2GHz frequency was utilized for reconstructing non-dispersive breast model in locating tumour [35, 37, 55], dispersive breast model [41] and dispersive simple object [19] and non-dispersive simple objects [18, 38, 58]. Similar resolution was also applied in [49] with 1GHz frequency. Due to approximate size in phantom models utilized in the mentioned studies and similar value of the electromagnetic wave frequency, therefore cell size of 1mm is relevant to be applied in this research work.

Several FBTS research works have utilized bigger cell size due larger dimension of object to search. In [56], the researchers have utilized a cell size of 7.5cm to reconstruct an air-filled cavity from radar data. The same application was seen in [43] in which the optimization solution was solved by using cell size of 0.15m.

2.2.2 Stability Condition for Time Step Size

The selection of time step size plays a major role in stabilizing FDTD simulation result by means of Courant Friedrichs Lewy (CFL) precondition. The size of time step cannot be larger than the prespecified condition to avoid error as the solution marching in time. It directly proportional to the size of grid cells utilized for simulation [65]. Conventional time step of two-dimensional Yee grid cell to reach stability can be computed with Equation (2.4) [66].

$$\Delta t \ll \frac{1}{\frac{1}{\sqrt{\mu\varepsilon}}\sqrt{\frac{1}{(\Delta x)^2}+\frac{1}{(\Delta y)^2}}} \tag{2.4}$$

The term μ denotes magnetic permeability and ε is the electric permittivity. Another version of step size formulation can be referred in [67] which solved by Gerschgorin theorem.

Research study in [68] have proved that spatial filtering imposed on the unstable time-harmonics in the event that time step exceeding the limit can curbed the instability problem. It allows several subgrids to run synchronously to main grid in which limitation on the time step of main grid can be ignored. Similar approach can be seen in recent study of ground penetrating radar (GPR) [69] that also imposed spatial filter on subgridding scheme with time step larger than CFL limit. In [67], the researchers have introduced an adaptive time step based on criterion derived from stability analysis of ordinary differential equations (ODEs).

2.2.3 Absorbing Boundary Condition

Absorbing Boundary Condition (ABC) is functional to absorb the outgoing fields in an infinite space of FDTD [70]. This is to avoid reflection at the vicinity of FDTD space which can disrupts the scattering measuring process within the investigation domain. Perfectly Matched Layer (PML) and Convolutional Perfectly Matched Layer (CPML) are utilized as an ABC in most FBTS research studies. Rigorous analyses and justification to select such ABC layers was never discussed in any FBTS studies.

PML was introduced by Berenger in 1994 [70]. It is a nonphysical lossy medium that has null reflective factor of a plane wave with respect to vacuum layer at varied frequencies and incidence angle. It capable to absorb fields without reflection at the solution boundaries by splitting certain fields components into its constituent parts that decay within the PML medium [71].

2.2.4 Advancements and Applications of FDTD

In [72], Maxwell’s equations discretization of the conventional FDTD method was upgraded by using Face-Centered-Cubic (FCC). It overcome problem of grid error which resulted from plane-waves propagation of dissimilar phase velocity. The same problem motivates researchers in [73] to apply the concept of dispersion reduction to gain optimized operators of finite difference expressions. The obtained result showed improvement in accuracy and computational cost efficiency in which validated by dispersion error.

Models with thin feature in geometry particularly with highly conductive profiles are hardly to solve in FDTD as it necessitates fine grids pertaining to CFL conditions. The consequence is therefore affected the computational size. In [74], the Hybrid Implicit-Explicit (HIE) of high aspect ratios was proposed to be applied in subgridding method which proven well-suited for thin layered models characterization.

Several papers [75–78] mentioned of high computational as a major disadvantage of conventional FDTD. Nevertheless, the issue can be solved with parallel implementation [79]. Alternative Direction Implicit (ADI) was integrated into the conventional FDTD that exhibited noteworthy reduction in the computational cost pertaining to the elimination of the CFL condition in the time step computation [80].

Despite having detrimental grid error which can be significant in a large-scale problem, unfit for thin features model and high in computational, many recent studies other than FBTS research works still simulate inverse scattering problem with the conventional FDTD lattice with considerably good results. Research in paper [81] have utilized FDTD to reconstruct two-dimensional head model which solved by using stochastic inversion of particle swarm optimization. The result showed an increase in speed of computational which was compared to Moments of Method (MOM) solver. Potentiality in using large scale of parallel FDTD with resolution of 1km was discussed in [63] to characterize the ionosphere waveguide of earth executed by petascale and exascale super computers. Evolution of FDTD is summarized in Table 2.2.

Table 2.2: Summary of FDTD evolution

Authors	Tool(s)	Contribution(s)
Salmasi & Potter [72]	Face-Centered-Cubic (FCC)	FCC is proposed to simulate and discretize Maxwell's equations in 3D FDTD. It overcome anisotropic error aroused in cartesian Yee grid, which due to anisotropic phase velocity during discretization. The surface of FCC is equipped with extra vertices enhances the dispersion characteristics of FDTD to allow better object reconstruction.
Zygiridis, Kantartzis & Tsiboukis [73]	Optimized operator	Finite-difference equations are optimized to reduce anisotropic error in Yee grid during discretization process. Similarly to [72], an optimized equations improve the dispersion characteristics of FDTD.
Londersele, Zutter & Ginste [74]	Hybrid Implicit-Explicit (HIE)	It is a subgridding technique in 2D FDTD which purposeful to reconstruct thin layer or miniscule structures. Fields are collocated in subgrids to explicitly determine the boundaries of the reconstructed object. Cell resolution is significantly increased to attain higher precision of reconstruction, particularly for skin effect analysis. Nevertheless, it still complies to CFL stability condition.

Table 2.2 continued

Authors	Tool(s)	Contribution(s)
Kourtzanidis, Rogier & Boeuf [80]	Alternative Direction Implicit (ADI)	ADI is purposeful to discretize the combination of Maxwell’s equations and plasma in the current source. The technique confiscates the CFL stability condition in computing time step size of FDTD. The unavailability of CFL allowing coarser time step, in which reducing the computational time about 70% as coarser time step will accelerate the computations. Based on CFL stability condition in the conventional FDTD, time step size is directly proportional to cell size. Smaller cell size is supposedly required to reconstruct fine details of small object. Therefore, the proposed technique is useful to characterise miniscule structures by reducing the cell resolution without reducing the time step.

2.3 Edge Preserving Smoothing Filter

Filtering process is often suggested to suppress the effect of noise, and some filters were found applied to resist the adverse effect of ill-posed and nonlinear problem in inverse scattering [11, 21, 55, 82]. Noise is intentionally added to the fields of actual object to imitate real situation in which random noise may exists during measurement [55]. Additive white Gaussian noise is usually utilized to contaminate the fields in many inversion techniques [4, 20, 38, 50]. Noise which arises from the process itself is caused by multiple scattering effect for a point-source scatterer which is about the same size of source signal wavelength [83].

Analogue filter particularly network synthesis filter is normally integrated with inversion technique to deal with contaminated measured scattered fields that can leads to severe nonlinearity problem. For instance, varied order of Chebyshev [11, 21, 55] and Elliptical [38] low-pass filter has been integrated with FBTS, which applied to measured fields due to actual object to suppress the effect of noise. Both showed considerably good results in locating sought object in contaminated data merely based on subjective evaluation of the reconstructed object. Nevertheless, there were substantial loss of data during denoising process [55].

On condition that measured fields are contaminated, the reconstructed object deteriorates accordingly [11, 21, 55]. The reconstructed object is also prone to artifacts in noise free environment due to ill-posedness and nonlinearity problem [58]. Artifacts is a term used to describe unwanted features in the reconstructed image resulted from the inversion solution or from the filtering process to aid the solution. Rationally, the application of spatial image filter which directly imposed on the dielectric profiles not only enhance the profiles, nevertheless would affect the fields in its subsequent iterations, though the relation between measured fields and dielectric profiles that constitutes the object is nonlinear [58]. This is due to gradients, directions and step size of FBTS to compute current profiles in conjugate gradient method are rely on the fields obtained from the reconstructed object of its preceding iteration [13, 29]. It is relevant to be applied in an inverse problem that has likelihood to incur error resulted from the inversion solution complicacy, which degrades the reconstructed image. Filtering in denoising artifacts can be applied as a preprocessing before image reconstruction or postprocessing once image is reconstructed.

The application of network synthesis filter and spatial image filter serves the same purpose to achieve the same goal, except that network synthesis filter and spatial image filter applied to fields (signal) and dielectric profiles (image), respectively [11, 21, 38, 55, 58]. Overall process of both approaches is conceptually similar that it simply a direct input and output process. However, comparison of their performance to aid the inversion technique to denoise artifacts in the reconstructed object was never discussed. This section only discusses two types of spatial image filter that has potential to aid inversion technique against its intrinsic problems with edge preserving and smoothing features.

2.3.1 Median Filter Family

Median filter is a common nonlinear filter, in which its output is non-intuitive with respect to its input without explicit relation between input and output [84]. The process of the conventional median filter is fundamentally simple that it computes each pixel by taking the median value of a data sequence constructed of neighbourhood pixels clustered with the respective pixel to be processed. The obtained median will substitute the initial centre point of a window kernel [85]. In other words, current pixel would be substituted by values in its neighbourhood. The filtering process is carried for all pixels regardless whether it is corrupted by noise or vice versa [86].

Median filter is used to eliminate impulse noise in image processing which might arises from error during image acquisition in related to hardware faulty [87]. The filter is also broadly applied to reduce speckle noise [85, 88–90] in Synthetic Aperture Radar (SAR) images. It was also proven in [91] that median filter is consistently good in eliminating speckle noise indicated by Despeckling Evaluation Index (DEI) measure. It has been demonstrated in [92] that median filtered of digital images surpassed the performance of fuzzy filter in eliminating different types of noise such as Gaussian noise, impulse noise, speckle noise and Poison noise.

Research by [93] have imposed a three-dimensional median filter towards its permittivity profile of breast tissue obtained by radar based method. Therefore, in the preliminary result of the research work presented in [58], median filter was iteratively imposed on the reconstructed object in noiseless environment, since the research aimed at mitigating intrinsic problem of inversion technique rather than focusing on impaired reconstructed images due to noise. The results showed significant improvement in terms of similarity degree in the dielectric profiles (relative permittivity and conductivity) measured by MSE between conventional FBTS and iterative median filtered FBTS. Accuracy at the edges however, was only evaluated visually. Hence, similarity degree of the image structure or boundary is not considered in analyses.

Despite its ability in eliminating noise and preserve edges of an image with simple algorithm, main disadvantage of median filter is that it introduces blurring effect in image resolution [86]. This causes some features like thin lines and curve line information missing [94] and even exhibit artifacts like rounded sharp corner [95]. Missing important features is mainly due to the filter process that treats all pixels as contaminated [85, 96]. Apart from that, there is possibility that accurate pixels could be substituted by the contaminated pixels [97]. Other drawbacks are data sorting [98] and windowing masking [86] which necessary to determine the median value, nevertheless are time consuming as the process is carried for each pixel. Several approaches with aim to avoid tendency of missing important features have combined the median filter with other filters. For instance, combined hybrid median with mean filter [98, 99], combined median with Lee filter [85], combined median with Savitzky-Golay filter [88] and combined Gamma with median filter [90]. This shows that median filter alone is insufficient to balance noise elimination and preserve important traits of the input image.

There are several extension methods of median filter to overcome its weaknesses. One example is weighted median filter [100] which relatively similar to median filter process. It takes the median in term of weight values of sequence data in its local neighbourhood. It performs better than median filter according to several researches [85, 95], however, the filtering concept is similar to conventional median such that each pixel incur to be filtered. Hence, weighted median filter also found inherits the same limitation as the conventional median filter [96]. Research in [84] stated that median and weighted median filters only performs well against low intensity of noise, as all pixels are filtered in a fixed size of window kernel. High noise level is suitably solved by large window kernel, however minuscule structures would be erased due to over smoothing. In addition to that, pixels are not selectively filtered which also cause uncorrupted pixels to be oversmoothed as it is treated in the same way as the corrupted pixels.

One approach to reduce missing important features through filtering is to identify corrupted pixels for filtering process that precludes smoothing all pixels available [96] which can be found in other median extension family. Filtering on the corrupted pixels not only preserve edges and other important traits of the image, nonetheless reduce the computational time as well. Contribution from the mentioned research work [96] have proved that the conventional median filtering able to preserve details of the image and adept in eliminating noise, on condition that corrupted pixels are identified correctly. It detects noise by identify pixels with intensity difference of 20 with respect to average value in its neighbourhood pixels, as well as through the existence of large variance in each window kernel. The obtained results were proven better than the existing median family.

Decision based median filter [101] did take into account of specifying corrupted pixels prior filtering, however, uncorrupted pixels also can be replaced since it operates in fixed window size. This is due to some corrupted pixels may not be present in the specified window. Adaptive median filter [102] was developed to tackle the noise detection problem by automated varying window size with some extra conditions for filtering process. It can handle impulse noise up to 50% density, yet consume more time than the decision based median filter [84]. Similar technic can be seen in the method proposed by [103] that improved the decision based method by adaptively increase the size of window kernel in which proven robust to 90% of noise density.

Noise or corrupted pixels in both decision based median filter and adaptive median filter are identified with condition that the pixel falls either at maximum (255) or minimum (0) level of grayscale image intensity. Disadvantage of detecting corrupted pixel merely based on maximum or minimum values is that random noise may incident in between the range which in turn leads to false filtering [96]. Table 2.3 lists advantages and disadvantages of median filter family.

Table 2.3: Comparison of median filter family

Type	Advantageous	Disadvantageous
Median filter	The same window kernel is used throughout the process. The operation is only relying on the data ranking, thus less complex in the algorithm.	Uncorrupted pixels are also filtered and hence susceptible to lose image features which due to invariant kernel size. It is time consuming as all pixels are involved in the filtering process.

Table 2.3 continued

Type	Advantageous	Disadvantageous
Weighted median filter	The operation is steerable by datasets ranking along with pixels’ weight as well. Hence it increases the reliability of the filtered value.	Similar to median filter as window kernel size is invariant for each pixel.
Decision based median filter	Filtering is only imposed on corrupted pixels that have been identified prior filtering.	Severely affected by noise in detecting corrupted pixels which incident at maximum and minimum value.
Adaptive median filter	Window kernel size is varied accordingly to the filtered median value. The median value of datasets in a kernel is also tested with threshold values. It is to determine whether the original pixel should be replaced with the median or being retained. Hence uncorrupted pixels would be unaltered and preserved.	More complicated in algorithm and time consuming to test several conditions for specifying window kernel size and identifying corrupted pixels.

In continual to the preliminary work by using conventional median filter, FBTS has been tested with another median filter family that compare performance of median, weighted median, adaptive median and adaptive weighted median filter. All filters were tested with different size of kernel to find the optimal size for smoothing without eliminating edge details. The final results are shown in Chapter 3, which found that adaptive weighted median yields the highest accuracy among the tested median family filter. Elaboration on the results will be discussed in Chapter 4, Section 4.2.

2.3.2 Anisotropic diffusion

Anisotropic diffusion is the fundamental of regularization technique, which inherently serves as a smoothing and edge preserving filter for image processing. It was introduced by Pietro Perona and Jitendra Malik in 1990 [104]. Most research papers categorized it as a filter instead of regularization method. Standard anisotropic diffusion filter is not formulated to minimize cost functional that is analogous to image reconstruction solution. Nonetheless it is usually directly applied to image for enhancement or restoration purpose in iterative manner. Regularization on the other hand introduces some penalty term towards minimization solution and is frequently imposed to aid solution of inversion technique to ameliorate image reconstruction [105]. In this thesis work, regularization in FBTS is imposed on both solution and image profiles by means of regularization and non-iterated anisotropic diffusion, respectively. Rationale of implementing non-iterated instead of iterated anisotropic diffusion will be explained in Chapter 3. It has been proven in [82] that the filter able to aid inversion solution for tomography seismic model that it has been incorporated into conjugate gradient method as a pre-processing process.

Algorithm of the filter is shown in Equation (2.5), where f is an input image, k is current iteration number, div is divergence operator and τ is a relaxation factor ranging $0 < \tau < 2$ [104].

$$f^{k+1} = f^k + \frac{\tau}{|\eta|} \cdot div[c(\|\nabla f^k\|) \cdot \nabla f^k] \tag{2.5}$$

In research study by [106–108], relaxation factor is defined as $0 < \tau < 1$ which determines the diffusion rate. η is the spatial neighbourhood pixels involved to compute image gradients or derivatives. On condition that gradient is computed in four directions, in example North, East, South and West directions then $|\eta|$ would be equal to 4 [106]. ∇f is gradient image and c denotes edge preserving potential function or diffusion coefficient.

Two types of edge preserving potential functions in anisotropic diffusion are given in Equation (2.6) and Equation (2.7), respectively [109, 110].

$$c(\|\nabla f\|) = \frac{1}{1 + \left(\frac{\|\nabla f\|}{K}\right)^2} \tag{2.6}$$

$$c(\|\nabla f\|) = exp\left(-\left(\frac{\|\nabla f\|}{K}\right)^2\right) \tag{2.7}$$

The first function was taken from Hebert and Leahy function for regularization [50] which suitably used for wide region. The second potential function is beneficial for high contrast layers [108, 109].

In the potential function, the term K is referring to gradient threshold parameter that must be greater than 0 to control the smoothing effect in which manually selected in most conventional method. Provided that the gradient threshold K is too small, then the smoothing effect would be insignificant. However, too large gradient threshold K would resulting oversmoothed filtered images [104, 106, 107]. Typical range of the gradient threshold stated in [108] was defined as $20 < K < 100$. However, in [107], the value gradient threshold K

was stated as 2 based on empirical experimentations. Correlation between gradient threshold and gradient magnitude in related literatures was never discussed. Diffusion or smoothing activity is bounded within detected edges, which is comparable to regularization. Small value in the gradient magnitude $|\nabla f|$ signifies that the area is homogenous and that smoothing effect should be solider for image denoising. Large value on the other hand indicate the presence of edges and therefore smoothing would not be applied within the detected vicinity to preserve the edges details [104].

The performance of standard anisotropic diffusion in many studies has been proven admirable in eliminating noise and preserve edge features. Some of the examples are improving the solution for seismic tomography imaging [82], ultrasound [108, 111] and computed tomography denoising [112]. Among factors that contribute to the effectiveness of the filter is the window size [113]. Too small window would not eliminate the noise and too large window would eradicate subtle features of the filtered image. Focus in research study by [106] was drawn on the convergence criterion to control number of iterations for filtering to avoid oversmoothed result along with improving gradient threshold parameter for diffusion.

Two limitations of anisotropic diffusion highlighted in [113] were smoothing effect is isotropic in all directions and the threshold value for the diffusion function is not automatically adapted to local features of input images. The threshold value has to be manually determined for varied images. Two improvements have been made by the researches to solve the problems, which automatically estimate noise in gradient images at each iteration as well as converting end result of edge preserving potential function in a scalar form into matrix diffusion.

Another drawback which emphasized in [107] was finite difference method usually involves horizontal and vertical directions. This method could be non-robust to noise and hardly distinguish edge and non-edges area due to lack of information on the image features that can be obtained with limited number of directions. Therefore, diagonal neighbours were included to acquire detail information of the image in computing the diffusion coefficient.

2.4 Regularization

Regularization method is functionally used for denoising, which has similar purpose to filtering process. Main difference between regularization and filter is that it incorporates a regularization term which is also known as a penalty term or a prior term into its solution by means of cost function minimization. In other words, regularization needs to be solved with an iterative minimization process. In related to tomographic image reconstruction with inverse scattering, the regularization term is added in the sense to minimize cost functional that stabilize scattered fields with respect to dielectric properties involved. Filters on the other hand have straightforward algorithm process which can be implemented directly towards fields or the reconstructed image. Therefore, it can be assumed that regularization can be considered as a filter in a practical viewpoint. However, filters cannot be categorized as a regularization process for the reason that it does not require any iterative minimization process in its algorithm.

There are many types of regularization methods, such as edge preserving regularization that employed various potential functions, Total Variation, Tikhonov, Singular Value Decomposition, Least Mean Squares, etc. Two types of regularization method are selected to be discussed in this section due to its potential performance based on state of art literatures. Regularization method can be classified into classical (with fixed interval) and local regularization (with varied interval) which based on the interval limit of the integral equation to be solved [114].

Most intrigue subject in related to regularization methods until recent years is the regularization parameters, which many agreed that it is tedious to be determined. Most researches employed heuristic method through empirical experimentation to find the optimal parameter value [49, 50, 115–119]. Advances researches may have upgrade the parameters to be adaptive to either local or nonlocal statistics of the observed image. As for instances, regularization parameter can be determined from systematic construction model [120], adaptive to local noise estimation [91, 121], L-curve criterion [114], and utilized Particle Swarm Optimization (PSO) [122]. Authors in [114] stated three types of regularization parameter selection, which depends on noise level, existence data and a combination of noise and data.

In a broad sense of protecting important features such as edges or curvy area from being removed during denoising with regularization method, correct estimation of discontinuities or boundary is the most important measure to ensure effective edge preservation. Boundary is a common prior knowledge to be explicitly imposed on regularization solution. It was highlighted in [123] that boundary is an important factor in denoising process and an edge density estimator was proposed for fine details preservation.

2.4.1 Edge Preserving Regularization

Edge preserving regularization has been widely applied to overcome ill-posedness problem to inversion technique [13, 18, 49, 50]. The edge preserving regularization method is conceptually similar to anisotropic diffusion filtering which also has constituent elements of edge preserving potential function, gradient threshold as well as regularization coefficient to stabilize the diffusion effect towards the filtered image. Therefore, findings from studies in anisotropic diffusion are relevant to be incorporated into this edge preserving regularization and vice versa.

The cost function in the regularization is composed of a data fidelity term $Q_1(\rho)$ and regularization term $Q_2(\rho)$, which formulated in Equation (2.8) [50].

$$Q_{TOTAL}(\rho) = Q_1(\rho) + Q_2(\rho) \tag{2.8}$$

In the context of this research, the data fidelity term is referring to cost functional of the inversion technique FBTS. Regularization term incorporates the element of controlled smoothing within the vicinity of the detected object. The regularization term in Equation (2.9) can be defined as a summation of potential functions $\varphi(\|.\|)$ in terms of image gradients $\nabla\rho$ which is a priori information that confined in a spatial dimension of $N_x \times N_y$ [13].

$$Q_2(\rho) = \sum_{x=1}^{N_x} \sum_{y=1}^{N_y} \lambda\varphi\left(\frac{\|\nabla\rho\|}{\delta}\right) \tag{2.9}$$

Authors in the original work of [50] explicitly mentioned that the level of image gradient or derivative is depending on types of sought images, in which second order derivative was utilized. However, second order derivative is said to be sensitive to noise which requiring preprocessing process [124]. Image derivative itself can be a research topic in edge detection.

Since the cost functional equation is penalized with a potential function that can be varied, therefore main advantage of an edge preserving regularization is its flexibility to be incorporated with any relevant weighting function that corresponds to the selected potential function [125]. The regularization term can be transformed into half-quadratic regularization to simplify the minimization process written in Equation (2.10) which introduces auxiliary regularization parameter b in Equation (2.11) and its corresponding function $\psi(b)$ into the solution which given in [50].

$$Q_{2_{HQ}}(\rho) = \sum_{x=1}^{N_x} \sum_{y=1}^{N_y} \lambda b \left(\frac{\|\nabla \rho\|}{\delta} \right) + \psi(b) \tag{2.10}$$

$$b = \frac{\varphi'(\nabla \rho / \delta)}{2(\nabla \rho / \delta)} \tag{2.11}$$

The auxiliary parameters of regularization term and optimization solution are alternately minimized. Regularization gradient of reconstructed profile is formed by taking Fréchet derivative of the regularization term, in which the function $\psi(b)$ is dismissed from the gradient equation [18]. Therefore, the function $\psi(b)$ shall not be discussed and not of interest in this research work. Other parameters involved are regularization coefficient and gradient threshold that denoted as λ and δ, respectively.

Regularization coefficient which to balance the effect between the data fidelity (FBTS term) and regularization term can be retrieved by certain methods depending whether the level of noise in known or unknown [121]. Golden Section Search method based on mean and variance of noise computed by windowing process was proposed in [121] to determine the regularization coefficient. It was postulated in the study that the optimal parameter can be estimated on the event that sought image must be approximate to the original. Therefore, Wiener filter was applied as a preprocessing process to the image prior to determine regularization parameter process to obtain better estimation.

L-curve criterion was described in [114] which designed for optimal parameter estimation to regularization. It relies on the cost functional values of both data fidelity (in this case referring to FBTS) along with regularization. These values, however, only depict whether the solution successfully converge or merely trapped in local minima. Based on observations, very low cost functional values do not necessarily mean that object's accuracy is elevated. Neither the graph nor the values would describe the accuracy level of the reconstructed object.

In related to solve inverse scattering problem with deterministic algorithm, recent work namely as automated regularization technique by [18] has demonstrated excellent inversion solution to generate reconstructed images approximate to its actual. The relaxation scheme in alternate minimization was comparable to stopping criterion in [115], nevertheless the method was applied to determine the need to update the auxiliary parameter of regularization term. The same principle is also applied in this research work mainly due to its high performance under noiseless environment setting. Its selection is mainly based on its large potential to be further explored in its explicit parameters.

In efforts to ameliorate edge preservation, researchers in [126] have imposed a convex weighted median as a prior knowledge into the regularization method and exemplified effective in avoiding missing details in the reconstructed image. The method is similar to research [121], in which Wiener filter was used in the preprocessing process prior regularization. In [119], cumulative of first, second and third order derivatives were considered to compute the gradient norm to preserve fine details of sought image.

2.4.2 Total Variation Regularization

Conceptual algorithm of total variation regularization was presented by Rudin, Osher and Fatemi in 1992 [127], which commonly known as TVR. It has garnered attention of researches in various fields until recent years and has been widely applied as a denoising tool in solving inverse problems [115, 128]. It employs the local statistics of the noisy image and iteratively imposed towards minimization solution by means of Lagrange multipliers. Cost functional of TVR in a spatial framework was formulated as in Equation (2.12) [127].

$$\int_{\Omega} \sqrt{\mu_x^2 + \mu_y^2}\, dxdy \tag{2.12}$$

Parameter μ_x and μ_y are pixel values in x and y direction in a region Ω. Detailed explanation on the algorithm and implementation can be referred to the author's original work [127]. It was stated by the authors that the original TVR is computationally faster than edge preserving regularization method.

The application of TVR in assisting the solution of tomographic image reconstruction were described in [129]. Most recent work in [39] showed improvement in noiseless image reconstruction of dielectric profiles by incorporating TVR into FBTS minimization solution, which related to this proposed research. Conventional algorithm of TVR was slightly modified by integrating a rounding parameter [130] into the square root function of spatial image in the Equation (2.12). The parameter was specified to be in infinitesimal value. It is intentionally added to avoid non-zero value of the original term in related to Euler-Lagrange equation. The Euler-Lagrange equation can be regards as a potential function for diffusion. This method is called smooth ε-regularization which mostly found for TVR minimization [129]. However, the method inherits two limitations which the inevitability to solve extra parameter ε as well as ineffectiveness in preserving contrasts and minuscule image structures [129]. In comparison to edge preserving regularization, the smoothing degree of TVR is only determined by the regularization parameter. Boundaries or gradient image is not controlled by any parameter, in which affect the sensitivity level of smoothing on edges and non-edges area. Therefore, it is ineffective in preserving contrasts since edges and non-edges area are not perfectly distinguished.

Among weaknesses of total variation is the ineffectiveness to retain slanted edges [131] though sharp edges are usually well-preserved. It was also stated in [115, 120, 128] that staircase artifacts can be induced from the regularization process itself. In order to solve such issues, researchers in [132] exploited higher order of TVR with linear multiple regularization of ℓ_1 norm of gradient magnitude and Laplacian of the observed image. It showed better restored results than the conventional TVR. The adaptive version of total variation was described in [91] with the results showed proficiency in overcome the weakness of conventional TVR. The term adaptive in the paper is referring to the capability of the algorithm to tune to noise level in the observed image. Nonetheless, these mentioned works only employed local statistics of the image for denoising.

Another way to improve the conventional TVR is to amalgamate local and non-local statistics that yields nonlocal convex function of regularization to achieve higher performance. One of the examples is Non-Local Means of non-local regularization which generalized the concept of Non-Local Means into TVR with the regularization parameters are empirically selected [128]. However, the weightage that denotes the similarity degree between pixels was determined from the original image. It is irrelevant in a practical viewpoint to solve inverse problem as the original information are supposedly unavailable.

Introducing a priori information into regularization of an inverse scattering problem is commonly found method to upsurge the denoised result. Priori information is not directly taken from actual object to search. Nonetheless, it is estimated from the unknown image intensities or profiles. Prior information of the sparsity at vicinity along with the material's discrete values have been utilized in [116] that successfully elevated the reconstructed image.

2.5 Reconstruction Region Segmentation

To the extent of researcher knowledge, none of documented studies involving reconstruction region segmentation in related to deterministic nonlinear optimization inversion technique has applied Adaptive K-means clustering method to extract desired area for reconstruction purpose. Nonetheless boundary of the reconstruction region is required as a priori information of deterministic optimization technique [20], in which segmentation algorithm has potential to point out object's peripheral and location [26, 46].

K-means clustering was utilized to extract patches constitute of pixels with similar features that enhanced better estimation of sparse coding coefficients for the restored images [133]. Similar clustering method was employed in [134] to construct learning sub dictionaries for the purpose of estimating high resolution from low resolution images. Other than being applied for image restoration, contaminated pixels were detected with K-means clustering in research works [135]. Conventional K-means segmentation had been utilized to point out changes in SAR images corrupted by speckle noise [136].

This research is motivated by the notion of object segmentation in Iterative Multi Scaling Approach (IMSA) that reduce the number of pixels in flat region for better solution. Significant amount of the problem unknowns is reduced which providing an increased probability for correct solution [43]. Main difference of this research contribution to IMSA is the number of steps required in zooming process and resolution level in defining the acquired region containing the unknown object.

The Automated Scaling Region of Interest (AS-ROI) in this research work is a non-iterative rescaling process and shall only utilize single scale of resolution for the rescaled investigation domain. The new domain is constructed in a circular shape that confines the vicinity of the detected object which allows the boundary to be updated iteratively during reconstruction. Hence, this would prevent severe distortions in the reconstructed image on condition that applied with fixed and erroneous boundaries. External pixels surround the detected object shall be replaced with the priori known background medium to amalgamate the inversion solution which also mentioned in [31].

2.5.1 Iterative Multi Scaling Approach

The concept of Iterative Multi Scaling Approach (IMSA) is virtually similar to segmentation process that it zooms in to object's region inside the initial coarse investigation domain for reconstruction purpose. Basically, it eliminates exterior pixels that enclosed the detected object by assigning the objective function to zero level [44]. It was originally presented in 2002 for dielectric profiles reconstruction [44] in which autonomous from minimization solution [45]. It imposes constraints or detected boundary towards the solution to achieve better estimation on the located object to search. Zooming procedure is carried out iteratively until the desired region is well defined or has reached the stationary criterion. The resolution level corresponds to the iteration number of zooming process [44–46]. Therefore, the reconstruction process at each newly defined region during the zooming process is carried out with higher resolution level. The authors in their extended work [45] specifically mentioned that the proposed method was independent from the minimization solution. However, the statement can be argued since the reconstructed profile accuracy within the new investigation region has to rely on correct solution of the minimization algorithm, which can be in deterministic or stochastic framework. Each of which has its own limitations to offer correct solution. In the context of cost functional algorithm, the similar equation is used throughout during reconstruction with and without IMSA.

The method is still widely used until recent years. In [137], the IMSA method was integrated with inexact Newton algorithm to solve inversion technique of second order Born approximation. The multi scaling was carried out within the minimization algorithm in Transverse Magnetic mode until specified rescaling criterions are met. The reconstructed profile then filtered and the inversion technique was resumed by taking the filtered reconstructed profiles as its prior in the new investigation domain. In their extended studies [138], the authors implemented the IMSA in conjugate gradient method which also falls under deterministic solution as the previous work [137]. Since the problem unknowns have been reduced, it was proven robust against various level of noise intensity and effective even under limited acquired data [138]. Combination of IMSA with conjugate gradient method also can be referred in [11], which related to this research. Conceptually similar to [137], the multi scaling method was also imposed on the filtered reconstructed profiles in the updated reconstruction region. The combination of IMSA with stochastic minimization by means of PSO can be referred in [139], which showed superior results than the deterministic approach.

Table 2.4 summarizes contributions of several research studies in related to reconstruction region segmentation in inversion technique for fine image reconstruction with IMSA. The table shows comparison in terms of implementation between IMSA against AS-ROI.

Table 2.4: Contributions of ROI segmentation with IMSA

Authors	Minimization technique	Object	No. of Tx[3]	No. of Rx[4]	Segmentation technique	Segmentation parametric configuration	Pre-processing/ Post-processing	Pre-processing/ Post-processing subjects	Quality Metric
Caorsi, Donelli, Franceschini & Massa [44]	Conjugate gradient method	2D homogenous circular cylinder	4	21	Sub-gridding technique	Heuristic	-	-	Relative error
Caorsi, Donelli, Franceschini & Massa [46]	Conjugate gradient based Alternate Direction Implicit method	2D homogenous circular cylinder	Min – 8 Max –36	Min – 8 Max – 49	Threshold clustering	Heuristic based on image histogram	Thresholding filter	Dielectric profiles	Relative error, Euclidean distance
Donelli, Franceschini, Martini & Massa [26]	PSO	2D homogenous square and circular cylinders	Min – 4 Max –36	Min –21 Max – 49	Threshold clustering	Heuristic based on image histogram	Thresholding filter	Dielectric profiles	Relative error, Euclidean distance and dimensional error

[3] Tx is referring to transmitter
[4] Rx is to denote receiver

Table 2.4 continued

Authors	**Minimization technique**	**Object**	**No. of Tx**	**No. of Rx**	**Segmentation technique**	**Segmentation parametric configuration**	**Pre-processing/ Post-processing**	**Pre-processing/ Post-processing subjects**	**Quality Metric**
Salucci et. al. [137]	Inexact Newton	2D homogeneous L shaped cylinders	16	16	Sub-gridding technique	Heuristic	Thresholding filter	Dielectric profiles	Internal pixels of object
Moriyama et. al. [11]	Conjugate gradient method	2D homogeneous L shaped and square cylinders	16	16	Sub-gridding technique	Heuristic	Chebyshev filter	Scattered fields	Internal pixels of object
Proposed method	Conjugate gradient method	2D homogeneous circular cylinder, U-shaped cylinder and lung(s) model	12	12	Adaptive K-Means Clustering	Automated	Regularization and anisotropic diffusion	Fields gradient and dielectric profile	Internal pixels confined by circular region in object's radius

2.6 Concluding Remarks

The first section in this chapter had elaborated on the deterministic inversion technique FBTS which utilized in this research work, which includes its conceptual process, applications and algorithm improvements in recent years. The second section discusses on the FDTD which a solver to the minimization solution of FBTS.

In several research works which have been discussed in later sections, edge preserving techniques including filter and regularization has been proven able to reduce artifacts, preserving important image features and eliminate noise effectively. However, the inclusion of such methods in an inversion technique would increase the computational load.

Segmentation techniques for rescaling purpose by IMSA that generally applied in tomographic reconstruction has been studied. It was found that the incorporation of segmentation in reducing the number of unknowns involved during object reconstruction had augmented the fidelity of the reconstruction technique. The idea of reducing the unknowns has been adapted into this research work.

Conceptual analogy of IMSA is like peeling an onion, which segmenting the object in multiple steps with an increased resolution level until predetermined convergence is reached. IMSA would eliminate any exterior pixels and only updating the interior pixels of detected object. It commonly utilizes hard segmentation method in which each pixel is clustered into single class. Comparisons of IMSA against the proposed technique of this research work are summarized in a form of table. All listed papers in the tables have exhibited positive outcomes towards the reconstructed object. However, fair comparison in its performance cannot be evaluated due to distinct inversion settings in simulations.

CHAPTER 3

METHODOLOGY

3.1 Overview of Process Flow

The flowchart in Figure 3.1 shows the process overview of proposed techniques in this research work. Three techniques involved comprises of Forward-Backward Time-Stepping (FBTS), Automated Scaling Region of Interest (AS-ROI) and edge preserving techniques. The reconstructed profiles are recursively updated with Polak–Ribière Polyak conjugate gradient method in FBTS.

The inversion technique FBTS is improved by embedding AS-ROI and edge preserving techniques into the solution. Conventional process of FBTS is carried out until the reconstructed image profiles has sufficient details in which suitable for object segmentation.

Dielectric profile segmentation by AS-ROI is initiated at iteration S, which occurs only once during iterative reconstruction. The segmentation process shall exclude exterior pixels of detected object. Therefore, only pixels which constitute the detected object shall be considered to be updated for image reconstruction.

Alternate minimization of FBTS is instigated at iteration R, by means of implementing edge preserving regularization on local gradients in even iteration number. In odd iteration number, the solution is minimized by conventional FBTS which then followed with imposing anisotropic diffusion on the reconstructed relative permittivity. The whole process shall be resumed until the predetermined convergence criterion is reached.

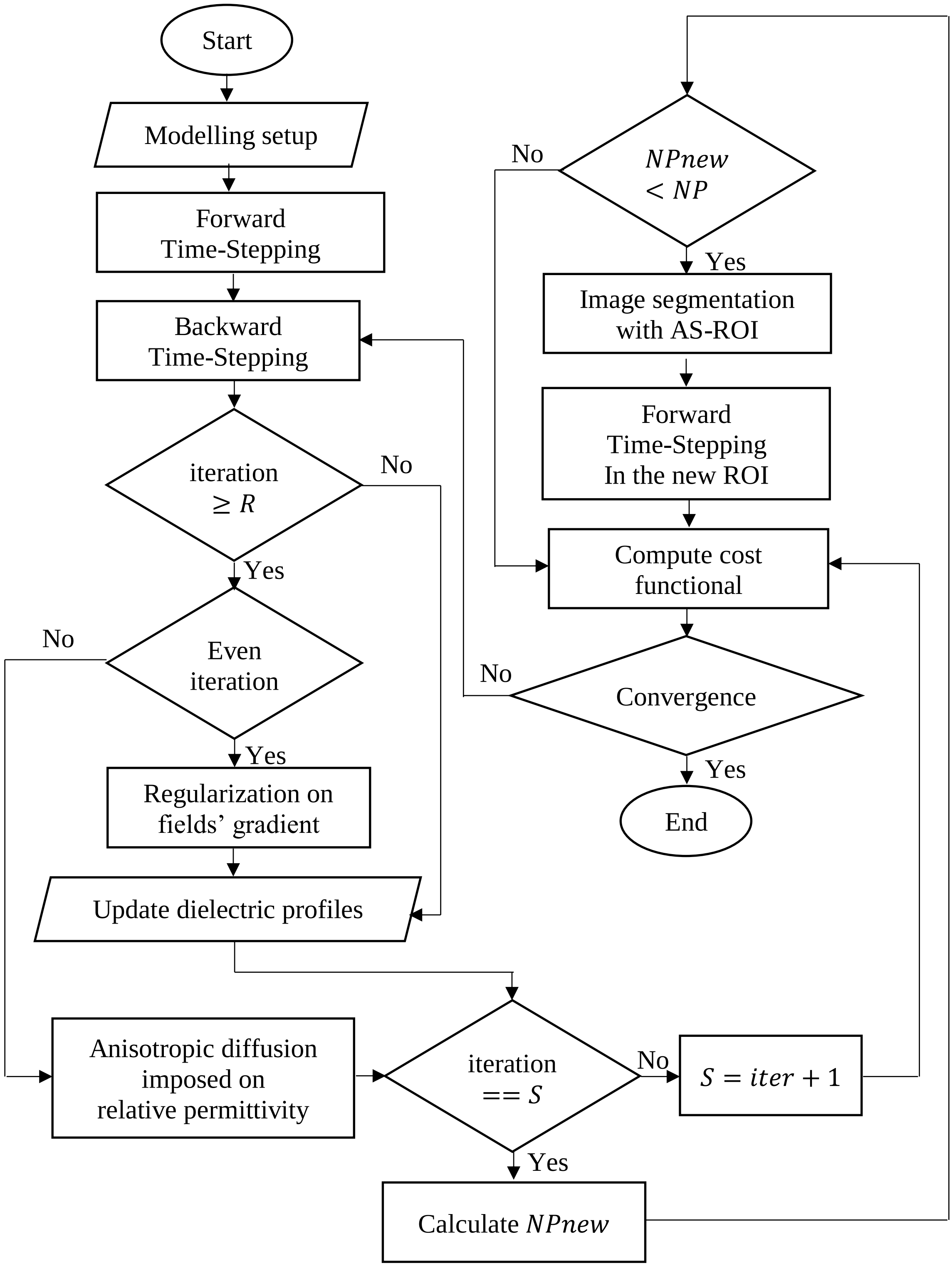

Figure 3.1: Flowchart of proposed techniques

3.2 Forward-Backward Time-Stepping (FBTS)

3.2.1 Overview of FBTS process

The whole process of FBTS can be categorized into two stages: Forward Time-Stepping and Backward Time-Stepping. Image profiles also divided into two types; actual object to be detected and simulated object that imitates the actual. The end result of FBTS is the simulated object that resulted from estimation of optimization solution. The reconstructing region to simulate the dielectric profiles in this research is defined as region of interest (ROI).

Forward Time-Stepping in Figure 3.2(a) solves direct problem in which generates transient scattered fields at the receiving antennas that originated from either actual or simulated object. Scattered fields are obtained with the same intensity of current source, J_{ZM} and antennas position for both actual and simulated cases. Backward Time-Stepping in Figure 3.2(b) on the other hand, employed the difference between total scattered fields $(v_m - \tilde{v}_m)$ collected at the receiving antennas due to actual and simulated object as a source (J'_{ZM}) to irradiate the simulation object.

The resulting fields in the ROI which known as adjoint fields shall then utilized in conjugate gradient method to update gradient and search directions of the estimated dielectric profiles. The obtained direction along with variation of total fields in the ROI will be utilized as a source illuminating simulation object which in turn used to find step size. The value of step size is important to compute estimated image profiles. All measurements and calculations in Forward Time-Stepping and Backward Time-Stepping are solved by means of Finite-Difference Time-domain (FDTD).

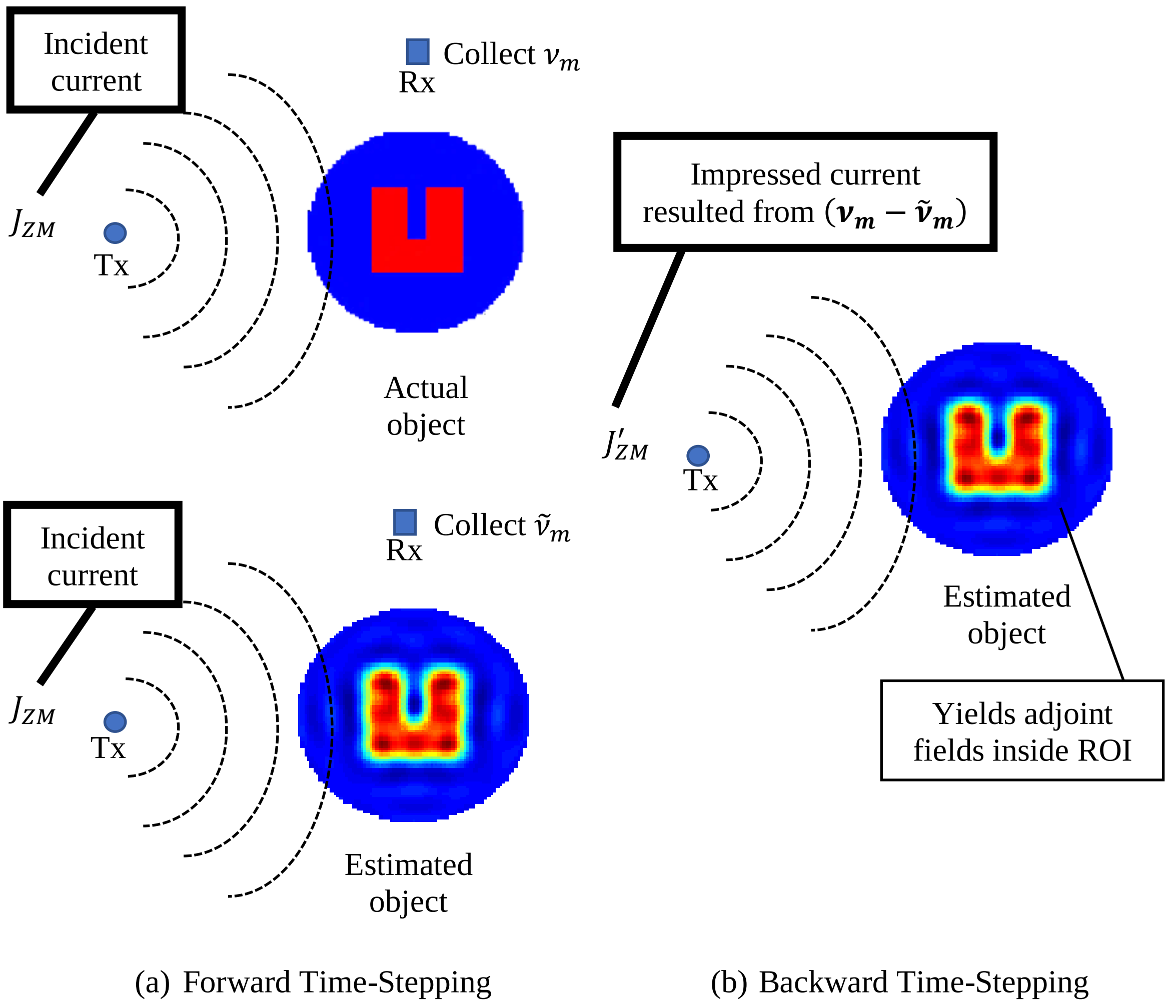

Figure 3.2: Forward and Backward Time-Stepping

Firstly, Forward Time-Stepping is executed to find total scattered fields of actual object. In normal operation of FBTS, the measurement process for the actual object only occurs once in the whole process. Then to initiate the process of FBTS, homogenous rough estimate is assigned to whole ROI which enclosed the sought object. In every iteration of optimization, Forward Time-Stepping is again employed to find collected fields scattered by the simulation object. Then, it followed by Backward Time-Stepping step which resulting the new estimate of dielectric profiles. The estimated profiles will be utilized for subsequent iteration that repeats the same the two stages as its preceding iteration.

3.2.2 Modelling Setup

Figure 3.3 illustrates configuration problem in two-dimensional spatial domain for analysis setup. The lossy object that confined within a predetermined ROI Ω_0 is immersed in a free space background. Significant effects of overcoming ill-posedness and nonlinearity of inverse problem can be obtained with free space as a background [138]. Object in this research is represented by numerical model of dielectric profiles. All layers consisting of object and ROI including the background free space are homogenous in values. M point source antennas which spaced evenly of the same radius at r_m^t $(m = 1,2, \dots, M)$irradiate the object with Gaussian pulses. The term r_m^t is referring to the transmitting antennas with radius of 170mm [1]. Distance between antenna and ROI should be within radiating near field to assume perfect fields propagation. Minimal distance, d_{min} is within 29mm and 33mm on condition that dipole antenna is considered in simulation [1]. However, the distance can be adjusted with varied types of antennas of different specifications.

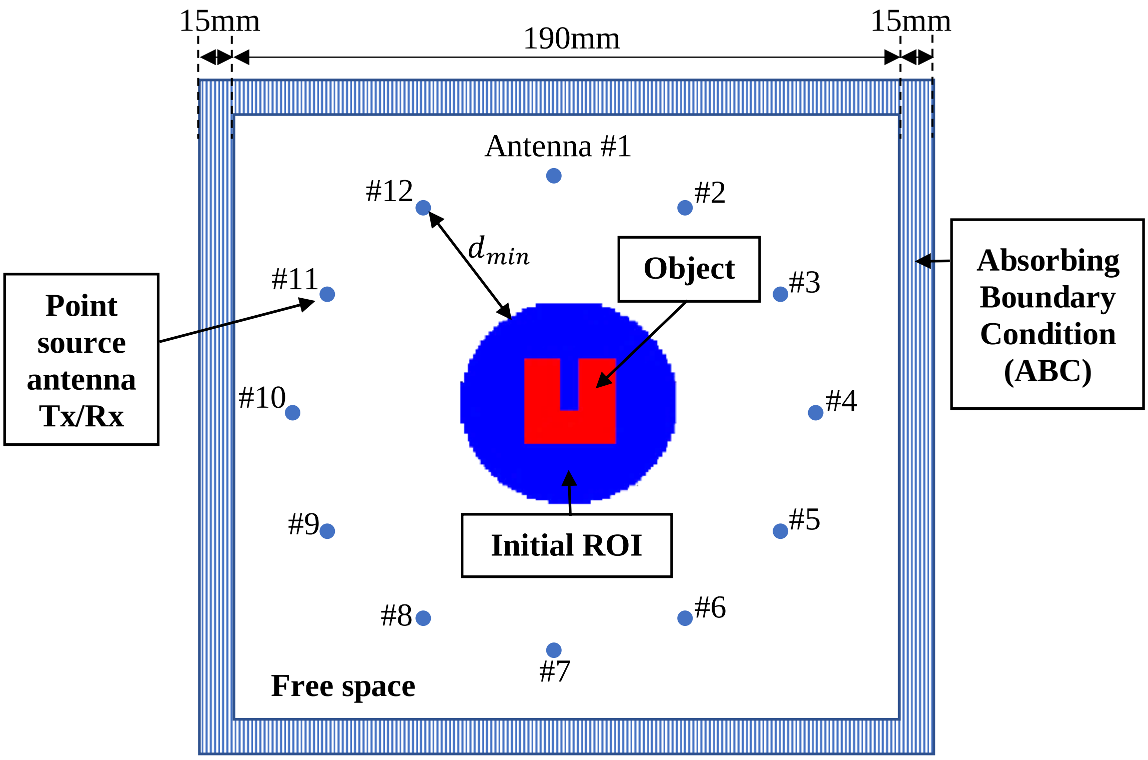

Figure 3.3: Configuration of the problem in 2D view

The pulses are generated by line current source $J_{ZM}(r,t)$ which given in Equation (3.1) pointing in z-direction that orthogonal to object's spatial domain [10, 29].

$$J_{ZM}(r,t) = I(t)\delta(r - r_m^t) \qquad , \qquad r = [x,y] \tag{3.1}$$

Signal source in this research is categorized as soft source since current is impressed to excite electromagnetic fields. Each of the antennas successively act as a transmitter at a time. The remaining N $(N = M - 1)$ antennas located at $r_n^r, n = 1,2,\ldots,N$ act as receivers to collect or measure total scattered fields. Total combination of collected field dataset is $M \times N$.

The term $I(t)$ in Equation (3.2) is referring to current excitation function or so called as modulated Gaussian pulse. t_0 is the time offset between time zero and the centre of Gaussian pulse. T_w is the Gaussian pulse width which to control the width of Gaussian envelope [29].

$$I(t) = e^{-\left[\frac{(t-t_0)}{T_w}\right]^2} sin\big(2\pi f_c(t - t_0)\big) \tag{3.2}$$

The centre frequency $f_c = 2$GHz is utilized in most analyses, in which determined from numerical and subjective observation. $\delta(r)$ denotes Dirac delta function which holds zero value elsewhere except for $r = r_m^t$. r is a space variation of antennas position in two dimensional spatial coordinate of x and y directions.

In Equation (3.3), total electromagnetic fields v_m due to excited current at m^{th} antenna is equivalent to incident field J_m which parallel to Maxwell's equation [10, 29].

$$\mathcal{L}v_m = J_M \tag{3.3}$$

Zero initial condition of electromagnetic fields is assumed for the total fields at time $t = 0$ or before transmitting process, as given in Equation (3.4) [10, 29].

$$\nu_m(r, 0) = 0 \tag{3.4}$$

Equation (3.5) is a matrix representation of electromagnetic fields ν_m and incident field J_m [10, 29].

$$\nu_m = \begin{bmatrix} E_{zm}(r,t) \\ \eta H_{xm}(r,t) \\ \eta H_{ym}(r,t) \end{bmatrix}, \qquad J_m = \begin{bmatrix} J_{zm}(r,t) \\ 0 \\ 0 \end{bmatrix} \tag{3.5}$$

E_{zm} is referring to electric field in z-direction whereas H_{xm} and H_{ym} are magnetic fields in spatial domain. The term η in Equation (3.5) is an intrinsic impedance of free space which can be calculated with Equation (3.6) [10, 29].

$$\eta = \sqrt{\frac{\mu_0}{\varepsilon_0}} \tag{3.6}$$

whereby μ_0 and ε_0 are absolute permeability and permittivity of free space, respectively.

Partial differential operator $\mathcal{L}$ is given in Equation (3.7), with c in its third term denotes speed of light in free space which can be computed using Equation (3.8) [29].

$$\mathcal{L} \equiv A\frac{\partial}{\partial x} - B\frac{\partial}{\partial y} - C\frac{\partial}{\partial ct} - D \tag{3.7}$$

$$c = \frac{1}{\sqrt{\mu_0 \varepsilon_0}} \tag{3.8}$$

Matrix parameter A, B, C and D that related to the differential operator are given in Equation (3.9) [29].

$$A = \begin{bmatrix} 0 & 0 & 1 \\ 0 & 0 & 0 \\ 1 & 0 & 0 \end{bmatrix}, \qquad B = \begin{bmatrix} 0 & 1 & 0 \\ 1 & 0 & 0 \\ 0 & 0 & 0 \end{bmatrix}$$
$$C = \begin{bmatrix} \varepsilon(r) & 0 & 0 \\ 0 & 1 & 0 \\ 0 & 0 & 1 \end{bmatrix}, \qquad D = \begin{bmatrix} \eta\sigma(r) & 0 & 0 \\ 0 & 0 & 0 \\ 0 & 0 & 0 \end{bmatrix} \tag{3.9}$$

In this research, inverse scattering method is employed to reconstruct dielectric profiles consisting relative permittivity, $\varepsilon(r)$ and conductivity, $\sigma(r)$. The cost functional stated in Equation (3.10) is minimized iteratively by means of conjugate gradient method until convergence in order to find the aforementioned dielectric profiles [10, 29, 37].

$$Q_{FBTS}(\rho) = \int_0^T \sum_{m=1}^{M} \sum_{n=1}^{N} K_{mn}(r_n^r, t) |v_m(\rho, r_n^r, t) - \tilde{v}_m(r_n^r, t)|^2 dt \tag{3.10}$$

Collected total fields in Forward Time-Stepping due to actual object is denoted as measured fields $\tilde{v}_m(r_n^r, t)$. Total fields radiated from the estimated object is called calculated scattered fields $v_m(\rho(r); r_n^r, t)$. These two types of received fields are obtained with the same intensity of current excited at r_m^t antenna and collected by r_n^r receiver. The difference between the two fields would indicates whether the optimization is in correct solution or vice versa.

The term $K_{mn}(t)$ in the Equation (3.11) is a nonnegative weighting function that holds zero value at time $t = T$, in which T is the duration taken for measurement [29].

$$K_{mn}(t) = cos\left(\frac{\pi t}{2T}\right) \tag{3.11}$$

The duration time T is specified as $2380\Delta t$ with time step size $\Delta t = 2.31$ps which correspond to the stability condition as described in Section 2.2. Parameter ρ in Equation (3.12) is a medium vector function of dielectric profiles, consisting relative permittivity $\varepsilon_r(r)$ and conductivity $\sigma(r)$ [29].

$$\rho = \left(\varepsilon(r), \sigma(r)\right) \tag{3.12}$$

Updated set of dielectric profiles are given in Equation (3.13) and Equation (3.14) for relative permittivity and conductivity, respectively [29].

$$\varepsilon_r^{(iter+1)}(r) = \varepsilon_r^{iter}(r) + \alpha_{\varepsilon_r}^{iter} d_{\varepsilon_r}^{iter}(r) \tag{3.13}$$

$$\sigma^{(iter+1)}(r) = \sigma^{iter}(r) + \alpha_{\sigma}^{iter} d_{\sigma}^{iter}(r) \tag{3.14}$$

From Equation (3.13) and Equation (3.14), $iter$ refers to current iteration number of optimization and $(iter + 1)$ is the subsequent iteration number. It is a recursive relation that current estimates are utilized to compute the succeeding estimates. In other words, it can also be described that current estimates are calculated based on prior estimates. Elements of those linear relations to compute updated dielectric profiles are step size α and steepest descent direction which denoted as d.

Previous cost functional function in Equation (3.10) is expressed to be similar to the error function defined in Equation (3.15) to find the step size α.

$$Q_{FBTS}(\rho) = Q\left(\rho^{iter}(r) + \alpha^{iter} d^{iter}(r)\right) \tag{3.15}$$

In conjugate gradient method, the determined value of step size α must be able to minimize the cost functional $Q_{FBTS}(\rho)$ with a given descent direction. The explanation to compute the updated dielectric profiles shall begin with finding the steepest descent direction which closely related to cost functional gradients. Then it followed with step size α estimation.

Fréchet differential is performed on the cost functional in order to solve iterative optimization with conjugate gradient method, which resulting gradients of dielectric profiles expressed in Equation (3.16) and Equation (3.17) [37].

$$g_{\varepsilon_r}(r) = 2\int_0^T \left(w_m(\rho; r, t)\frac{\partial v_m(\rho, r, t)}{\partial(ct)}\right) dt \tag{3.16}$$

$$g_{\sigma}(r) = 2\int_0^T w_m(\rho; r, t) v_m(\rho, r, t)\, dt \tag{3.17}$$

The term $w_m(\rho; r, t)$ in the gradient is referring to the resulting adjoint fields due the difference between calculated and measured fields utilized as a current source illuminating the reconstructed dielectric profiles.

Intrinsically, steepest ascend occurs when direction and gradient are in parallel. Hence, the obtained gradients always point to the direction of steepest ascend or maximum increase in the cost function. However, the purpose of optimization is to find local minimum rather than maximum. Therefore, initial steepest descent direction which denoted as $d_{\varepsilon_{r_0}}(r)$ for relative permittivity and $d_{\sigma_0}(r)$ for conductivity in the first iteration of optimization are taking the negative value of the obtained gradients. Formulation for the initial steepest descent direction of each profiles are given in Equation (3.18) and Equation (3.19).

$$d_{\varepsilon_{r_0}}(r) = -g_{\varepsilon_{r_0}}(r) \tag{3.18}$$

$$d_{\sigma_0}(r) = -g_{\sigma_0}(r) \tag{3.19}$$

The updated directions $d_{\varepsilon_r}^{(iter+1)}(r)$ for relative permittivity and $d_{\sigma}^{(iter+1)}(r)$ for conductivity are solved by using parameter β of Polak–Ribière Polyak formula as shown in Equation (3.20) up to Equation (3.23) [13, 29].

$$d_{\varepsilon_r}^{(iter+1)}(r) = -g_{\varepsilon_r}^{(iter+1)}(r) + \beta_{\varepsilon_r}^{iter} d_{\varepsilon_r}^{iter}(r) \tag{3.20}$$

$$d_{\sigma}^{(iter+1)}(r) = -g_{\sigma}^{(iter+1)}(r) + \beta_{\sigma}^{iter} d_{\sigma}^{iter}(r) \tag{3.21}$$

$$\beta_{\varepsilon_r}^{iter} = \frac{\left\langle g_{\varepsilon_r}^{(iter+1)}(r) - g_{\varepsilon_r}^{iter}(r) \middle| g_{\varepsilon_r}^{(iter+1)}(r) \right\rangle}{\left\langle g_{\varepsilon_r}^{iter}(r) \middle| g_{\varepsilon_r}^{iter}(r) \right\rangle} \tag{3.22}$$

$$\beta_{\sigma}^{iter} = \frac{\left\langle g_{\sigma}^{(iter+1)}(r) - g_{\sigma}^{iter}(r) \middle| g_{\sigma}^{(iter+1)}(r) \right\rangle}{\left\langle g_{\sigma}^{iter}(r) \middle| g_{\sigma}^{iter}(r) \right\rangle} \tag{3.23}$$

Analytical approximation approach is utilized to find the step size α value which given in Equation (3.24). Its numerator and denominator equations are listed in Equation (3.25) and Equation (3.26), respectively.

$$\alpha = \left|\frac{b_{ss}}{R_{ss}}\right| \tag{3.24}$$

$$b_{ss} = \int_0^T \sum_{m=1}^{M} \sum_{n=1}^{N} K_{mn} \cdot v_m'(d_\rho) \cdot [\nu_m(\rho) - \tilde{\nu}_m] dt \tag{3.25}$$

$$R_{ss} = \int_0^T \sum_{m=1}^{M} \sum_{n=1}^{N} K_{mn} \cdot \left(v_m'(d_\rho)\right)^2 dt \tag{3.26}$$

The term $(\nu_m(\rho) - \tilde{\nu}_m)$ in its numerator is obtained from Backward Time-Stepping step, and $v_m'(d_\rho)$ is a Fréchet differential of measured field due to the actual object. In FDTD simulation, $v_m'(d_\rho)$ is computed by taking a multiplication product of descent direction with space variation of scattered fields in ROI as a source to illuminate an estimated object. Then the total fields at the receiving antennas is regarded as $v_m'(d_\rho)$.

Conjugate gradient method applied in this research work is summarized as follows:

1: Start, $iter = 0$
2: Assign appropriate initial guess ρ_0
3: Calculate gradient $g^{(0)}$
4: Set initial descent direction $d^{(0)} = -g^{(0)}$
5: repeat
6: Solve for $\alpha^{(iter)}$ that can minimize $Q\left(\rho^{iter} + \alpha^{iter} d^{iter}\right)$
7: Update $\rho^{(iter+1)} = \rho^{(iter)} + \alpha^{iter} d^{iter}$
8: Find $g^{(iter+1)}$ in related to $\rho^{(iter+1)}$
9: Compute $\beta^{(iter)} = \dfrac{\left\langle g^{(iter+1)} - g^{(iter)} \middle| g^{(iter+1)} \right\rangle}{\left\langle g^{(iter)} \middle| g^{(iter)} \right\rangle}$
10: Update $d_\sigma^{(iter+1)}(r) = -g_\sigma^{(iter+1)}(r) + \beta_\sigma^{iter} d_\sigma^{iter}(r)$
11: Find $Q_{FBTS}(\rho)$
12: $iter = iter + 1$
13: until convergence

3.3 Image segmentation by Automated-Scaling Region of Interest

Conventional operation of FBTS is carried out until iteration S, with S is the number of iteration to initiate the Automated-Scaling Region of Interest (AS-ROI) which determined empirically. In condition that segmentation process to define the new ROI started too early, the reconstructed output could not give sufficient information of the sought object. This would cause the radius and offset values of the object location cannot be determined precisely. On the other hand, supposing the segmentation started behindhand, the process could not limit the computational cost. Reconstructed image at later iterations number also contains spurious edges which affect localization of the object.

Segmentation method in AS-ROI is interpreted from MATLAB coding written by [140], in which adaptive K-means clustering is applied. Advantages of adaptive K-means clustering is that the number of centroids and the number of clusters can be determined automatically. Therefore, it eliminates the needs of histogram analysis to observe the threshold level of distinct layers for segmentation purpose. Thresholding segmentation is utilized in most studies for segmentation in IMSA, which requires histogram analysis [11, 43–45]. In this research, AS-ROI is only applied to relative permittivity as its accuracy is much higher than conductivity profiles [54]. Segmentation relies on the ability of the algorithm to find distance between centroids and pixels data. Euclidean distance (ED) is utilized to find the distance in which considered sufficient for segmentation [141]. The whole algorithm of AS-ROI can be categorized into four steps.

Step 1: Finding centroids

Dataset of relative permittivity (ε_r) profiles of an unknown object in the initial ROI are sorted from maximum to minimum values to form one dimensional array of data

$(\varepsilon_{r_1}, \varepsilon_{r_2}, \dots, \varepsilon_{r_{NP}})$. The term NP is referring to the number of pixels of the original reconstruction region. The process started with the selection of centroids μ_i which is the mean value of all observation points for clusters set CL_i. Centroids that is the mean value of each clusters can be calculated with Equation (3.27).

$$\mu_i = \frac{1}{CL_i} \sum_{\varepsilon_{r_i} \in CL_i} \varepsilon_{r_i} \quad \forall i = 1,2,\dots,K \tag{3.27}$$

Total number of centroids is denoted as K, in which i is an integer number that increases from 1 to K. In this research work, maximum number of centroids K is defined to be 10 which is similar to the original work by [140]. Based on observations, the chosen value is optimal for the segmentation purpose of reconstructed image profile. These centroids will generate clusters set of $CL_i = CL_1, CL_2, \dots, CL_k$. Note that the maximum number of clusters is equivalent to the maximum number of centroids K. The first centroid μ_1 is obtained from the mean value of all pixels in the initial ROI. At this stage, the number of elements in CL_i is still equivalent to NP.

Then, relative distance $distA_{ij}$ between centroid and pixels data is calculated with Equation (3.28).

$$distA_{ij}\left(\varepsilon_{r_j}, \mu_i\right) = \left|\varepsilon_{r_j} - \mu_i\right| \quad \forall 1 < i < K, \varepsilon_{r_j} \in CL_i \tag{3.28}$$

Qualified pixels $\varepsilon_{r_{qualified}}$ with relative distance that is less than or equal to the calculated bandwidth bw_i for the cluster centroid as in Equation (3.29) will be utilized to compute the new centroid.

$$bw_i = \sqrt{\frac{1}{CL_i}\sum_{i=1}^{K}\sum_{\varepsilon_{r_j}\in CL_i}\left(\varepsilon_{r_j} - \mu_i\right)^2} \tag{3.29}$$

On a condition that previous centroid equivalent to the new centroid, or once the process has iterated for K times, then qualified pixels which has been assigned to cluster centroids will be discarded from the dataset. The whole process will be repeated until either all pixels has been discarded or the maximum number of clusters is reached.

Stored centroids are sorted in values accordingly. Then the centroid distance μ_{dist_i} in Equation (3.30) between adjacent centroid is calculated.

$$\mu_{dist_i} = \begin{cases} \mu_{(i+1)} - \mu_i & \forall i = 1,2,\dots,K-1 \\ \mu_i & i = K \end{cases} \tag{3.30}$$

The maximum pixel value which obtained from sorted dataset in earlier process is used to determine the minimum distance d_{thres} between centroids as a threshold. The threshold value can be obtained with Equation (3.31).

$$d_{thres} = \frac{max(\varepsilon_{r_i})}{K} \tag{3.31}$$

Any centroids with adjacent centroid distance that is lower than the specified threshold will be discarded to form clusters. Centroids determination process is summarized as follows:

Start, sort $(\varepsilon_{r_1}, \varepsilon_{r_2}, \ldots, \varepsilon_{r_{NP}})$
repeat
    Solve Eq. μ_i
    repeat
        Solve Eq. $distA_{ij}$
        Solve Eq. bw_i
        if $distA_{ij} < bw_i$
            Recalculate new centroid with $\varepsilon_{r_{qualified}}$
        end if
        if (centroid $==$ new centroid || iteration > 10)
            Remove $\varepsilon_{r_{qualified}}$
            Store centroid
        end if
        Update new centroid = centroid
until convergence
Sort stored centroids
Solve Eq. μ_{dist_i}
Solve Eq. d_{thres}
if $\mu_{dist_i} < d_{thres}\ \forall i = 1,2,\ldots,K$
    Remove μ_i
end if

Step 2: Assign pixels to cluster centroids

Distance $distB_{ij}$ between each pixel ε_{r_j} and each centroid are calculated with Equation (3.32).

$$distB_{ij}\left(\varepsilon_{r_j}, \mu_i\right) = \left|\varepsilon_{r_j} - \mu_i\right|^2 \quad \forall 1 < i < K, \varepsilon_{r_j} \in CL_i \tag{3.32}$$

For instance, if five centroids are detected in Step 1, then five distances should be calculated for each pixel. Pixel will be assigned to a cluster which yields the minimum distance. The process is exemplified in the following pseudocode:

repeat
    Solve Eq. $distB_{ij}$
Find minimum distance between each pixel ε_{r_j} and centroids μ_i
if $distB_{ij} ==$ minimum distance
    Assign $\varepsilon_{r_j}$to that CL_i
end if

Step 3: Extract detected object

Object is extracted from the outermost layer detected. In other words, the first cluster detected is discarded with the rest assumed to be object. In this research, object layers are arranged according to its dielectric profiles value. The outermost has the lowest and the innermost has the highest dielectric profiles. This would ease the scattering process for object recognition. On top of that, it also simplifies the process of cluster numbering which corresponds to the intensity value. With the outermost layer supposedly assigned with the lowest cluster number, therefore it can be easily recognized to be discarded.

From Figure 3.4, the outermost layer which is layer 0 is removed. Layer 1 and layer 2 are assumed to be object. Another method to identify the outermost layer is by examining each cluster's pixel coordinates. Shall one of the pixel coordinate from any cluster situated in minimum or maximum value in x or y direction, then the cluster can be categorized as the outermost layer. Coordinates of observation points or pixels which declared as object are stored. These coordinates are then sorted in values accordingly. It yields maximum and minimum values in x and y axis, namely as X_{max}, X_{min}, Y_{max} and Y_{min}.

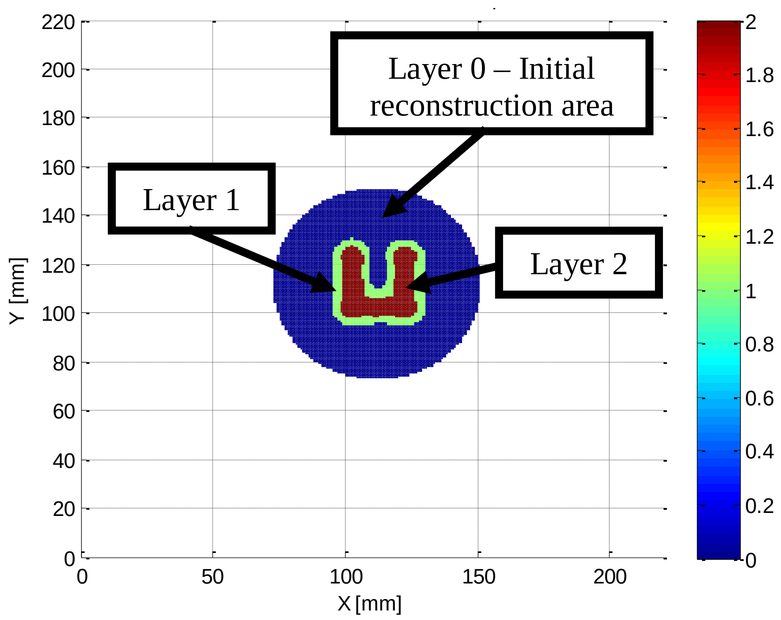

Figure 3.4: Segmented relative permittivity at 30th iteration with its cluster label number

Regardless of object's geometry, intersection between points X_{max}, X_{min}, Y_{max} and Y_{min} form a rectangular that confines the detected object as shown in Figure 3.5. Figure 3.5 shows the object's centre point (x_1, y_1) as well as its distance with respect to FDTD's centre point (x_0, y_0).

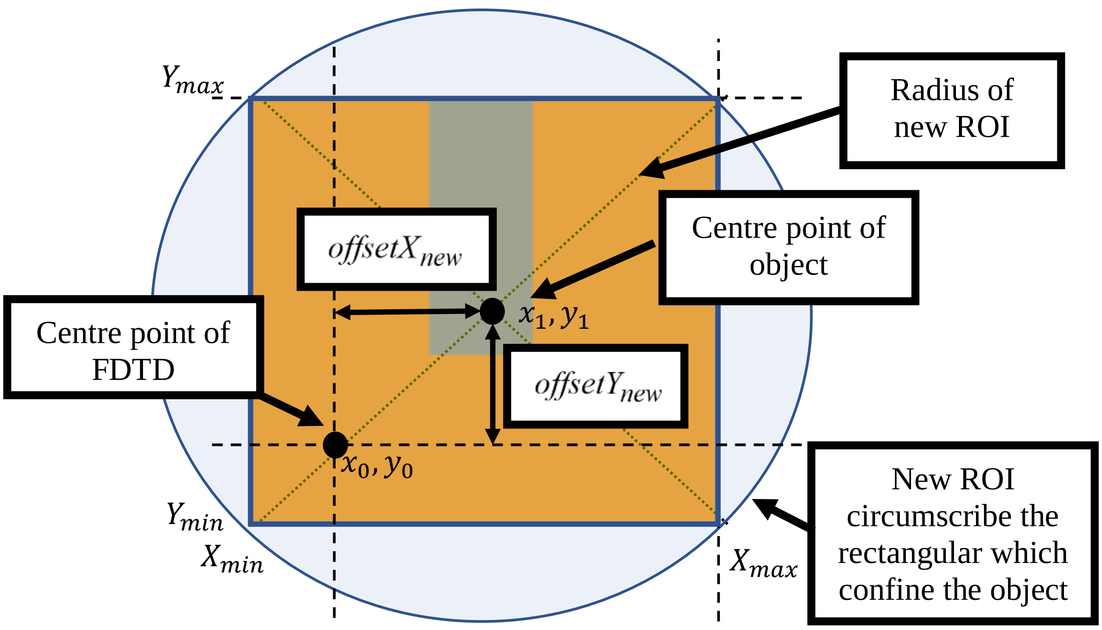

Figure 3.5: Segmented object confined within the new ROI

Centre coordinate (x_1, y_1) of the object can be estimated from the maximum and minimum values in x and y axis as in Equation (3.33) and Equation (3.34).

$$x_1 = round\left(\frac{X_{max} - X_{min}}{2}\right) \tag{3.33}$$

$$y_1 = round\left(\frac{Y_{max} - Y_{min}}{2}\right) \tag{3.34}$$

Distance in x and y directions are referred as $offsetX_{new}$ and $offsetY_{new}$, which can be obtained with Equation (3.35) and Equation (3.36), respectively.

$$offsetX_{new} = x_1 - x_0 \tag{3.35}$$

$$offsetY_{new} = y_1 - y_0 \tag{3.36}$$

These distance values are significant to compute centre point of the newly ROI region. In order to avoid losing desired pixels, note that peripheral of detected object which initially delimited by a rectangular is circumscribed in a new circular region. Radius of the circular or the new ROI region is determined by the maximum distance in four directions as shown in Figure 3.6.

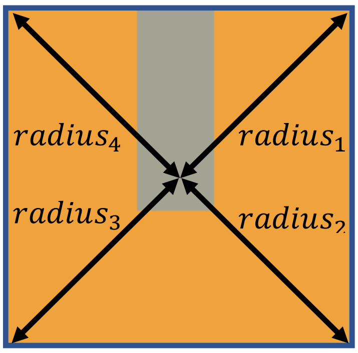

Figure 3.6: Distance in four directions to find radius of the new ROI

Logically each radius must be of the same distance, since it is computed from the centre point of the rectangular. However, in programming there would be slight error between these values. Therefore, maximum distance would be considered as the radius of the new ROI, which purposely to avoid missing pixels as mentioned earlier. Each radius can be calculated by Equation (3.37) to Equation (3.40).

$$radius_1 = round\left(\sqrt{(X_{max} - x_1)^2 + (Y_{min} - y_1)^2}\right) \tag{3.37}$$

$$radius_2 = round\left(\sqrt{(X_{max} - x_1)^2 + (Y_{max} - y_1)^2}\right) \tag{3.38}$$

$$radius_3 = round\left(\sqrt{(X_{min} - x_1)^2 + (Y_{max} - y_1)^2}\right) \tag{3.39}$$

$$radius_4 = round\left(\sqrt{(X_{min} - x_1)^2 + (Y_{min} - y_1)^2}\right) \tag{3.40}$$

The following pseudocode summarized all processes involved in Step 3.

1: Discard the first cluster
2: Store pixels in other clusters which assumed to be object
3: Sort the desired pixel coordinates
4: Solve for object's centre point (x_1, y_1)
5: Solve for object's distance $offsetX_{new}$ and $offsetY_{new}$
6: Solve for ROI's radius

Step 4: Rescale ROI

Suppose the number of iteration of FBTS $iter$ has reached a predefined iteration S to initiate segmentation process, number of object's pixels NP_{new} are calculated from the radius determined in Step 3. In condition that the current number of pixels of segmented object is larger or equal to its initial pixel number, then AS-ROI shall be repeated in the next iteration number of optimization $(iter + 1)$. Else if the desired pixels are less than the actual, then the reconstruction region shall be rescaled down. At this stage, FBTS runs as its first iteration yet with smaller reconstruction region. In order to obtain better result, the number of iteration S can be empirically determined rather than being randomly chosen.

Direct scattering with Forward Time-Stepping is implemented to compute new measured scattering fields $\tilde{v}_{m_{new}}$ of the object in the new ROI. All variables related to the initial number of pixels are redeclared accordingly. Initial guess is also redefined to be in the new ROI with its pixel values taken from previous iteration number. Then, inverse scattering by Backward Time-Stepping is repeated in the new region until convergence.

Figure 3.7 shows rescaling process from the initial ROI to new ROI, which highlighted in the red bold dotted lines. Note that the new reconstruction region analogous to object's location and size.

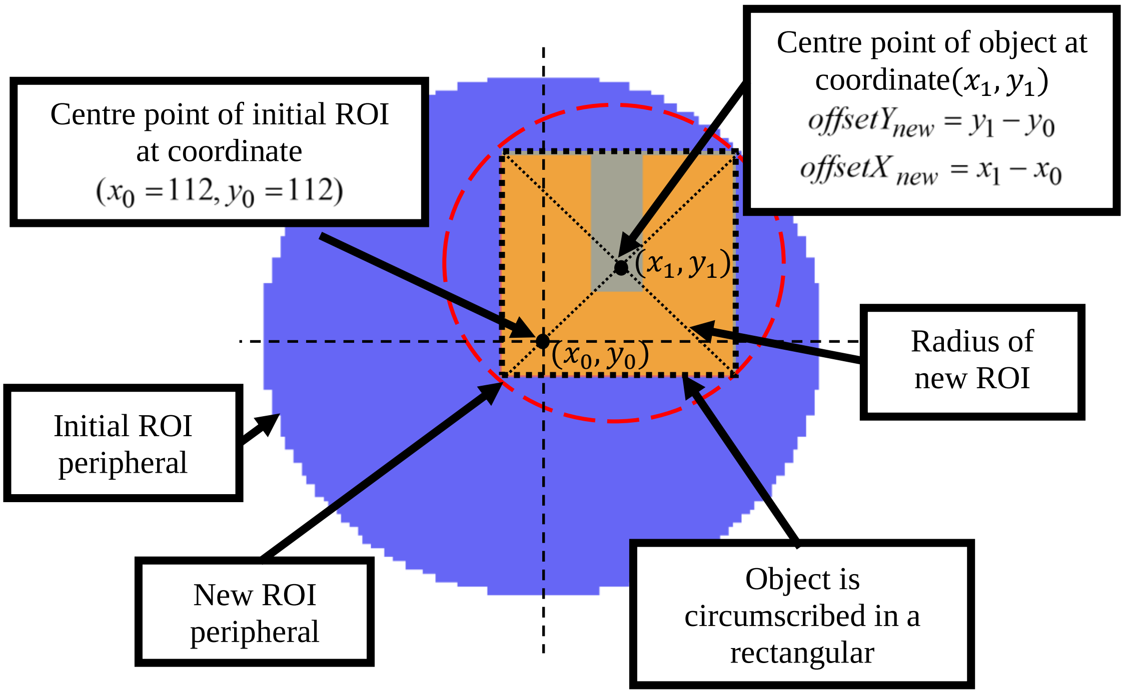

Figure 3.7: Redefine the new ROI

Rescaling process in Step 4 is summarized as follows:

if $iter == S$
    Solve for NP_{new}
    if $NP_{new} \geq NP$
        Resume FBTS in initial ROI
        $S = iter + 1$
    end if
    else if $NP_{new} < NP$
        Redefine reconstruction region coordinates
        Solve for $\tilde{\nu}_{m_{new}}$
        Redeclare all variables related to NP
        Redefine initial guess in the new ROI
    end else if
end if

3.4 Regularized FBTS with AS-ROI

Previous cost functional of FBTS is slightly modified by adding a regularization term which only imposed on the rescaled relative permittivity obtained from fused AS-ROI with FBTS. This condition is dissimilar to several related research papers that employed regularization on all dielectric profiles involved [13, 18]. As a result, it yields $Q_{TOTAL}(\varepsilon_r, \sigma)$ as in Equation (3.41) which a summation of cost functional for the rescaled FBTS $Q'_{FBTS}(\varepsilon_r, \sigma)$ and edge preserving regularization $Q_{EPR}(\varepsilon_r)$ [18, 29].

$$Q_{TOTAL}(\varepsilon_r, \sigma) = Q'_{FBTS}(\varepsilon_r, \sigma) + Q_{EPR}(\varepsilon_r) \tag{3.41}$$

Regularization term $Q_{EPR}(\varepsilon_r)$ which written in Equation (3.42) is bounded in the new reconstruction region Ω.

$$Q_{EPR}(\varepsilon_r) = \lambda \iint_{\Omega} \varphi\left(\frac{\|\nabla\varepsilon_r\|}{\delta}\right) d\Omega, \;\; \Omega = NP_{new} \tag{3.42}$$

The regularization coefficient or weighting parameter λ in the regularization cost function $Q_{EPR}(\varepsilon_r)$ will balance the effect between FBTS and regularization data. The potential function or regularization function φ is liable for image diffusion in homogenous area which delimited within detected edges. Edges in this case are made prevalent by using the gradient threshold parameter δ, which used to identify boundaries between regions based on the dielectric profiles' intensities contrast.

In the Equation (3.43), the regularization term is defined in a spatial domain with image dimension of $N_x \times N_y$ [13].

$$Q_{EPR}(\varepsilon_r) = \sum_{x=1}^{N_x}\sum_{y=1}^{N_y} \lambda\varphi\left(\frac{\|\nabla\varepsilon_r\|}{\delta}\right), \;\; N_x \times N_y = NP_{new} \tag{3.43}$$

Image dimension in this case is referring to an area of a circular region that confined the detected object at iteration S with AS-ROI. Even though the reconstruction area has been reduced, the dimension of discretized search domain on FDTD cells 220×220mm^2 are still maintained.

Image gradients or edges in Equation (3.44) denoted as $\nabla\varepsilon_r$. Image gradients consisting of horizontal and vertical direction $\nabla\varepsilon_{r_a} = (\nabla_N, \nabla_E, \nabla_S, \nabla_W)$ as well as in diagonal direction $\nabla\varepsilon_{r_b} = (\nabla_{NE}, \nabla_{SE}, \nabla_{SW}, \nabla_{NW})$ [50].

$$\|\nabla\varepsilon_r\| = \frac{\partial\varepsilon_{r_a}}{\partial x} + \frac{\partial\varepsilon_{r_a}}{\partial y} + \frac{\partial\varepsilon_{r_b}}{\partial x} + \frac{\partial\varepsilon_{r_b}}{\partial y} \tag{3.44}$$

∇ in the Equation (3.44) means discrete derivative or first order gradient operator. Total image gradients $\|\nabla\varepsilon_r\|$ is a summation of gradients in all directions involved in the spatial domain. Image gradients of relative permittivity with respect to row x and column y in 8 directions or 8 neighbourhood pixels are obtained by using first derivative finite differences of image pixels as shown in Equation (3.45) until Equation (3.52) [121].

$$\nabla_{N_{(x,y)}} = \varepsilon_r(x, y) - \varepsilon_r(x-1, y) \tag{3.45}$$

$$\nabla_{NE_{(x,y)}} = \varepsilon_r(x-1, y+1) - \varepsilon_r(x, y) \tag{3.46}$$

$$\nabla_{E_{(x,y)}} = \varepsilon_r(x, y+1) - \varepsilon_r(x, y) \tag{3.47}$$

$$\nabla_{SE_{(x,y)}} = \varepsilon_r(x+1, y+1) - \varepsilon_r(x, y) \tag{3.48}$$

$$\nabla_{S_{(x,y)}} = \varepsilon_r(x+1, y) - \varepsilon_r(x, y) \tag{3.49}$$

$$\nabla_{SW_{(x,y)}} = \varepsilon_r(x+1, y-1) - \varepsilon_r(x, y) \tag{3.50}$$

$$\nabla_{W_{(x,y)}} = \varepsilon_r(x, y) - \varepsilon_r(x, y-1) \tag{3.51}$$

$$\nabla_{NW_{(x,y)}} = \varepsilon_r(x, y) - \varepsilon_r(x-1, y-1) \tag{3.52}$$

The initial equation of edge preserving regularization in Equation (3.42) and Equation (3.43) are converted into half quadratic regularization to simplify the minimization process, which introduces auxiliary regularization parameters with detailed explanation given in [18, 50, 125]. The term of half quadratic is due to interrelated quadratic connection between the reconstructed image and auxiliary regularization parameters [50].

Variable b_a in Equation (3.53) is an auxiliary regularization parameter in horizontal and vertical direction. Variable b_b which written in Equation (3.54) is used to denote auxiliary regularization parameter in diagonal directions [50].

$$b_a = \frac{\varphi'\left(\nabla\varepsilon_{r_a}/\delta\right)}{2\left(\nabla\varepsilon_{r_a}/\delta\right)} \tag{3.53}$$

$$b_b = \frac{1}{2}\left[\frac{\varphi'\left(\nabla\varepsilon_{r_b}/\delta\right)}{2\left(\nabla\varepsilon_{r_b}/\delta\right)}\right] \tag{3.54}$$

Auxiliary regularization parameters b_a and b_b are the first derivative of potential function φ, which functional for image diffusion or smoothing. These two auxiliary regularization parameters are called as weighting functions with the general assumptions made on its edge preservations are given in [13]. Parameter δ in the weighting functions is the gradient threshold that control the smoothing degree of regularization which corresponds to the presence of image gradient. In the availability of edges or large image gradient, the weighting functions approximately becomes zero. In contrast, weighting functions are much higher in homogenous areas that led to high smoothing degree.

By incorporating regularization scheme into FBTS [29], total gradient of relative permittivity is written as in Equation (3.55) with the regularization gradient given in Equation (3.56).

$$g_{\varepsilon_{r_{TOTAL}}} = g_{\varepsilon_{r_{FBTS}}} + g_{\varepsilon_{r_{EPR}}} \tag{3.55}$$

$$g_{\varepsilon_{r_{EPR}}} = -2\frac{\lambda}{\delta^2}\nabla\cdot\left(b_a\nabla\varepsilon_{r_a} + b_b\nabla\varepsilon_{r_b}\right) \tag{3.56}$$

Weighting functions and regularization gradient mentioned previously are obtained by taking Fréchet derivative of the regularization cost functional term [18, 29].

As listed in Table 3.1 [13, 50], three potential functions for edge preserving regularizations alongside its associated weighting functions are considered, which are utilized in most research papers concerning regularization.

Table 3.1: Edge Preserving Regularization Potential Function with its weighting functions

Potential function $\boldsymbol{\varphi}$	$\boldsymbol{\varphi(t)}$	$\boldsymbol{\varphi'(t)}$	$\boldsymbol{b_a}$	$\boldsymbol{b_b}$
Geman & Mc.Clure	$\frac{t^2}{1+t^2}$	$\frac{2t}{(1+t^2)^2}$	$\frac{1}{\left(1+\left(\frac{\nabla\varepsilon_{r_a}}{\delta}\right)^2\right)^2}$	$\frac{1}{2\left(1+\left(\frac{\nabla\varepsilon_{r_b}}{\delta}\right)^2\right)^2}$
Hebert & Leahy	$\log(1+t^2)$	$\frac{2t}{1+t^2}$	$\frac{1}{1+\left(\frac{\nabla\varepsilon_{r_a}}{\delta}\right)^2}$	$\frac{1}{2\left(1+\left(\frac{\nabla\varepsilon_{r_b}}{\delta}\right)^2\right)}$
Hyper Surfaces	$2\sqrt{1+t^2}-2$	$\frac{2t}{\sqrt{1+t^2}}$	$\frac{1}{\sqrt{1+\left(\frac{\nabla\varepsilon_{r_a}}{\delta}\right)^2}}$	$\frac{1}{2\sqrt{1+\left(\frac{\nabla\varepsilon_{r_b}}{\delta}\right)^2}}$

Both regularization coefficient λ and gradient threshold parameter δ are empirically determined. The regularization coefficient λ will be varied from 5.0×10^{-12} to 5.0×10^{-9}. The reason it is small in number is due to gradient values of FBTS falls about the same range, and hence the regularization effect can be balanced. The selection of 5.0 as a multiplier by considering that it is the middle number between 1.0 and 10.0, as to reduce risk of being too low or too high. Gradient threshold parameter δ are varied from 0.75 to 1.5, based on empirical observations. Optimal result by means of MSE level for both mentioned parameters will be generalized for later analysis. In the event that previous optimal values are considered misfit for the regularization, the whole process of observations shall be repeated until good result is obtained.

Regularization in the rescaled FBTS is started at iteration R, which determined by statistical observation and occurs later than iteration S. Total cost functional in Equation (3.41) is solved by using alternate minimization over weighting functions b_a and b_b with relative permittivity ε_r. At even iteration number which equal or larger than R, total cost functional is minimized over b_a^{n+1} and b_b^{n+1} with fixed ε_r^n, which can be calculated by using Equation (3.57) and Equation (3.58) [50].

$$b_a^{n+1} = \frac{\varphi'\left(\nabla {\varepsilon_r}_a^n/\delta\right)}{2\left(\nabla {\varepsilon_r}_a^n/\delta\right)} \tag{3.57}$$

$$b_b^{n+1} = \frac{1}{2}\left[\frac{\varphi'\left(\nabla {\varepsilon_r}_b^n/\delta\right)}{2\left(\nabla {\varepsilon_r}_b^n/\delta\right)}\right] \tag{3.58}$$

The term $(n+1)$ in this section refers to current iteration and n is the preceding iteration. Then for a fixed b_a^{n+1} and b_b^{n+1}, the new image estimate ε_r^{n+1} within the same iteration is obtained by minimizing total cost function in Equation (3.41) with conjugate gradient method.

On the other hand, at odd iteration number, reconstructed image profile ε_r^n is resulted from non-regularized FBTS process. Minimization by FBTS and regularized FBTS in AS-ROI is alternately applied to reconstruct both relative permittivity and conductivity. Nonetheless, regularized FBTS only involving relative permittivity in which conductivity is only minimized by FBTS. Rationale behind alternate minimization between regularized and non-regularized FBTS is to balance the effect of regularization towards FBTS and to avoid consequence from extreme values of regularization parameters. The ε_r^n shall then smoothed by using anisotropic diffusion by using Equation (3.59) [104].

$$\frac{\partial \varepsilon_r(x,y,t)}{\partial t} = div[g(\|\nabla \varepsilon_r(x,y,t)\|) \cdot \nabla \varepsilon_r(x,y,t)] \tag{3.59}$$

Regularization gradient obtained from even iteration number is imposed to the reconstructed image which only iterates once in that respective iteration of optimization to avoid over smoothing. Diffusivity function $g(\|\nabla \varepsilon_r(x,y,t)\|)$ is actually similar to previous weighting functions b_a and b_b for regularization, nonetheless the term is referring to Hebert and Leahy function [50]. The term t is the time evolution for the filter's iteration number. Deterministic algorithm for regularized FBTS is summarized as follows:

1: Assign initial guess for ε_r^0 , σ^0
2: Repeat
3: Compute b^{n+1} by means of previous image estimate ε_r^n
4: if $(iter \geq R)\&\&(iter\%2 == 0)$
5: Reconstruct dielectric profiles $(\varepsilon_r^{n+1}, \sigma)$ by minimizing $Q_{TOTAL}(\varepsilon_r, \sigma)$
6: end if
7: else if $(iter \geq R)\&\&(iter\%2 == 1)$
8: Reconstruct dielectric profiles $(\varepsilon_r^n, \sigma)$ by minimizing $Q_{FBTS}(\varepsilon_r, \sigma)$
9: Impose anisotropic diffusion on ε_r^n in spatial domain
10: end else if
11: Until convergence

3.5 Dielectric characterization of lung(s) model

Grayscale image of transverse CT scan of thoracic wall in Figure 3.8 is utilized as a reference to reconstruct lung(s) model in this research. It is referred as slice #00018 under test case R_014, which taken from The Cancer Imaging Archive (TCIA) Public Access

[142]. Slice thickness of the lungs images from the database is varied from 3mm to 6mm. Initial image resolution is $512 \times 512\text{mm}^2$.

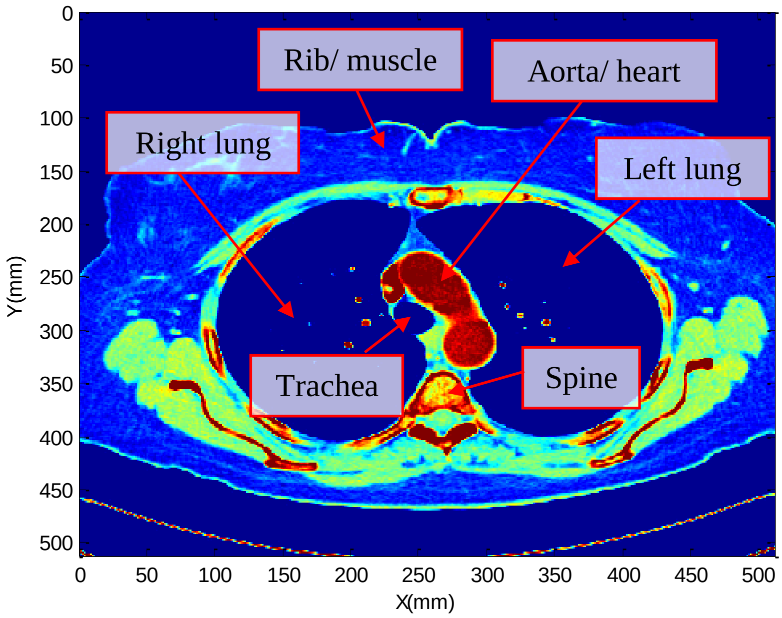

Figure 3.8: Transverse CT scan image of thoracic wall in grayscale [142]

Layers of dielectric properties and organs involved in the analysis will be adjusted in such a way according to several research papers concerning lung tumour detection, consequently the signal can propagate and scatter properly to allow object recognition. The research work emphasizes on studying the proposed technique in FBTS to locate and estimate the size of lung(s) tumour based on segmented layers of reconstructed image profiles obtained by AS-ROI. Similar to breast model, initial guess utilized for lung(s) tumour detection are empirically determined.

Three models are presented namely as Model #1, Model#2 and Model#3, with dielectric profiles values of layers or organs involved are taken from Cole-Cole expression for human tissues at 2GHz by Gabriel. [143]. Actual image needs to be rescaled down due to limited memory capacity, which only allows object size must be roughly less than 10000 pixels based on several simulations on single or even parallel computing. Otherwise, the program will halt. Apart from that, large number of pixels would increase the processing time. Thresholding segmentation to point out lungs area and rescaling process of the original image [142] are implemented in MATLAB.

Lungs for Model#1 is resized to 40% from the actual image consisting of 8087 pixels. Lung model utilized in Model#2 and Model#3 is rescaled to 60% which made of 9135 pixels, since it only involves the left lung. After being resized, the original grayscale image is then manually segmented based on its intensity values, in which lungs area is extracted out for used. Pixels which exterior to lungs are manually segmented out in Microsoft Excel. The selection of left lung over right lung is due to large contrast at the periphery between heart and left lung, that ease the segmentation process. Right lung on the other hand is adjacent to tracheal lobe which are of the same grayscale pixel intensity.

In these three models, dielectric values of lungs are calculated from volume ratio of best case scenario for normal lungs tissues, consisting of 66% air, 14% blood and 20% parenchyma [144]. Parenchyma dielectric value is determined by the assumption made by [145] which taking the average of inflated and deflated lungs as the best scenario. Calculations for relative permittivity and conductivity for lung(s) denoted as ε_{lung} and σ_{lung} are given in Equation (3.60) and Equation (3.61). In the equations, air is denoted as air, blood as bld, inflated lung(s) as $linf$ and deflated lung(s) is written as $ldef$.

$$
\begin{aligned}
\varepsilon_{r_{lung}} &= 66\%\left(\varepsilon_{r_{air}}\right) + 14\%\left(\varepsilon_{r_{bld}}\right) + 20\%\left(\varepsilon_{r_{linf}} + \varepsilon_{r_{ldef}}\right)/2 \\
&= 0.66(1.0) + 0.14(59.0) + 0.2(20.8 + 49.1)/2 \\
&= 15.91
\end{aligned}
\tag{3.60}
$$

$$\sigma_{lung} = 66\%(\sigma_{air}) + 14\%(\sigma_{bld}) + 20\%\left(\sigma_{linf} + \sigma_{ldef}\right)/2 \tag{3.61}$$
$$= 0.66(0.0) + 0.14(2.19) + 0.2(0.69 + 1.39)/2$$
$$= 0.51\text{Sm}^{-1}$$

Lungs and heart structure in the first model shown in Figure 3.9 is constructed based on segmented slice of thoracic area which applied in paper [146]. Heart profile values are directly taken from heart muscle in Cole-Cole expression [147] as given in Equation (3.62) and Equation (3.63).

$$\varepsilon_{r\,heart} = 55.80 \tag{3.62}$$

$$\sigma_{heart} = 1.91\text{Sm}^{-1} \tag{3.63}$$

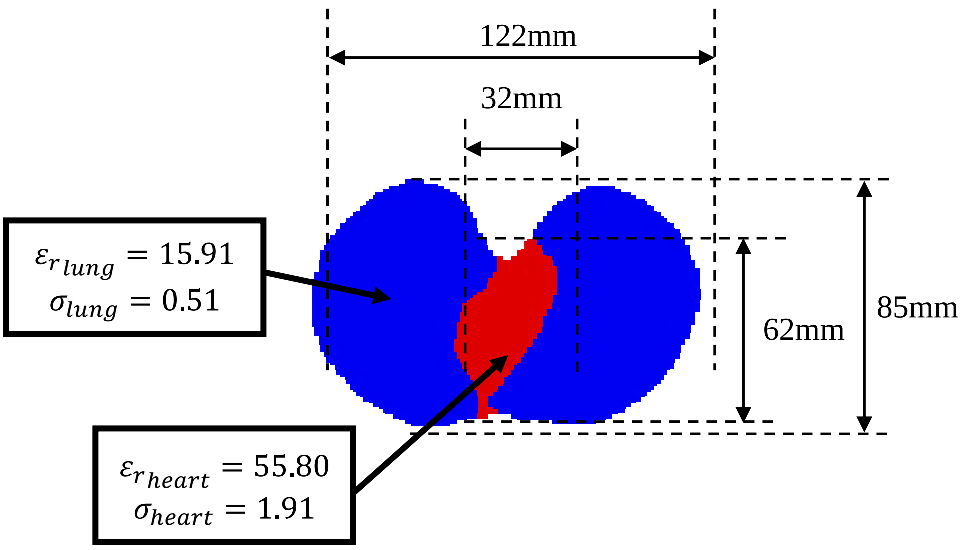

Figure 3.9: Geometrical configuration of Model #1

Constituent of tumour in Model#2 which illustrated in Figure 3.10 is based on Camacho and Tjuatja's study which containing 60% blood, 20% muscle and 20% of blood vessel [148]. Equation (3.64) and Equation (3.65) show the calculation of tumour profiles in the model, in which muscle and blood vessel are abbreviated as $mscl$ and bv, respectively.

$$\begin{aligned} \varepsilon_{r\,tumour_{Model\#2}} &= 60\%\left(\varepsilon_{r\,bld}\right) + 20\%\left(\varepsilon_{r\,mscl}\right) + 20\%\left(\varepsilon_{r\,bv}\right) \\ &= 0.6(59.0) + 0.2(53.3) + 0.2(43.1) \\ &= 54.68 \end{aligned} \tag{3.64}$$

$$\begin{aligned} \sigma_{tumour_{Model\#2}} &= 60\%(\sigma_{bld}) + 20\%(\sigma_{mscl}) + 20\%(\sigma_{bv}) \\ &= 0.6(2.19) + 0.2(1.45) + 0.2(1.17) \\ &= 1.84\text{Sm}^{-1} \end{aligned} \tag{3.65}$$

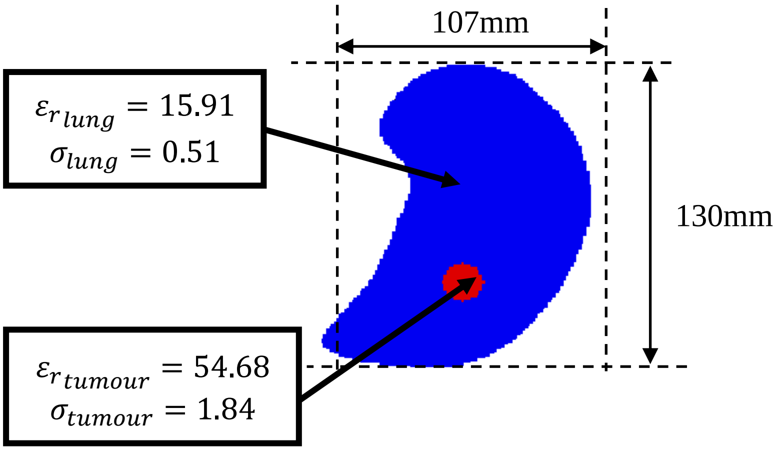

Figure 3.10: Geometrical configuration of Model#2

Dielectric profiles of lung tumour in Model#3 shown in Equation (3.66) and Equation (3.67) are determined by generalized the finding of research work by [149]. The tumour composition is taken from the mid-range value of ratio for cancerous tissues in relative to normal lung tissues with lung profiles obtained from Equation (3.60) and Equation (3.61). Geometrical configuration of Model#3 is shown in Figure 3.11.

$$\varepsilon_{r\,tumour_{Model\#3}} = (1.2 + 3)/2 \cdot \varepsilon_{r\,lung} \tag{3.66}$$
$$= (1.2 + 3)/2 \cdot 15.91$$
$$= 33.41$$

$$\sigma_{tumour_{Model\#3}} = (1.6 + 2)/2 \cdot \sigma_{lung} \tag{3.67}$$
$$= (1.6 + 2)/2 \cdot 0.51$$
$$= 0.918\mathrm{Sm}^{-1}$$

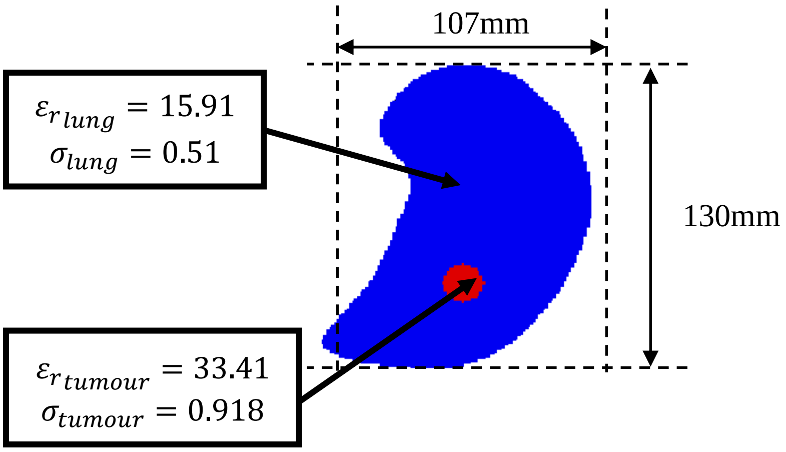

Figure 3.11: Geometrical configuration of Model#3

3.6 Image Quality Metric

Image quality metric used throughout in this research are mean squared error (MSE), relative error (RE) and Euclidean distance (ED). MSE is written as in Equation (3.68) [58].

$$MSE(\varepsilon_r) = \frac{1}{N_X N_y} \sum_{x=1}^{N_x} \sum_{y=1}^{N_y} \left[\rho_{actual}(x,y) - \rho_{spec}(x,y)\right]^2, \tag{3.68}$$
$$\rho \in (\varepsilon_r, \sigma)$$

$\text{MSE}(\varepsilon_r)$ in this research context is an average to a summation of the difference between image pixel values of the reconstructed image profiles ρ_{spec} in related to its actual synthetic values ρ_{actual} at coordinate (x, y) that confined in the region $(N_X \times N_y)$. Reconstructed image profiles ρ consisting of relative permittivity ε_r and conductivity σ. The term $spec$ is used to denote specified iteration in which image quality metric is performed on the reconstructed object.

MSE has been applied in several related studies [18, 19, 39, 49, 59] to describe the quality of reconstructed profiles. MSE is simple in algorithm, nevertheless based on observations thus far [58, 150], it can be said sufficient to explicitly explain the statistical precision level that constantly analogous to subjective evaluation of images. The function of MSE in this research is not only being a precision index measure of the reconstructed object. It is also applied to estimate optimal parameter settings for AS-ROI as well as edge preserving regularization by means of its level at the lowest value.

Since it measures the difference between two pixels at similar coordinates, therefore lower MSE would indicates better result in its accuracy. Based on observations that will be explicated in Chapter 4, MSE is much lower in conductivity profiles than relative permittivity due to its significantly low intensity values. However, it does not imply that the reconstructed image of conductivity is more accurate than relative permittivity.

Relative error (RE) which was also applied in [44–46] is added as the second precision index to determine the size accuracy of the reconstructed object. It can be calculated as in Equation (3.69). rad_{actual} is the actual radius of the phantom object and rad_{spec} is to denote radius which estimated by the AS-ROI algorithm.

$$RE = \left|\frac{rad_{actual} - rad_{spec}}{rad_{actual}}\right| \times 100 \tag{3.69}$$

The third precision index is a Euclidean distance (ED) to measure localization error between the exact centre coordinate and the detected object placement. It has been applied in [26, 46] for the same purpose, which also asses localization accuracy. The formula of ED is expressed in Equation (3.70).

$$ED = \sqrt{\left(offsetX_{act} - offsetX_{spec}\right)^2 + \left(offsetY_{act} - offsetY_{spec}\right)^2} \tag{3.70}$$

$offsetX_{act}$ and $offsetY_{spec}$ are the actual offset values in x and y directions. Meanwhile, $offsetX_{spec}$ and $offsetY_{spec}$ are the detected offset values by the AS-ROI. Offset values in this research framework are referring to the distance between object and centre coordinate of FDTD at (112,112).

3.7 Concluding Remarks

This chapter has underlined processes involved in the proposed technique. Summary of the overall process flow has been presented in the first section. FBTS algorithm along with its modelling setup for simulation was enlightened in the second section. A new rescaling approach by AS-ROI which embedded inside FBTS has been presented in the third section. The rescaling method is a non-iterative technique with resolution level maintained throughout the reconstruction process. The fourth section explicated on the combined technique of AS-ROI with edge preserving techniques: edge preserving regularization imposed on fields' gradient and edge preserving filter by means of anisotropic diffusion imposed on the relative permittivity profile. Characterization of three lung(s) phantom model has been described in later section. The last section emphasized on three types of image quality metric utilized in this research work. The metrics measure the fidelity of the reconstruction technique in terms of pixel accuracy in the investigation domain, object's size and localization accuracy.

CHAPTER 4

RESULTS AND DISCUSSION

Focal point of this research is to combine an Automated Scaling Region of Interest (AS-ROI) with Forward-Backward Time-Stepping (FBTS) method, to focus on the object's region for image reconstruction. Edge preserving smoothing filter and edge preserving regularization were studied as auxiliary values to the research work, which further enhance the accuracy of unknown object from the observed fields. The efficiency of the proposed work is validated by numerical analysis utilizing several synthetic object models. Analysis in this research include edge preserving techniques, AS-ROI in FBTS, followed with hybrid AS-ROI with edge preserving regularization in FBTS.

Analysis are divided into two parts. In the first part in Section 4.1 up to 4.5, reconstruction of simple objects which taken after breast dielectrical profiles from Debye model are considered. The geometry is made up of two layers which immersed in free space as coupling medium, encompasses of fatty tissue and fibroglandular of breast. The object geometry however, only consists of simple shapes which does not resemble human breast. The second part in Section 4.6 up to 4.7 present findings on lung(s) model, that is also made of two layers containing lung(s) tissue and tumour. The observation points will be the entire detected region of interest (ROI). Mean squared error (MSE), relative error (RE) and Euclidean distance (ED) will be used throughout as an image similarity index to measure the accuracy of the reconstructed object. Termination criterion of convergence is predetermined at 100^{th} iteration for all analysis except for finding parameter settings of edge preserving regularizations. In order to measure computational time difference, the number of antennas is maintained at 12 units to encircle the unknown object for all analysis.

4.1 Image reconstruction of simple object at varied frequencies

In the first analysis, reconstruction of simple objects in three geometrical shapes are considered, which analysed at different frequencies ranging from 1GHz to 4GHz. All these four frequencies (1GHz, 2GHz, 3GHz and 4GHz) correspond to the stability condition of FDTD simulation as discussed in Chapter 2, Section 2.2.2. Frequency level of incident waves is inversely proportional to the penetration depth that affect the strength of signal passing through mediums' layers of varied dielectric properties [151]. Therefore, simulations in this section would analyse an optimal frequency that able to characterize the object's geometry with sufficient penetration level. In particular, the four frequencies were studied to suit object and ROI's size in 40mm radius with a given dielectric profiles. The finding of optimal frequency will be generalized to be used for later analysis, since object and ROI size are limited to FDTD fixed size.

Analysis domain on FDTD cell has a dimension size of $220 \times 220\text{mm}^2$ which utilized for all analysis in this research. Each layer thickness or dielectric properties of actual object and its initial guess are given in Table 4.1. These dielectric values will be used for all analysis objects which taken after Debye breast model. All objects to be analysed are shown in Figure 4.1, for Shape#1, Shape#2 and Shape#3. Shape#1 has width and length of 39mm and 39mm, respectively. Meanwhile, for Shape#2, the width and length are 39mm and 20mm respectively. As for Shape#3, the multiple circulars have radius of 3mm, 5mm and 7mm (from left to right). Varied shapes were analysed to observe the consistency of the tested frequencies.

Table 4.1: Dielectric properties settings for breast model

Layer	Actual		Initial guess	
	ε_r	σ	ε_r	σ
Fat	9.98	0.18	13.70	0.10
Fibroglandular	21.45	0.45	13.70	0.10
Background (free space)	1.00	0.00	1.00	0.00

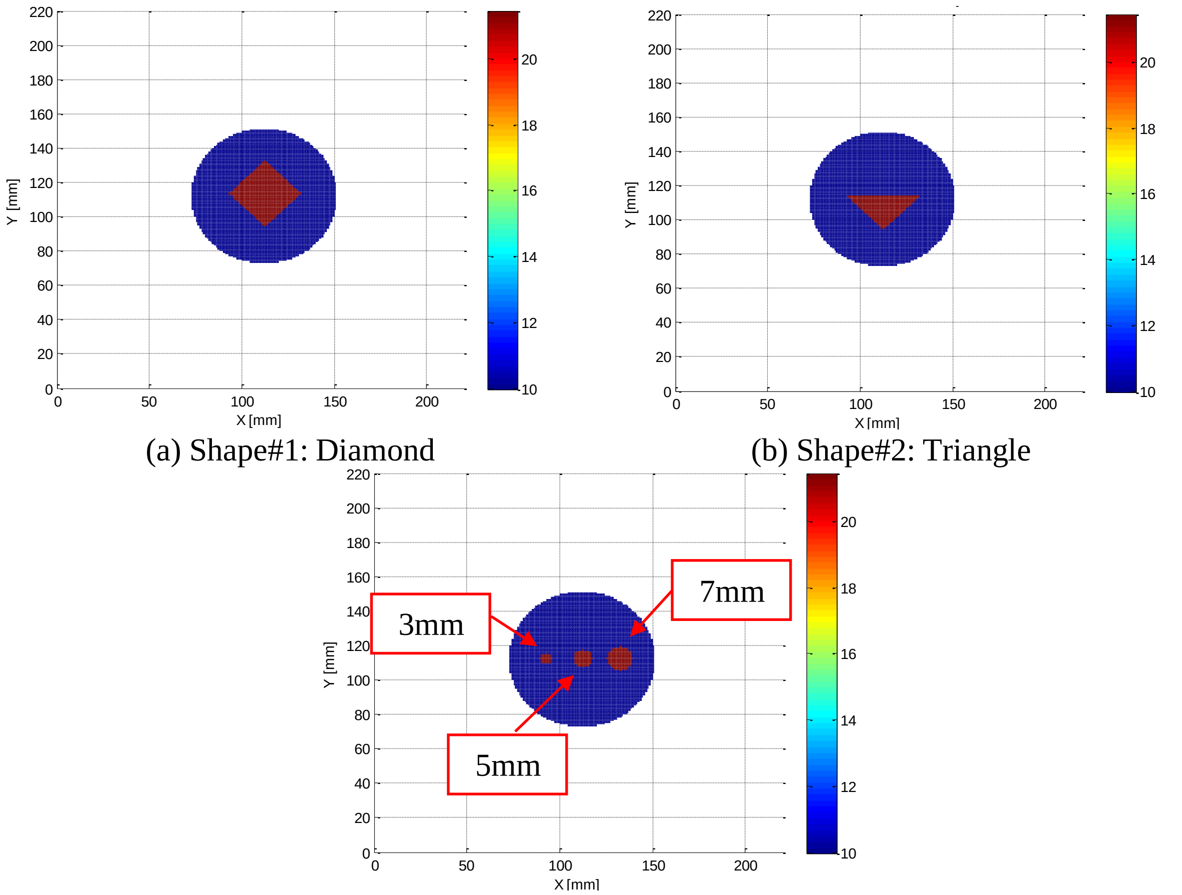

(a) Shape#1: Diamond

(b) Shape#2: Triangle

(c) Shape#3: Multiple circulars

Figure 4.1: Actual relative permittivity of phantom model in varied shapes

In terms of subjective evaluation, only reconstructed images of Shape#1 are presented as the frequency effect on all three models are similar. Figure 4.2 shows cross-sectional top and side view of relative permittivity images of Shape#1 with various frequency ranging from 1GHz to 4GHz. Cross-sectional top view of relative permittivity image which reconstructed at 1GHz in Figure 4.2(a) is blurred at the edges. Nevertheless, the lossless background is well reconstructed in which appear to be homogenous in all directions. Severe fluctuations can be observed in its corresponding cross-sectional side view in Figure 4.2(e). This indicate that the signal penetration was higher at the background layer with lower dielectric properties, nonetheless getting weaker inside the object of higher dielectric properties. At 2GHz which illustrated in Figure 4.2(b) and 4.2(f), blotches appeared inside the reconstructed object. However, the background intensities were fairly homogenous. Internal layer of object is not perfectly reconstructed due to similar reason as for 1GHz frequency.

The geometry of Shape#1 generated by FBTS at 3GHz in Figure 4.2(c) is clearly close to the actual image, in which blotches appeared in the reconstructed object by 2GHz frequency has diminished. Edges line exhibited in Figure 4.2(g) also approximates to the actual trail compared to other frequency settings. At 4GHz, distortions in the reconstructed image in both background and object's layers can be seen in Figure 4.2(d). Distortions are more notable in the cross-sectional side view in Figure 4.2(h). This finding is analogous to related study [54], which also found that 4GHz frequency leads to nonlinearity of the inversion solution that deteriorates the reconstructed image.

MSE levels of relative permittivity images is shown in Figure 4.3. It also reached its lowest MSE value of 1.18 at 3GHz which applicable for all three geometrical shapes that have been analysed. From Figure 4.2 and 4.3, optimal result for permittivity image for Shape#1 is obtained by using the frequency of 3GHz. Numerical evaluations indicated by MSE in this analysis are comparable to the subjective evaluations that had been discussed earlier.

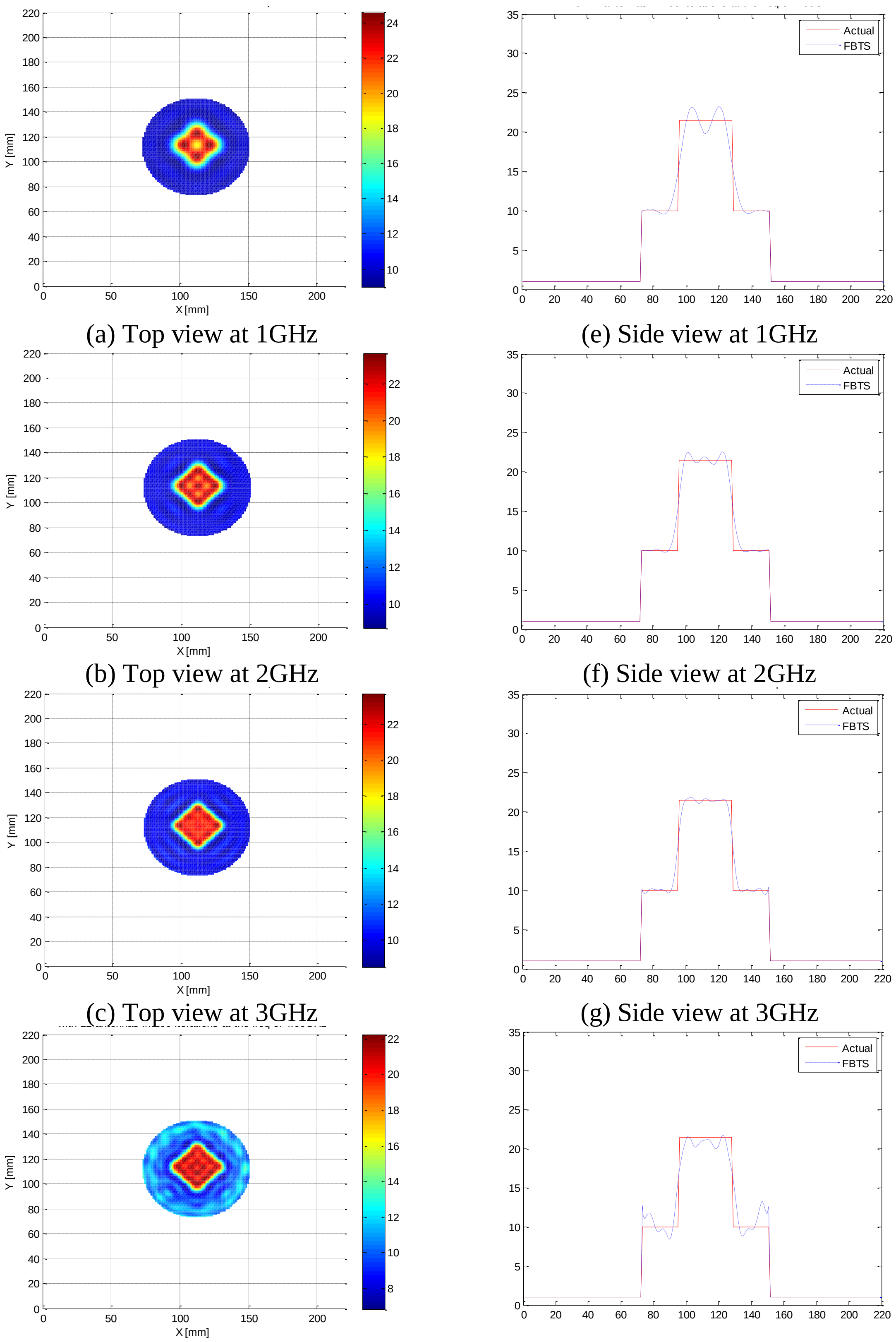

(a) Top view at 1GHz

(e) Side view at 1GHz

(b) Top view at 2GHz

(f) Side view at 2GHz

(c) Top view at 3GHz

(g) Side view at 3GHz

(d) Top view at 4GHz

(h) Side view at 4GHz

Figure 4.2: Cross-sectional view of relative permittivity images (Shape#1) in x-y plane at 100th iteration obtained at varied frequencies

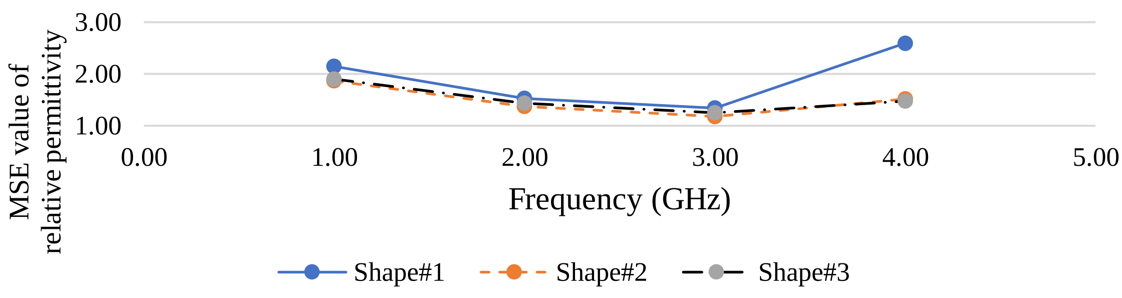

Figure 4.3: MSE values of relative permittivity images of Shape#1, Shape#2 and Shape#3 reconstructed at varied frequencies

The conductivity profile which analysed at different frequencies are illustrated in Figure 4.4. Dissimilar to relative permittivity, conductivity images started to deteriorate and yields clear ring objects at 3GHz as shown in Figure 4.4(c). Distortions were visible in the cross-sectional side view Figure 4.4(g). From Figure 4.4, optimal results of conductivity images can be obtained with frequency lower than 3GHz. It can be said that instability of the inversion solution has started at 3GHz for conductivity images. Precise evaluation is made by using MSE result, since there is no substantial difference between cross-sectional view of reconstructed images at 1GHz and 2GHz. Accuracy level of conductivity is shown in Figure 4.5. The MSE level of conductivity in Figure 4.5 reaches the lowest value of 8.95×10^{-4} at the frequency of 2GHz for all three shapes.

In order to have fair result between relative permittivity and conductivity images, frequency at 2GHz is suffice to generate considerably good result for both permittivity and conductivity of simple objects, based on subjective and quantitative evaluation. On top of that, penetration depth is inversely proportional to frequency and relative permittivity [152]. Higher frequency or relative permittivity decreases the penetration depth of incident fields which attenuate the capability of an inversion technique. Therefore, all subsequent analyses shall be investigated with 2GHz frequency considering that later analyses shall utilized higher relative permittivity values.

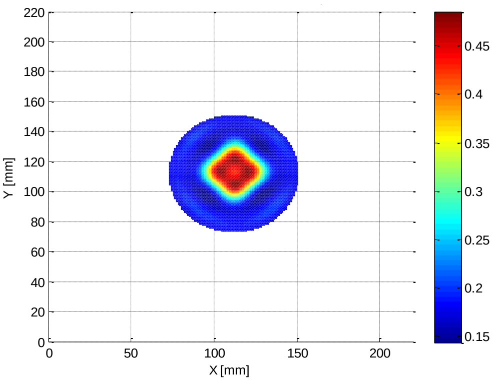

(a) Top view at 1GHz

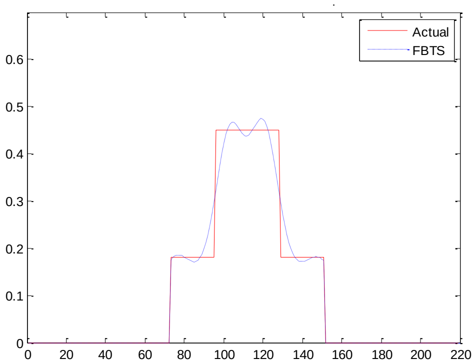

(e) Side view at 1GHz

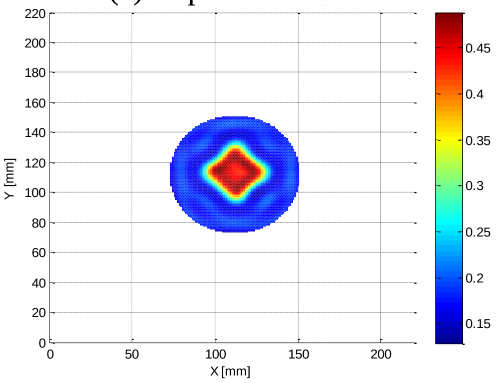

(b) Top view at 2GHz

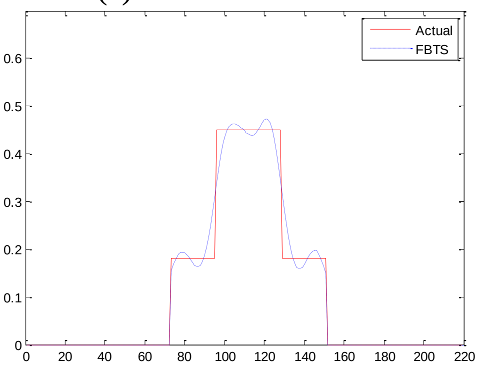

(f) Side view at 2GHz

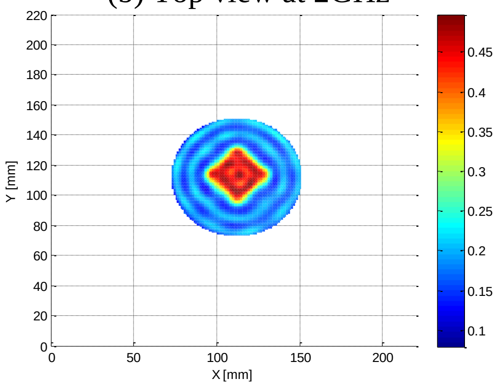

(c) Top view at 3GHz

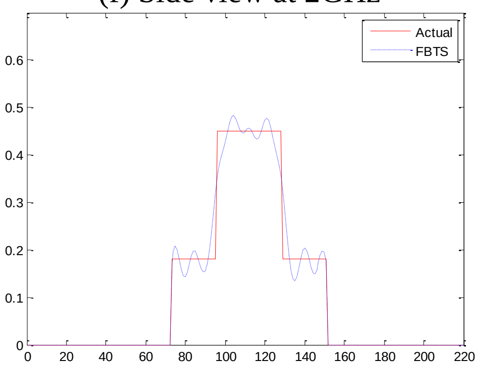

(g) Side view at 3GHz

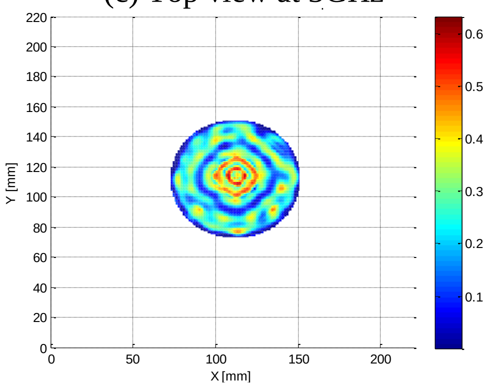

(d) Top view at 4GHz

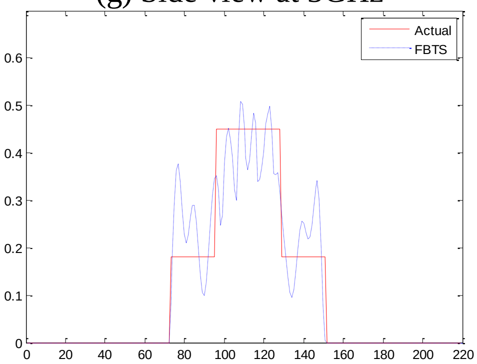

(h) Side view at 4GHz

Figure 4.4: Cross-sectional view of conductivity images (Shape#1) in x-y plane at 100th iteration at varied frequencies

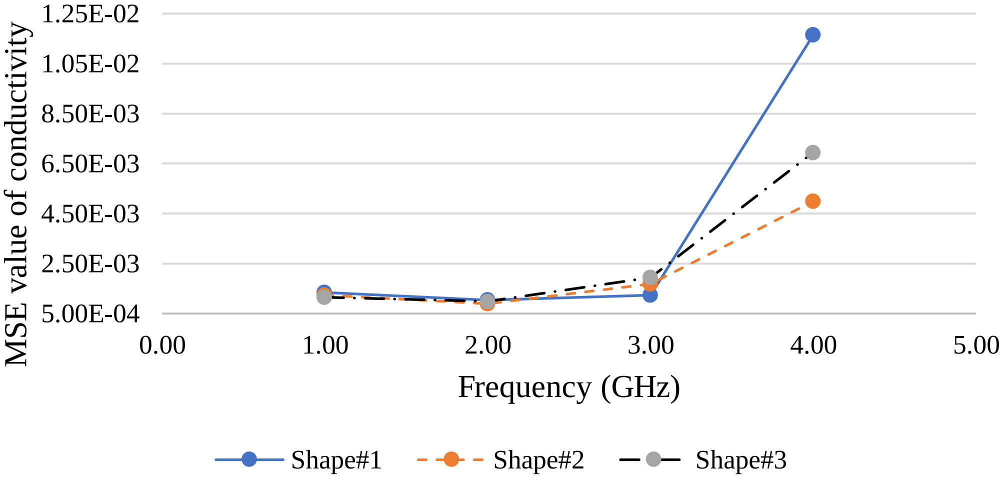

Figure 4.5: MSE values of conductivity images of Shape#1, Shape#2 and Shape#3 reconstructed at varied frequencies

4.2 Edge preserving smoothing filter

In this analysis, several edge preserving smoothing filters were studied. Edge preserving smoothing filters is utilized as a pre-processing process prior to regularization method. The combined edge preserving smoothing filters and regularization is proven effective in preserving image details as discussed in Section 2.4.1. Filters are imposed directly on the reconstructed output at each iteration of optimization. This is to eliminate artifacts in the reconstructed images due to nonlinearity and ill-posed problems of inverse scattering method. Despite being a simple input-output process, the effect on the accuracy improvement is quite significant.

Filters chosen for analysis were median filter family and anisotropic diffusion. Filter selection is generally due to its good performance as discussed in the Chapter 2 under section 2.31 and 2.33 for median filter family and anisotropic diffusion, respectively. Despite with some disadvantages listed in several papers [85, 86, 94–98] for median filter in eliminating noise, it is still applied in this research work as the aim is to alleviate the ill-posedness and nonlinearity of inverse problem under noise free environment setting. The selection of anisotropic diffusion to be applied on the reconstructed profiles is mainly due to its algorithm [82, 104–110, 112] that is comparably similar to regularization process [13, 50]. This is to ensure balance diffusion effect on the scattered fields as well as on the reconstructed profiles.

Median filter family that are considered in this analysis includes median filter, weighted median and Adaptive weighted median filter with optimal size of $3 \times 3\text{mm}^2$. Kernel size of Adaptive weighted median filter is expanded up to $5 \times 5\text{mm}^2$, as larger kernel will oversmoothed the object. Kernel size of each filter is empirically determined based on its MSE results. In anisotropic diffusion, there are several options of potential function that can be used for regularization purpose. In this analysis only Geman & McClure potential function is applied. This is to synchronize the weighting function as applied in edge preserving regularization for smoothing effect, which will be discussed in Section 4.3. Parameters for gradient threshold and weighting for image diffusion are empirically determined, which set to 1.25 and 0.1, respectively. These parameters are applied for both relative permittivity and conductivity.

Figure 4.6 shows comparison of cross-sectional top view between reconstructed relative permittivity profiles of actual, FBTS and filtered FBTS. The object model to be analysed is shown in Figure 4.6(a), which is a U-shaped object in 33mm for both height and width dimension. The gap of the U-shaped is in 7mm. The selection of the U-shaped pattern is to study the capability of edge preserving smoothing filter and regularization to assist the FBTS in detecting depth of the U curve and preserving its multiple edges.

In terms of relative permittivity values, all filtered images show substantial improvement in comparison to the reconstructed image by FBTS. Note that visible artifacts or ring objects which exists in FBTS result as in Figure 4.6(b) are vanished as iterative edge preserving smoothing filters are applied, which illustrated in Figure 4.6(c) until Figure 4.6(f).

From Figure 4.6(f), the U-shaped object becomes more homogenous in its intensities level by using anisotropic diffusion, as the smoothing effect is bounded by the detected edges unlike median filter family or any other filters. As explained in Section 2.3.2, smoothing by anisotropic diffusion is strongly imposed on non-edges area nevertheless has slight effect on edges.

Figure 4.7 shows comparison of cross-sectional side view for the reconstructed dielectric profiles at the centre image (112,112) between actual, FBTS and anisotropic diffusion filtered FBTS. In Figure 4.7(a), the curve or gap of between two poles for relative permittivity which constitute the U-shape is more pronounced for the anisotropic diffusion filtered FBTS, as it getting deeper near to the actual line compared to the reconstructed image by FBTS. In contrast to relative permittivity, the edges of conductivity image in Figure 4.7(b) did not approaching the actual edges. This is due to incorrect estimation of parameter settings applied to conductivity, as all parameters are empirically tuned for relative permittivity image. Smoothing degree on conductivity images is therefore applied accordingly to the availability of gradient in relative permittivity, in spite of some edge pixels of conductivity are misclassified as homogeneous area and vice versa. Consequently, some conductivity pixels are over smoothed as the cross-sectional line appear higher than the actual.

Figure 4.8 and Figure 4.9 show accuracy level for dielectric profiles of FBTS and filtered FBTS. From Figure 4.8, all filtered relative permittivity achieve lower MSE than FBTS, in which the accuracy for all filtered images are enhanced. Correspond to its cross-sectional top and side view, anisotropic diffusion contributes the highest accuracy for relative permittivity with 13.13% decrement in MSE level compared to FBTS as the smoothing degree for each pixel is determined by the occurrence of edges and non-edges. Median family only contributes about 2.71% decrement in average for relative permittivity.

The main reason for inferior results of median family is pixels are treated by windowing kernel, in which uncorrupted pixels might be treated in the same way as the corrupted pixels.

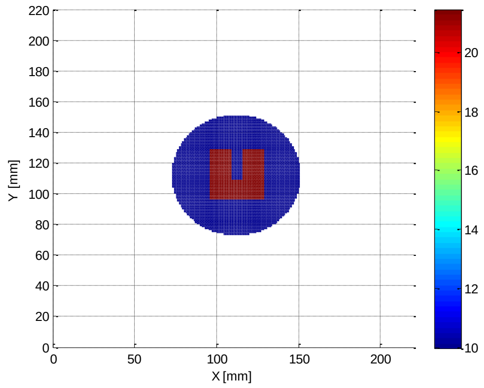

(a) Actual object

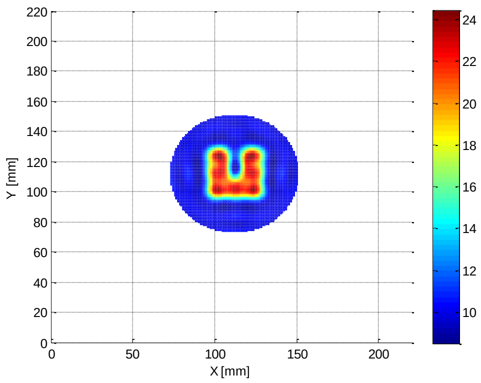

(b) FBTS

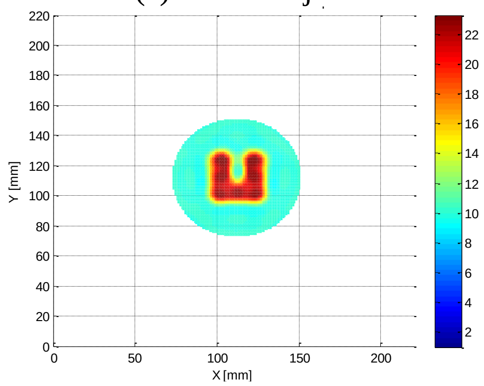

(c) Median filtered FBTS with kernel size of $3 \times 3\text{mm}^2$

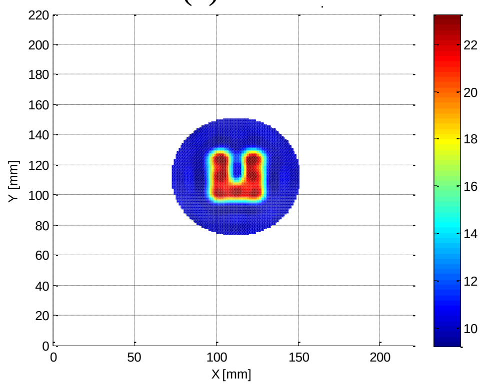

(d) Weighted median filtered FBTS with kernel size of $3 \times 3\text{mm}^2$

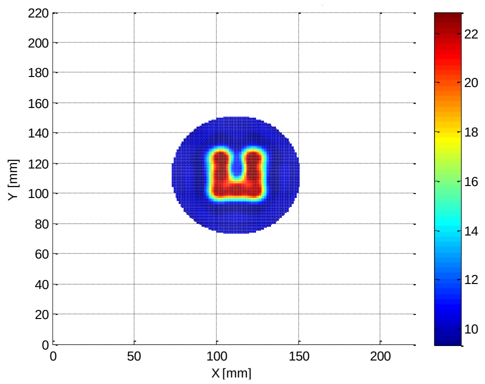

(e) Adaptive weighted median filtered FBTS with kernel size of 3×3 to $5 \times 5\text{mm}^2$

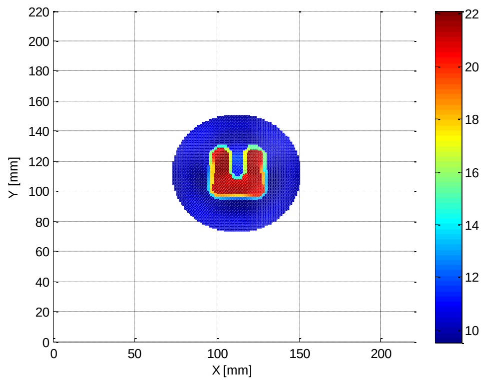

(f) Anisotropic diffusion filtered FBTS

Figure 4.6: Cross-sectional top view of relative permittivity images in x-y plane at 100th iteration for various filters in FBTS

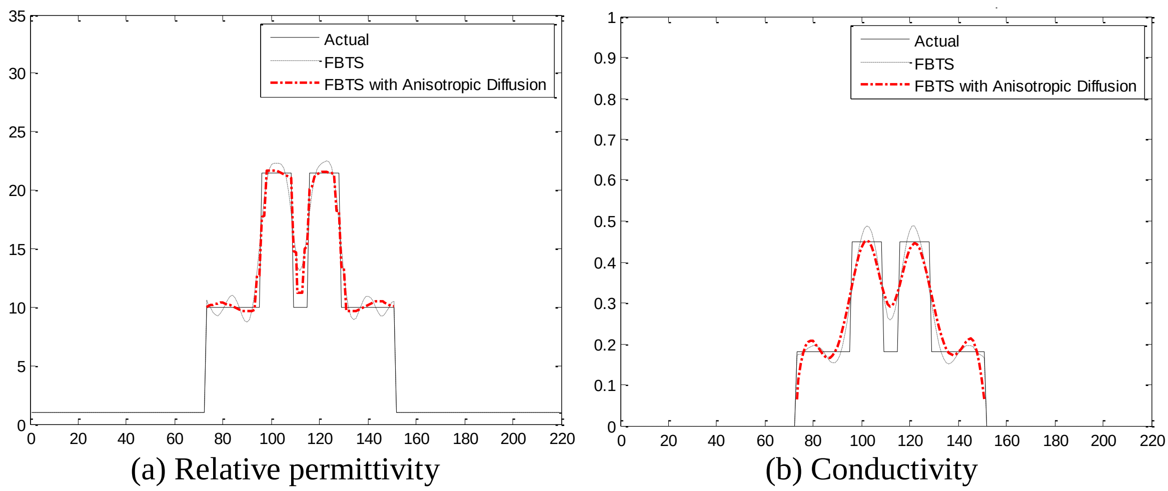

Figure 4.7: Cross-sectional side view along the x-axis at 100th iteration of the actual image, reconstructed image by FBTS and reconstructed image by iterative anisotropic diffusion in FBTS

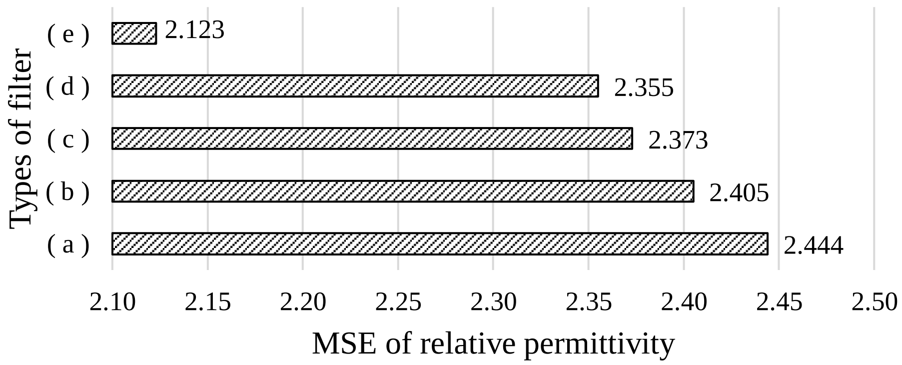

Figure 4.8: MSE values of relative permittivity images using (a) FBTS (b) Median filter with kernel size of $3 \times 3\text{mm}^2$ (c) Weighted median filter with kernel size of $3 \times 3\text{mm}^2$ (d) Adaptive weighted median filter with kernel size of 3×3 to $5 \times 5\text{mm}^2$ (e) Anisotropic diffusion

In contrast to relative permittivity outcome, conductivity filtered image by anisotropic diffusion in Figure 4.9 has the lowest accuracy with MSE level increased about 106.58%. Median filtered images of conductivity nevertheless show slight improvement with average decrement of 3.71% in MSE. Other than being affected by non-optimal parameters of filters, the inefficiency of FBTS in reconstructing conductivity images [54] also contribute to inferiority performance of filtering towards conductivity. Table 4.2

summarizes the MSE level for the reconstructed object by FBTS and filtered FBTS in which the lowest value for each profile were highlighted.

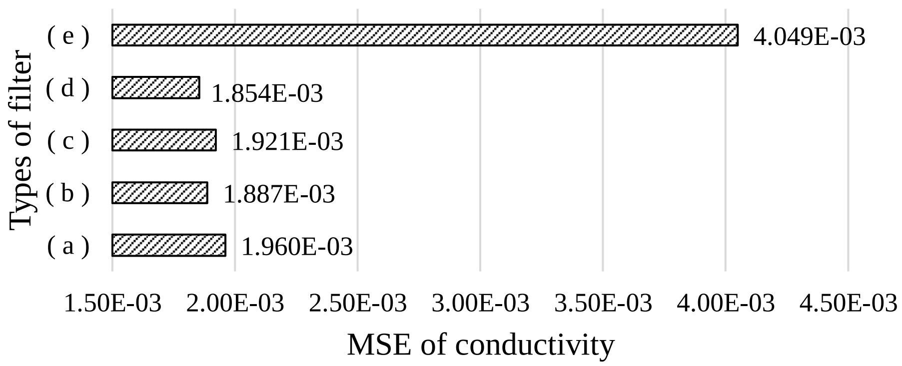

Figure 4.9: MSE values of conductivity images using (a) FBTS (b) Median filter with kernel size of $3 \times 3\text{mm}^2$ (c) Weighted median filter with kernel size of $3 \times 3\text{mm}^2$ (d) Adaptive weighted median filter with kernel size of 3×3 to $5 \times 5\text{mm}^2$ (e) Anisotropic diffusion

Table 4.2: MSE level of unfiltered and filtered FBTS

Reconstructed image obtained by	MSE of ε_r	MSE of σ
FBTS	2.444	1.96×10^{-3}
Median filtered FBTS	2.405	1.887×10^{-3}
Weighted median filtered FBTS	2.373	1.921×10^{-3}
Adaptive weighted median filtered FBTS	2.355	$\mathbf{1.854\times10^{-3}}$
Anisotropic diffusion filtered FBTS	**2.123**	4.049×10^{-3}

4.3 Edge Preserving Regularization

Edge preserving regularization is an extended version of anisotropic diffusion which has been proven remarkable in improving the accuracy of the reconstructed image. It has added elements that modifies gradients of reconstructed image as well as gradients of conjugate gradient method. Three potential functions are considered, encompasses of Geman

& McClure, Hebert & Leahy and Hyper Surfaces which acting separately, on relative permittivity and conductivity.

The analysis is started with finding optimal parameter settings for each potential function by maintaining the value of gradient threshold for relative permittivity and conductivity at 1.0 and 0.32, respectively. Gradient threshold parameter values are empirically determined. The value of regularization coefficient is varied from 5.0×10^{-12} to 5.0×10^{-9}, which correspond to conjugate gradients of FBTS [18, 49]. Object for edge preserving regularization analysis is similar to Section 4.2. Image reconstructions are carried out in 51 iterations, which half the process for all other analysis. The rationale behind choosing odd number for finding parameter settings of regularization as the regularization process was opted to be ended at odd iteration number until convergence criterion is met.

The MSE results are shown in Figure 4.10 and Figure 4.11. From both figures, regularization with Geman & McClure potential function and regularization coefficient of 5.0×10^{-10} contributes the highest improvement, in which optimal to the simulation settings. The inverse scattering is intrinsically nonlinear and hence volatile to any changes. From the MSE results, regularization coefficient higher than 5.0×10^{-10} can be considered too high that cause instability of the FBTS that led to improper estimation of dielectric profiles after the regularization process. On the other hand, regularization coefficient which lower than 5.0×10^{-10} are considered too low to provide significant regularization effect towards the reconstructed image profiles.

In what follows, only Geman & McClure potential function is considered for both regularization purpose and anisotropic diffusion filter in Section 4.2. Therefore, the smoothing effect on fields by regularization would be analogous to the smoothing of reconstructed image profiles by the anisotropic diffusion filter.

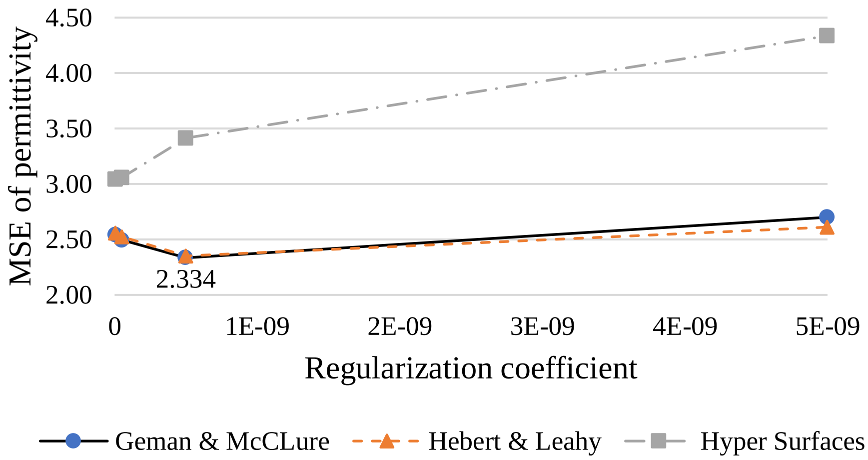

Figure 4.10: MSE values of relative permittivity images for various potential functions in edge preserving regularization

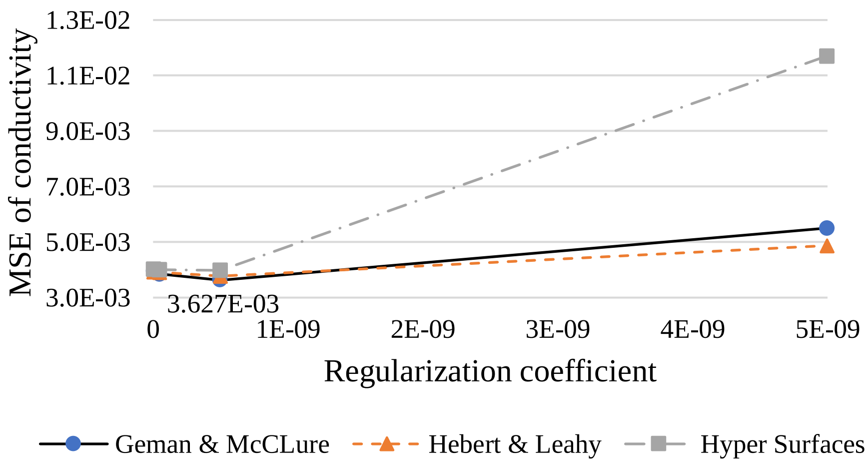

Figure 4.11: MSE values of conductivity images using for various potential functions in edge preserving regularization

The analysis for determine optimal parameters settings is continued by using varied threshold parameter for relative permittivity, which ranging from 0.75 to 1.5 with a deviation of 0.25. The threshold parameter of conductivity is still maintained at 0.32 to observe the regularization effect, on condition that only one of dielectric properties is treated. As discussed in Chapter 2, edge preserving regularization is commonly imposed on all reconstructed profiles.

Results of dielectric properties accuracies are illustrated in Figure 4.12 and Figure 4.13. From Figure 4.12, ideal value for gradient threshold which acted on relative permittivity is 1.25. With the threshold parameter imposed on conductivity maintained at the same value, Figure 4.13 shows the regularizing effect of varying relative permittivity parameters on conductivity image, only to find the best value of regularization coefficient. Similar to previous outcome, optimal results for both relative permittivity and conductivity in Figure 4.12 and Figure 4.13 are obtained at regularization coefficient of 5.0×10^{-10}. Up to this point in this section, MSE values are only used to determine optimal parameter settings of regularization and are not compared to the reconstructed image by FBTS.

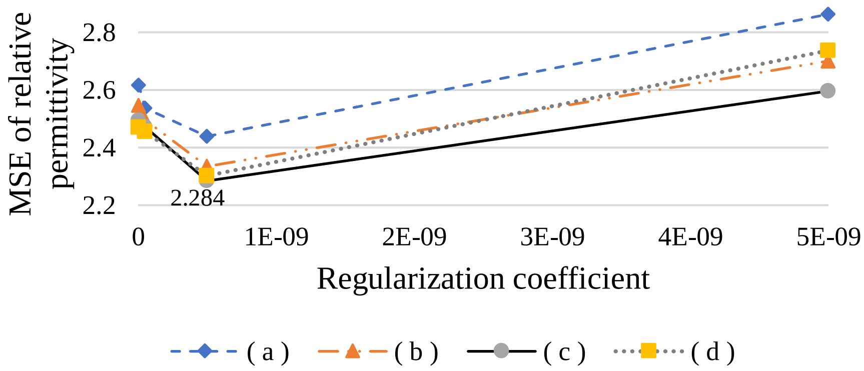

Figure 4.12: MSE values of relative permittivity images with varied regularization coefficient and varied threshold parameter for relative permittivity of (a) 0.75 (b) 1.0 (c) 1.25 (d) 1.5

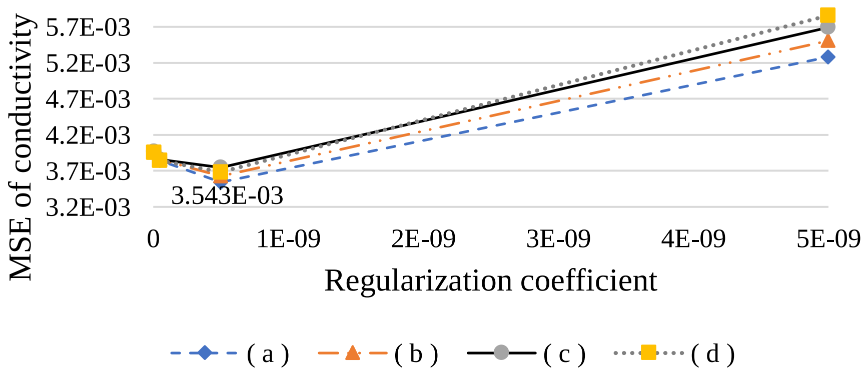

Figure 4.13: MSE values of conductivity images with varied regularization coefficient and varied threshold parameter for relative permittivity of (a) 0.75 (b) 1.0 (c) 1.25 (d) 1.5

Figure 4.14 and Figure 4.15 show comparison of accuracy level between regularized cases by combined method of edge preserving regularization with FBTS and non-regularized cases in FBTS at various starting number of iterations. The MSE values for relative permittivity and conductivity images reconstructed by FBTS are 2.44 and 1.96×10^{-3}, respectively. For relative permittivity images in Figure 4.14, regularization enhance the accuracy even it is applied in the first iteration which attains MSE of 2.17 in comparison to FBTS at 2.44. However, the effect is more prevalent at 20^{th} iteration, which reaches the lowest value at 1.91. Similar to anisotropic diffusion, the smoothing degree by regularization is based on the occurrence of edges or gradient. Any deterministic inversion technique including FBTS would require some time to converge. At early iteration the reconstructed images have not fully developed as the initial guess for image reconstruction is insufficient to estimate the unknown object. Therefore, edges are hardly distinguished from non-edges area. Imposing regularization towards erroneous pixels would cause solution to be inaptly treated. At iteration later than 20^{th}, solution is considered insufficiently regularized, which leads to lowering the accuracy level.

Since only regularization parameters of relative permittivity are varied, note that MSE of conductivity images are larger for regularized cases compared to the non-regularized with FBTS as in Figure 4.15. Maintaining the regularization gradient threshold value imposed to conductivity surely deteriorates its reconstructed image, as there is no effort to make it compatible with the object. Despite that, the whole regularization process still able enhance the quality image of relative permittivity significantly.

Based on the results reported in Figure 4.12 up to 4.15, only relative permittivity is considered to be regularized for later analysis. Conductivity image on the other hand is only optimized by conjugate gradient method in FBTS since it is proven that unregularized conductivity would not affect the regularized relative permittivity. Plus, it would reduce the complexity in determine regularization parameter settings.

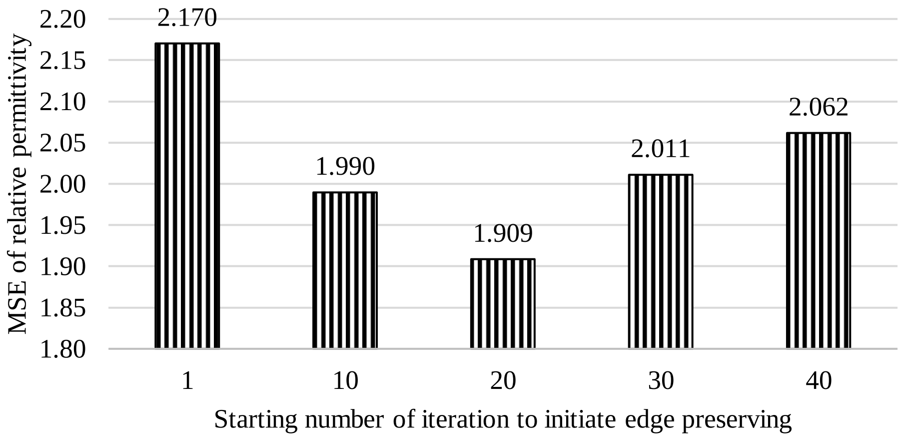

Figure 4.14: MSE values of relative permittivity images with edge preserving regularization in FBTS at varied starting number of iterations

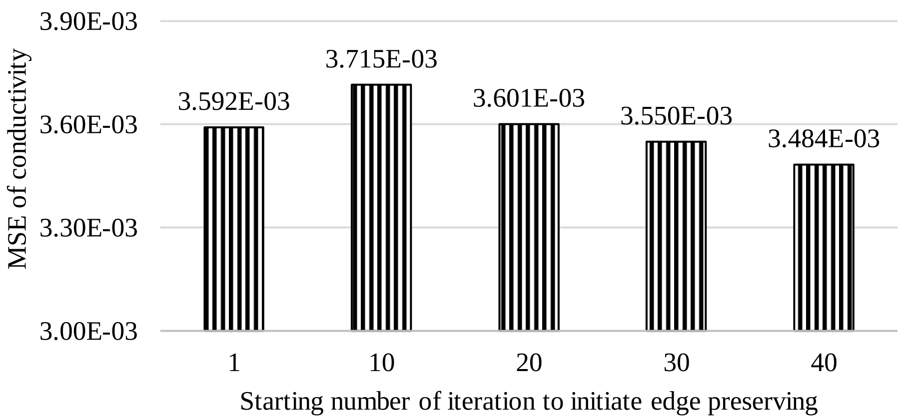

Figure 4.15: MSE values of conductivity images with edge preserving regularization in FBTS at varied starting number of iterations

4.4 Automated Scaling in Region of Interest (AS-ROI)

Similar to analysis for edge preserving regularization, starting number to initiate the rescaling process by AS-ROI also affect the quality of image reconstruction. Since relative permittivity image is more accurate than conductivity, it is used in AS-ROI process to define the new reconstruction area. Therefore, the finding is relied on the accuracy of relative permittivity, which makes conductivity less significant in this analysis. The whole pixels of the newly defined ROI would be the test points in all AS-ROI analysis. Figure 4.16 shows the accuracy of reconstructed images in terms of MSE level at various starting number of iteration for AS-ROI. Cost functional for optimization is shown in Figure 4.17. Both suggests that optimal iteration number to start the AS-ROI is at 30th iteration out of 100 iterations in total for image reconstruction. It is due to similar reason as edge preserving regularization in Section 4.3. Providing that when AS-ROI start too early, incorrect area will be segmented for reconstruction due to erroneous of edge pixels. On the other hand, the rescaled investigation area would insufficiently be optimized as the convergence criterion is fixed to 100th iteration in all analyses.

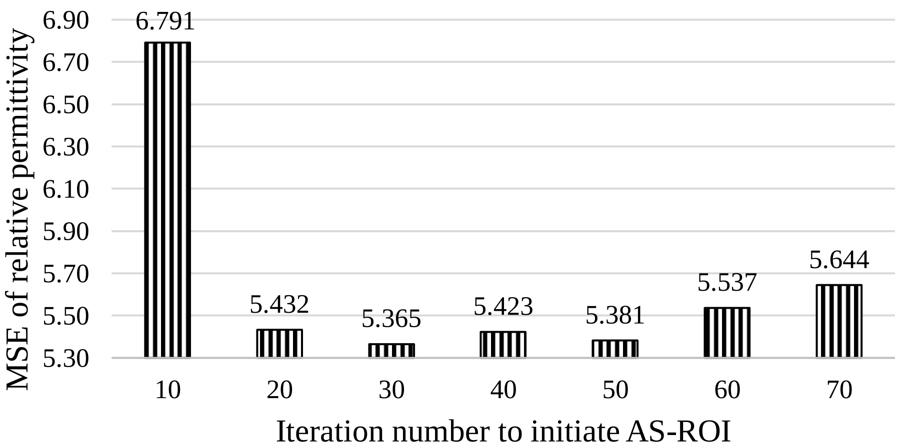

Figure 4.16: MSE of relative permittivity with varied starting number of iteration to initiate AS-ROI for object at centre coordinate

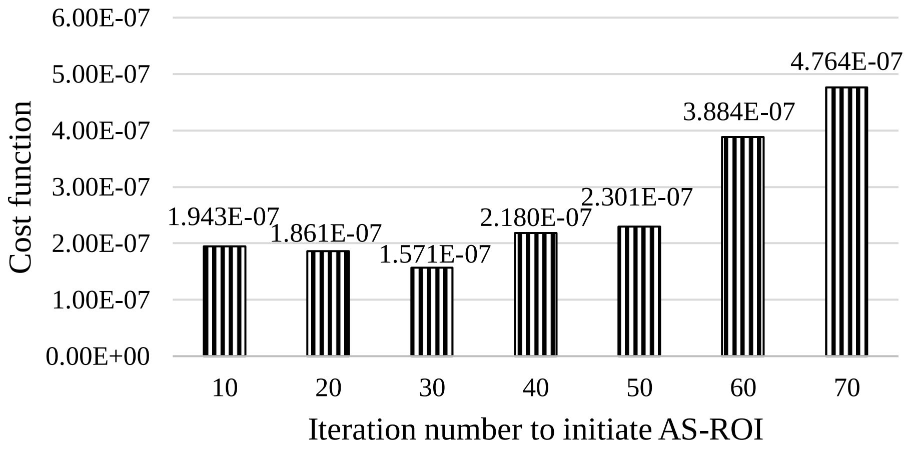

Figure 4.17: Cost functional values with varied starting number of iteration to initiate AS-ROI for object at centre coordinate

In this analysis, a circular object in two locations and 10 sizes as described in Table 4.3 is considered. Rationale of choosing circular shape in this analysis is to imitate the shape of benign tumour. Irregular shapes to indicate malignant tumour is not of interest since malignancy can be detected merely by observing the level of dielectric values. Offset values simply means distance between object and centre coordinate of FDTD (112,112). In terms of coordinate placements detection with various sizes, the accuracy is found to be 100%. Radius size is varied from 3mm to 21mm, however, there is large difference between the radius detected for all analysis and the actual. For this particular geometrical shape, the average relative error (RE) between actual and detected radius size is 55.32% for object which placed at centre coordinate. Object with offset distance of (10,10) from the centre coordinate has average RE of 68.66% in estimating object's radius.

Table 4.3: Accuracy in terms of offset and radius detected by AS-ROI for circular object in various sizes at two coordinates placement (a) offset at (0,0) from centre coordinate (b) offset at (10,10) from centre coordinate

Analysis number	Offset values detected		Actual radius of object (mm)	Detected radius (mm)	
	(a)	(b)		(a)	(b)
1	0,0	10,10	3	6	10
2	0,0	10,10	5	10	10
3	0,0	10,10	7	11	11
4	0,0	10,10	9	14	14
5	0,0	10,10	11	16	16
6	0,0	10,10	13	18	18
7	0,0	10,10	15	21	21
8	0,0	10,10	17	24	24
9	0,0	10,10	19	27	27
10	0,0	10,10	21	28	28

The analysis is extended to a U-shaped object as described in Section 4.2. Five placement coordinates are considered, with fixed value of object radius size in 24mm. In these five cases as in Table 4.4, all coordinates are determined correctly and radius detected is slightly differ with RE of 4.17%. The actual ROI is within 40mm, which then rescaled down to 25mm by AS-ROI based on the object’s radius. Number of layers detected by adaptive K-means clustering in AS-ROI also conform the actual. This imply that the geometrical shape of object influences the capability of AS-ROI as well as FBTS itself for image optimization, as the finding on radius detection is considerably different between circular and U-shaped object.

Table 4.4: Accuracy in terms of offset and radius detected by AS-ROI which initiated at 30^{th} iteration for U-shape object

Analysis number	Actual offset values	Offset values detected	Initial radius of ROI (mm)	Actual radius of object (mm)	New radius of ROI (mm)
1	0,0	0,0	40	24	25
2	10,10	10,10	40	24	25
3	5,-5	5,-5	40	24	25
4	-5,5	-5,5	40	24	25
5	-10,-10	-10,-10	40	24	25

Figure 4.18 and Figure 4.19 show the capability of AS-ROI in improving accuracy of reconstructed images for all five coordinates stated in Table 4.4. In the rescaled ROI case, note that both relative permittivity and conductivity images in mentioned figures are improved in terms of its intensities level, compared to the non-rescaled ROI by FBTS. This can be seen in the reduction of MSE values in both figures for the rescaled cases in all five coordinate settings. Average MSE of relative permittivity images by AS-ROI in FBTS is at 5.41, that is lower than the average MSE of FBTS at 6.03. As for conductivity images, the average MSE are 3.16×10^{-3} and 4.14×10^{-3} for AS-ROI and FBTS, respectively.

In the rescaling process by AS-ROI, initial pixels that exterior to the detected object shall be replaced with background pixels in which considerably lower than the object's profiles. The incident fields are therefore can easily penetrate through background layer toward the object due to low profiles' values, thus mitigate the inverse scattering process. The results is comparable to findings obtained by IMSA [11, 44–46], in which reducing the number of pixels for reconstruction had increase the accuracy of reconstructed profiles.

Hence, it supported the fact that nonlinearity of inversion solution such as FBTS is proportional to the number of pixels for reconstruction [11, 21].

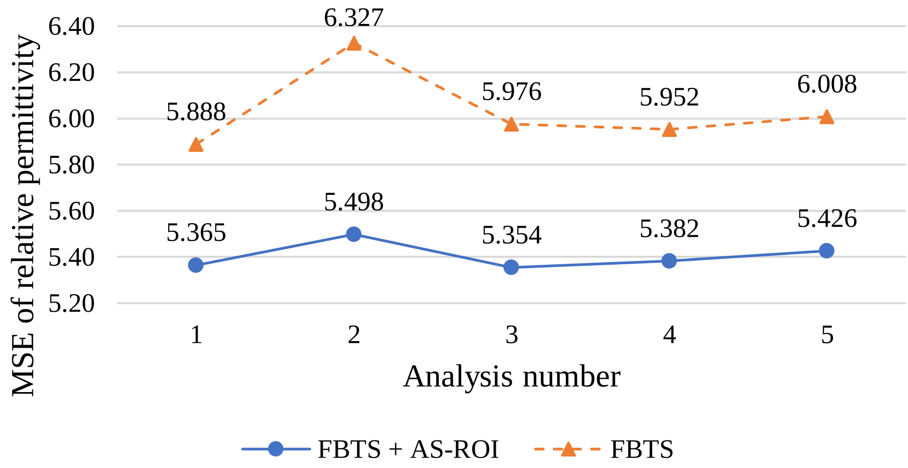

Figure 4.18: MSE values of relative permittivity images between AS-ROI and FBTS

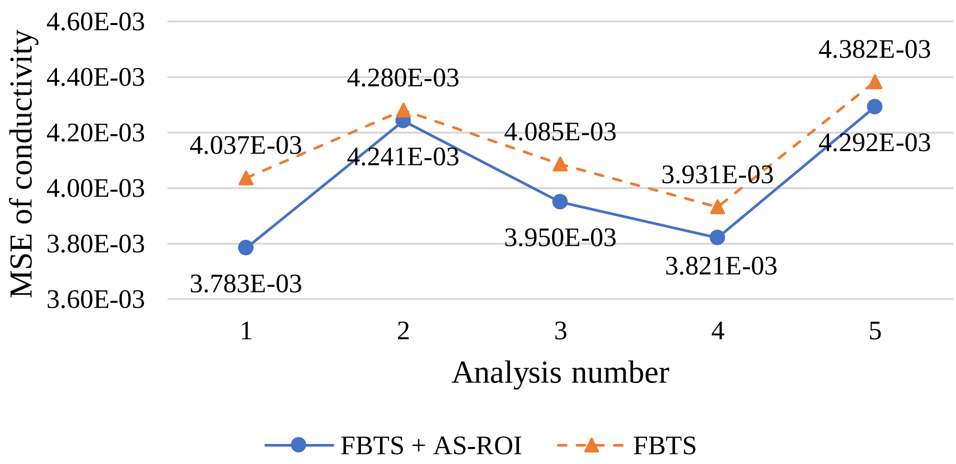

Figure 4.19: MSE values of conductivity images between AS-ROI and FBTS

4.5 AS-ROI with Edge Preserving

In previous analysis, it is proven that incorporating individual element of edge preserving techniques as well as AS-ROI into FBTS gives substantial enhancement in shape, location and intensities level of unknown object. Therefore, for this analysis, both elements are combined inside FBTS with optimal parameter settings as presented in previous sections.

Object to be analysed is a U-shaped object, similar to analysis in Section 4.2. Five coordinate settings are employed as described in Table 4.4. Rescaling process is implemented at 30th iterations and regularization started 20 iterations after redefining the new ROI area. Starting iteration number of regularization which runs synchronous to AS-ROI process are analysed. The empirical result showed that the best result can be obtained at 20th iteration after the newly ROI is defined.

Cross-sectional top view of relative permittivity images from the combined methods are illustrated in Figure 4.20. Note that the quality of the combined rescaled and regularized case in Figure 4.20(b) is far better than Figure 4.20(a). Figure 4.21 shows relative change in MSE level of relative permittivity to compare the performance of non-regularized FBTS with AS-ROI and regularized FBTS with AS-ROI. Based on quantitative measure in Figure 4.21, by combining both mentioned methods to assist the optimization solution, it further reduced the MSE level in all analysis settings. Relative change is measured with respect to accuracy by FBTS. The relative change is intentionally presented in negative values as it means decrement in MSE. As for the MSE, the lower means accuracy of sought measured values is improved. The average of relative change by AS-ROI is -0.1 or equivalent to 10.33% increment. The combined methods achieved even lower average value of relative change, which is at -0.19 or improved about 18.58%. Each method of edge preserving smoothing filter, regularization and AS-ROI has been proven able elevate the efficiency of FBTS solution, which can be referred from Section 4.2 up to 4.4. In a double fold process of the combined rescaled and regularized method in FBTS, edge preserving smoothing filter and regularization are alternately imposed on the improved reconstructed profiles by AS-ROI. Thus, it rationalizes higher precision level as indicated by lower MSE.

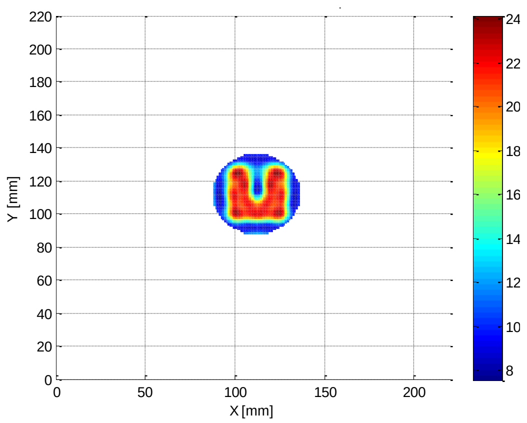

(a) AS-ROI

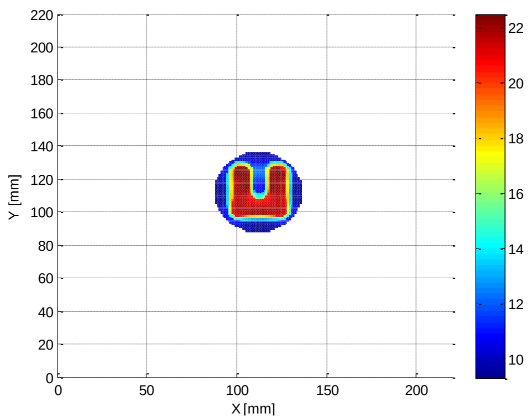

(b) AS-ROI with edge preserving techniques

Figure 4.20: Cross-sectional top view of relative permittivity images in x-y plane at 100th iteration in the new ROI between AS-ROI and AS-ROI with edge preserving techniques

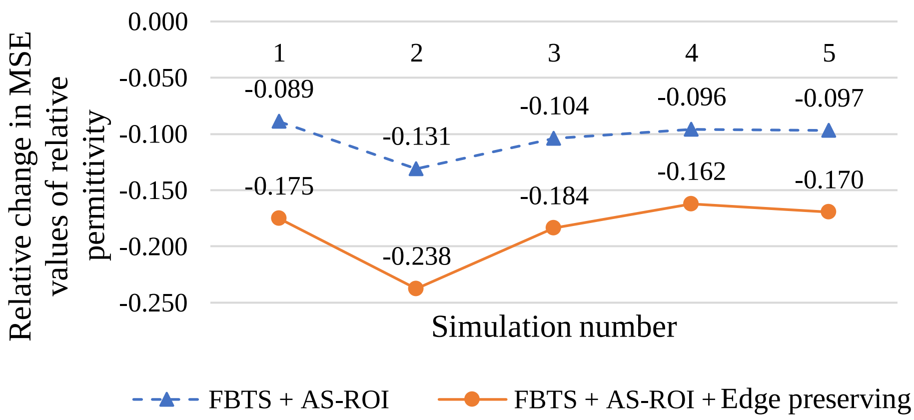

Figure 4.21: Relative change in MSE of relative permittivity with respect to FBTS values between AS-ROI and AS-ROI with edge preserving for five coordinate placements settings

Comparison of computational time taken by FBTS, rescaled FBTS by AS-ROI and regularized of rescaled FBTS is shown in Figure 4.22. Rescale down the ROI area with AS-ROI almost reduce the computational time, in which 4 out of 5 settings are completed in lesser time compared to FBTS. Average computational time for FBTS for all five cases is 30442s. Incorporating AS-ROI in FBTS only consumes 86.94% of average time required for FBTS in reconstructing all five cases, which is equivalent to 26467s due to reduction in the number of pixels. The time difference between the two approaches is about 3976s.

Integrating regularization into FBTS with AS-ROI though consumes more time to reach the convergence criterion. It requires 32228s in average, that is 5.87% more time consuming than FBTS, as more parameters and processes involved.

However, to achieve accuracy level as the combined method of FBTS, AS-ROI and regularization, FBTS and FBTS with AS-ROI might need more iterations of optimization for image reconstruction. More iterations clearly mean that computational time and memory allocation will be increased. Thus, it can be concluded that the combined method of FBTS, AS-ROI and regularization able to compensate computational cost for image reconstruction.

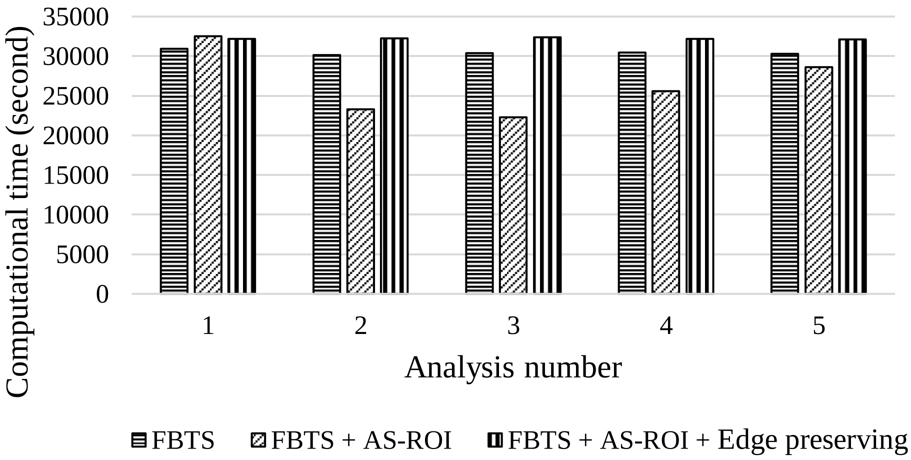

Figure 4.22: Comparison in computational time between three different approaches

4.6 Image reconstruction of lung(s) area by FBTS

In order to validate previous results with the proposed technique, the research work is extended to lungs area. Analysis in this section contribute to lung(s) image reconstruction by FBTS. Very high contrast or large size of object would increase the nonlinearity problem of inverse scattering that disrupts the scattering process [10, 21, 29]. However, limitations for the contrast values and object's size which can cause the nonlinearity problem were never analysed. Therefore, three models are studied with its dielectric properties' settings are described as in Table 4.5 up to Table 4.7.

In the first model that illustrated in Figure 4.23, thoracic wall comprising lungs and mediastinum was considered as the object. Mediastinum takes dielectric values of human heart. Other organs like thorax, blood vessels, esophagus however, are not included, which makes the dielectric properties of the object still in two layers. Due to limited memory and to reduce the nonlinearity of FBTS, object is resized down to 40% of the actual as discussed in Chapter 3.

Results for the reconstructed images of Model#1 are presented in Figure 4.24. Even that the dielectrical property values is not of interest, object's shape and location in both relative permittivity and conductivity are still not well defined. Accuracy in terms of intensity values for the first model is quite low, which attained substantially high MSE level at 172.05 and 0.19 for permittivity and conductivity, respectively. This is due to mediastinum area is considered too large that disrupts the scattered waves back to receiving antenna. Therefore, for later analysis, only the left lung will be analysed as an object instead of taking the whole thoracic area to reduce errors.

Table 4.5: Dielectric properties settings for lungs Model#1

Layer	Actual		Initial guess	
	ε_r	σ	ε_r	σ
Lungs	15.91	0.51	19.00	0.50
Mediastinum (heart)	55.80	1.91	19.00	0.50
Background (free space)	1.00	0.00	1.00	0.00

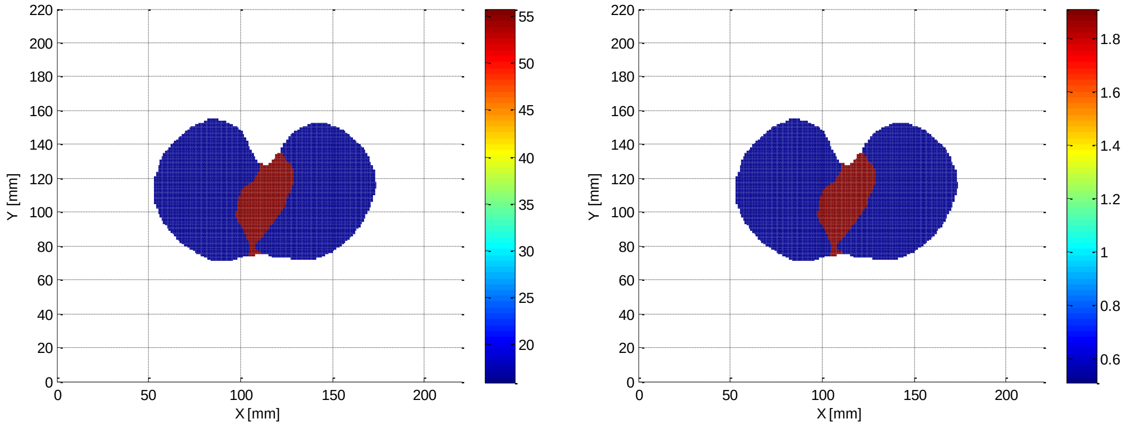

(a) Relative permittivity (b) Conductivity

Figure 4.23: Actual image of lungs Model#1

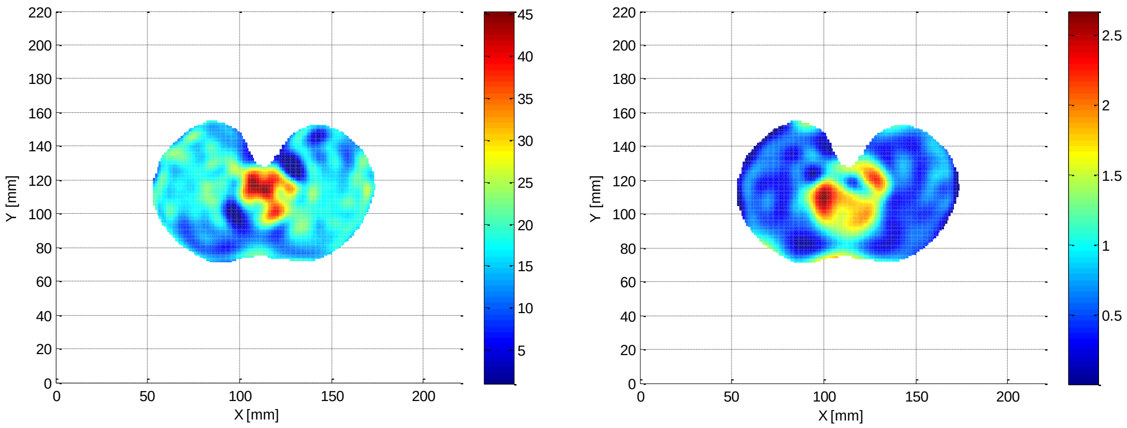

(a) Relative permittivity (b) Conductivity

Figure 4.24: Reconstructed image of lungs Model#1 by FBTS

For the second model as in Figure 4.25, only left lung area is considered to be analysed. It is rescaled to 60% from the actual image and embedded with a single circular tumour in 8mm radius. The 8mm radius is a threshold size to determine the positivity of the tumour which require additional diagnostic [153]. From the result in Figure 4.26, the tumour is quite apparent from the background. Location and shape of the tumour also resemble its original image. Permittivity's accuracy level is at 6.92 and conductivity is at 2.34×10^{-2}, which far better than the first model.

Table 4.6: Dielectric properties settings for lung Model#2

Layer	Actual		Initial guess	
	ε_r	σ	ε_r	σ
Lung	15.91	0.51	19.00	0.50
Tumour	54.68	1.84	19.0	0.50
Background (free space)	1.00	0.00	1.00	0.00

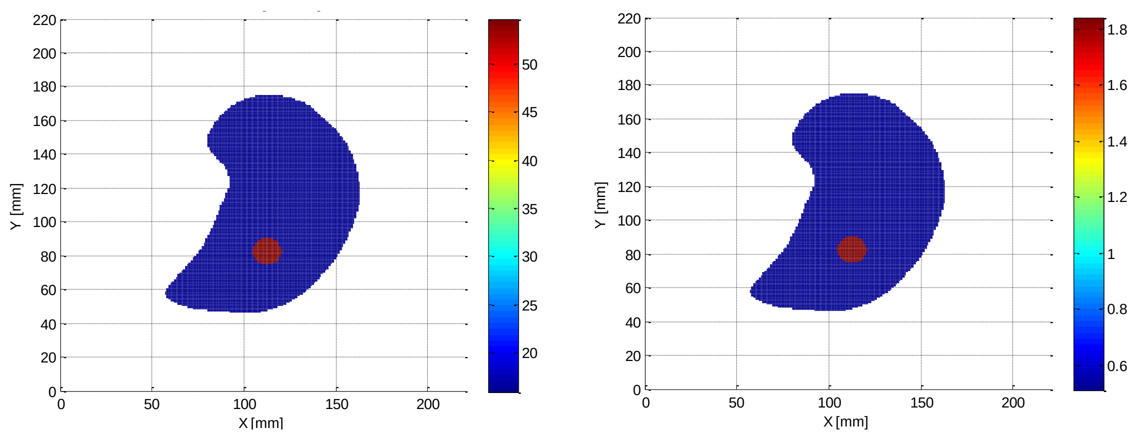

(a) Relative permittivity (b) Conductivity

Figure 4.25: Actual image of lung Model#2

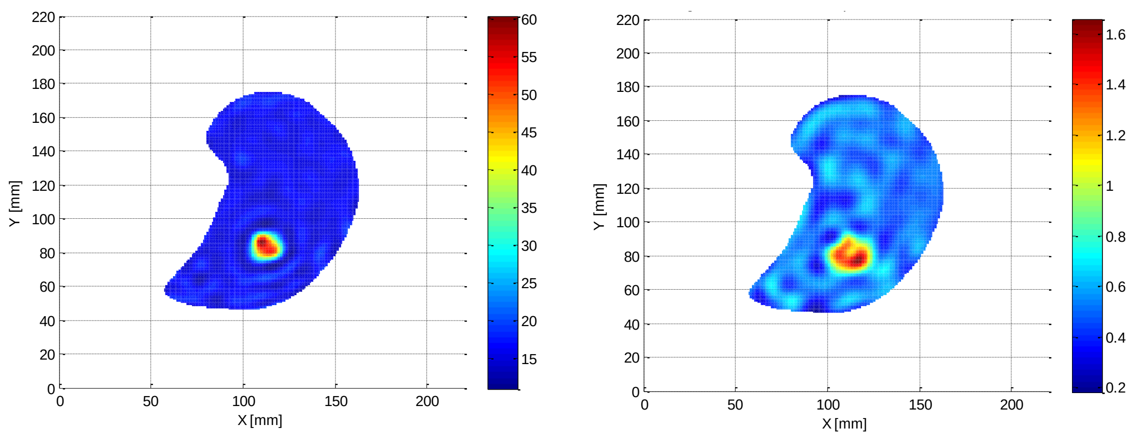

(a) Relative permittivity (b) Conductivity

Figure 4.26: Reconstructed image of lung Model#2 by FBTS

Model#3 is illustrated in Figure 4.27, which almost equivalent to Model#2 in shape and size. However, it has smaller dielectric values of tumour as given in Table 4.7. Similar to previous result for Model#2, location of the tumour also corresponds to the actual. Tumour's outline is more rounded in shape compared to Model#2. From the three lung(s) models that have been analysed, Model#3 shows the highest accuracy that achieved MSE of 1.15 for relative permittivity and 1.75×10^{-3} for conductivity. In previous models, there is large difference between dielectric property values for each layer compared to Model#3. This proves that, other than object's area, too high contrast between layers also suppress the scattering process which leads to inaccuracy in reconstructing image profiles.

Table 4.7: Dielectric properties settings for lung Model#3

Layer	Actual		Initial guess	
	ε_r	σ	ε_r	σ
Lung	15.91	0.51	18.70	0.50
Tumour	33.41	0.92	18.70	0.50
Background (free space)	1.00	0.00	1.00	0.00

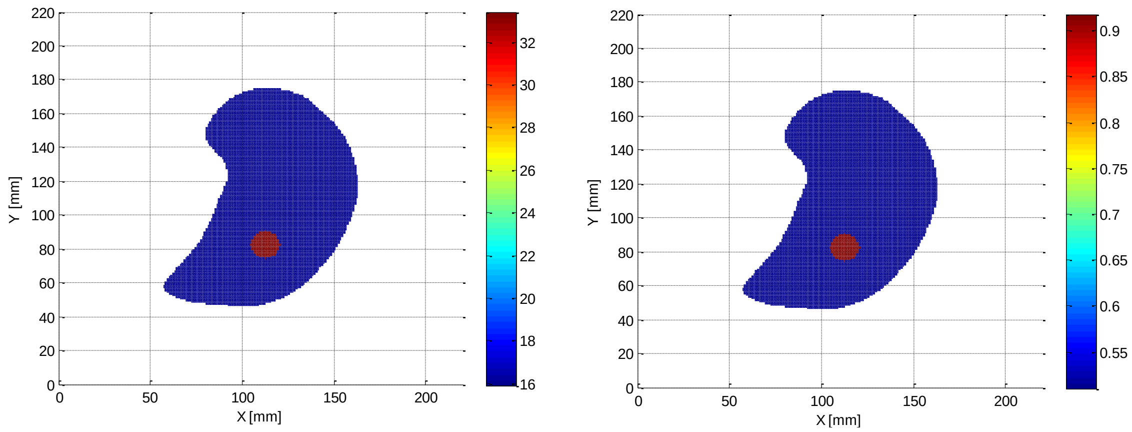

(a) Relative permittivity (b) Conductivity

Figure 4.27: Actual image of lung Model#3

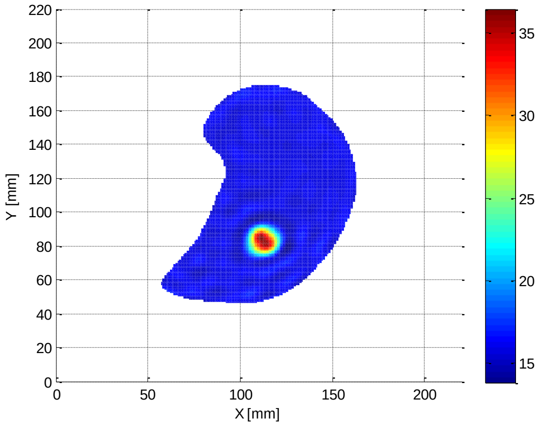

(a) Relative permittivity

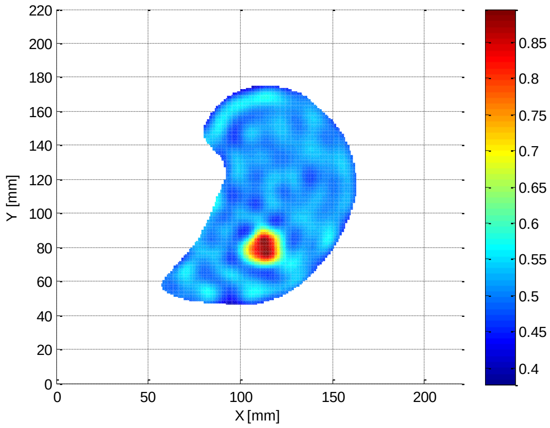

(b) Conductivity

Figure 4.28: Reconstructed image of lung Model#3 by FBTS

4.7 Application of AS-ROI and edge preserving regularization for lung(s) tumour detection

4.7.1 Single tumour detection in lung model by AS-ROI

In this section, Model#2 and Model#3 are analysed to investigate the efficiency of AS-ROI in pointing out location and size of an embedded tumour in five different coordinates. The results are shown in Table 4.8. As in Section 4.4, offset values mentioned in Table 4.8 denotes distance between the tumour and FDTD's centre point which located at coordinate (112,112). In all five settings, the algorithm accurately locates only one coordinate for Model#2 and two coordinates for Model#3. Figure 4.29 shows error of offset values which measured in Euclidean distance (ED) for both models. From the figure, it is obviously seen that Model#2 has larger error than Model#3 in terms of object location detection, with average distance of 3.91 and 0.68, respectively. It is due to accuracy level of Model#2 is considerably lower than Model#3, which discussed in Section 4.6.

As for radius approximation, the algorithm shows consistency in estimating radius for Model#3 with average error of 0.63. It is noticeably lower than average error of Model#2 which at 2.0. Average error in estimating object's radius is analogous to accuracy level measured in MSE for lung image reconstruction by FBTS. This indicates that efficiency of AS-ROI is highly relied upon the accuracy of FBTS estimation in reconstructing image profiles prior to rescaling process. AS-ROI is designed to slightly overestimate the size of the object in order to avoid missing pixels. However, providing that AS-ROI started at iteration with reconstructed image is not fully developed, the size of object could be overly estimated. As mentioned in Section 4.4, nonlinearity of inverse problem is proportional to the number of unknowns. Therefore, an overly estimated size of object would not alleviate the nonlinearity problem in which degrade the efficiency of AS-ROI.

Table 4.8: Accuracy of Model#2 and Model#3 for single tumour detection by AS-ROI

Coordinate setting	Actual offset values	Offset values detected		Initial radius of object (mm)	New radius of ROI (mm)	
		Model#2	Model#3		Model#2	Model#3
1	0,0	0,0	0,0	8	13	13
2	10,10	8,9	9,9	8	14	13
3	5,-5	-3,-13	4,-5	8	66	13
4	-5,5	-6,4	-5,5	8	14	13
5	-10,-10	-10,-9	-9,-10	8	13	13

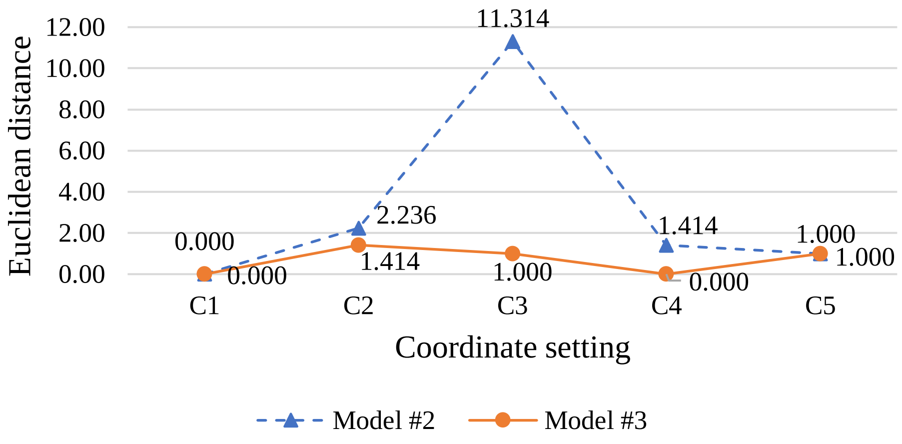

Figure 4.29: Euclidean distance with respect to centre coordinate of Model#2 and Model#3 for 5 coordinate settings of single tumour

4.7.2 Multi tumours detection in lung model by AS-ROI with edge preserving regularization

The analysis utilizes Model#3 as an object analysis due to its high accuracy of the reconstructed image profiles by FBTS. Lung area is embedded with two tumours of similar radius in 8mm, which offset at (0,0) and (25,25) from centre coordinate (112,112) as in Figure 4.30(a). Reconstructed images by three methods, FBTS, FBTS with AS-ROI and regularized FBTS with AS-ROI are illustrated in Figure 4.30(b) up to 4.30(d). Cross-sectional top view between Figure 4.30(b) and Figure 4.30(c) do not show much difference, however, Figure 4.30(c) shows slight improvement in terms of its shape due to higher signal penetration by eliminating the exterior pixels. Figure 4.30(d) is found more homogeneous in its layers compared to FBTS and rescaled FBTS by AS-ROI, as artifacts which appears as ring objects are considered vanished. Artifacts are eliminated with smoothing effect by edge preserving regularization on the solution and anisotropic diffusion filter of the reconstructed image. Therefore, non-edges area becomes more homogeneous in pixel intensities.

Cross-sectional side view of object#1 and object#2 are shown in Figure 4.31 and Figure 4.32. Note that the implementation of AS-ROI in FBTS helps the image profiles values approaching the actual object's peripheral in both Figure 4.31(a) and Figure 4.32(a). Regularizing the rescaled FBTS in Figure 4.31(b) and Figure 4.32(b) even show remarkable improvement that the regularized edges approximately overlapped with the actual edges, as the pixel values are homogenous in non-edges area which benefited from the smoothing effect.

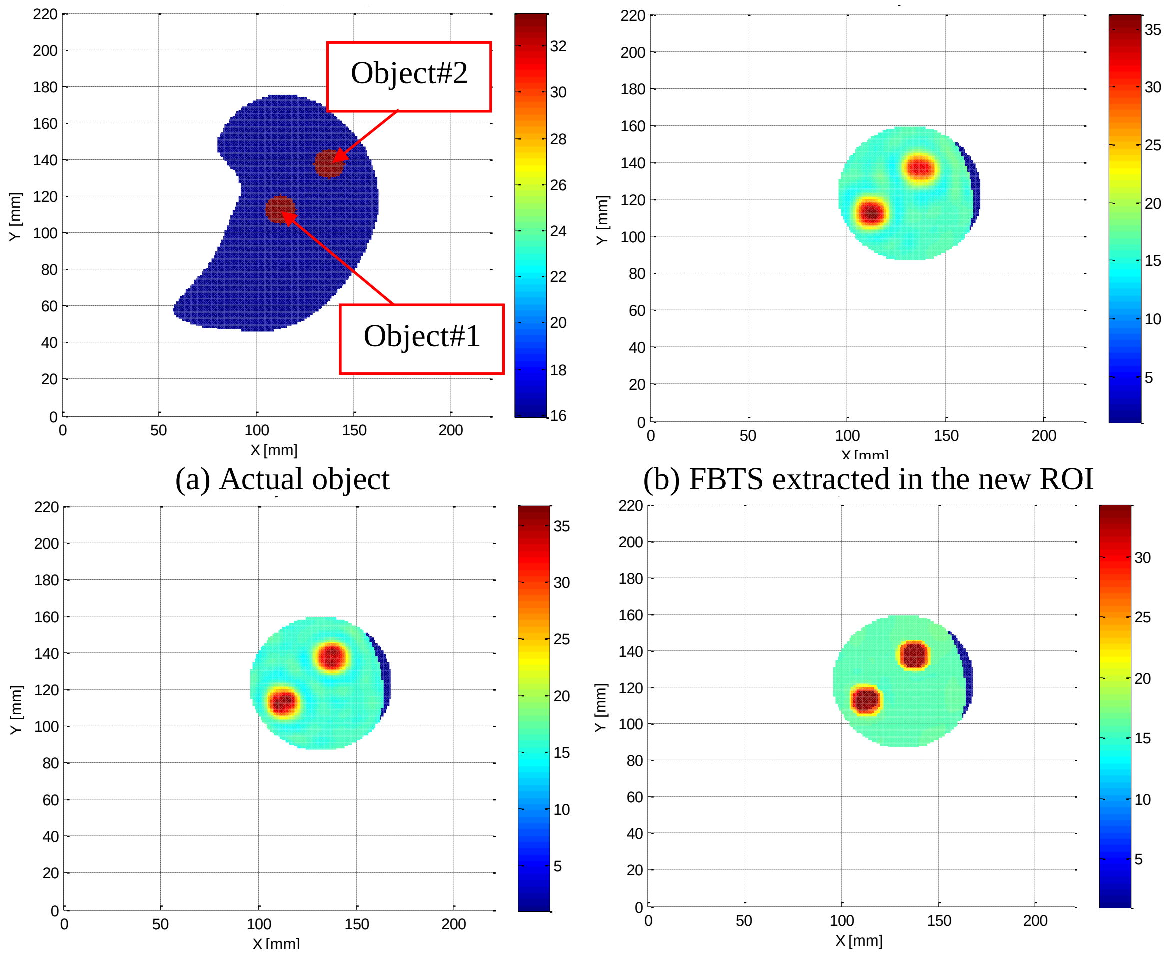

(a) Actual object

(b) FBTS extracted in the new ROI

(c) AS-ROI in FBTS

(d) AS-ROI with edge preserving techniques in FBTS

Figure 4.30: Cross-sectional of relative permittivity top view in x-y plane at 100th iteration for the segmented area

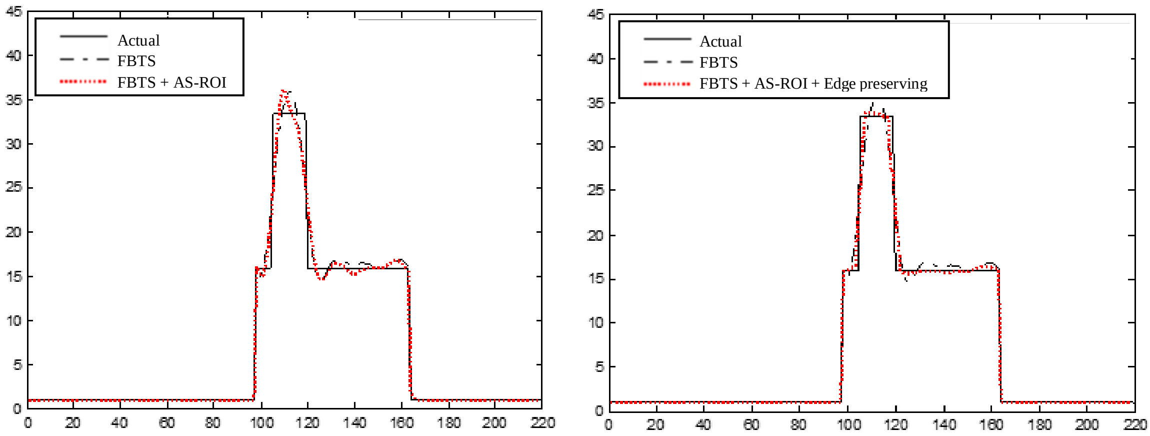

(a) AS-ROI in FBTS

(b) AS-ROI with edge preserving techniques in FBTS

Figure 4.31: Cross-sectional side view of object#1 which offset at (0,0) from centre coordinate in Model#3

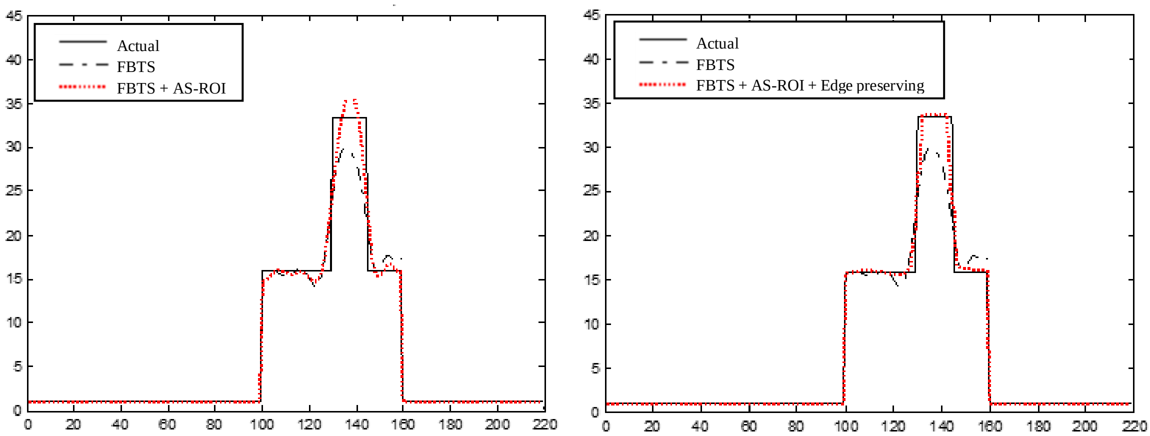

(a) AS-ROI in FBTS

(b) AS-ROI with edge preserving techniques in FBTS

Figure 4.32: Cross-sectional side view of object#2 which offset at (25,25) from centre coordinate in Model#3

Quantitative measure of accuracy level is presented in Figure 4.33. AS-ROI in FBTS elevates the accuracy about 25.17% for this particular model. The precision in image pixels or intensity levels has increased about 40.68% by integrating AS-ROI and edge preserving regularization inside FBTS compared to FBTS alone.

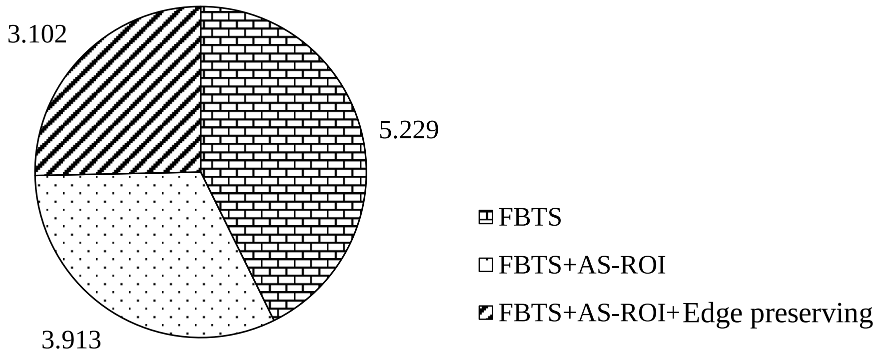

Figure 4.33: MSE of relative permittivity images of Model#3 embedded with two tumours which reconstructed by FBTS, AS-ROI in FBTS and AS-ROI with edge preserving applied in FBTS

Computational time results for three cases (FBTS, the rescaled FBTS and the regularized of rescaled FBTS) as shown in Figure 4.34 corresponds to the results presented in Figure 4.24. A left lung which embedded with two tumours is reconstructed by FBTS in 31198 seconds. The reduction of pixels by AS-ROI which only focusing on tumours area for image reconstruction has successfully reduced the computational time to 22232s or about 28.74% decrement with respect to the FBTS. The inclusion of edge preserving regularization and anisotropic diffusion filter which alternately applied on solution and relative permittivity image however has increased the time to 32662s or about 4.69% increment in comparison to the FBTS. The increment in the computational time resulted from edge preserving techniques is expected as it entailing more parameters and processes of the rescaled reconstruction area.

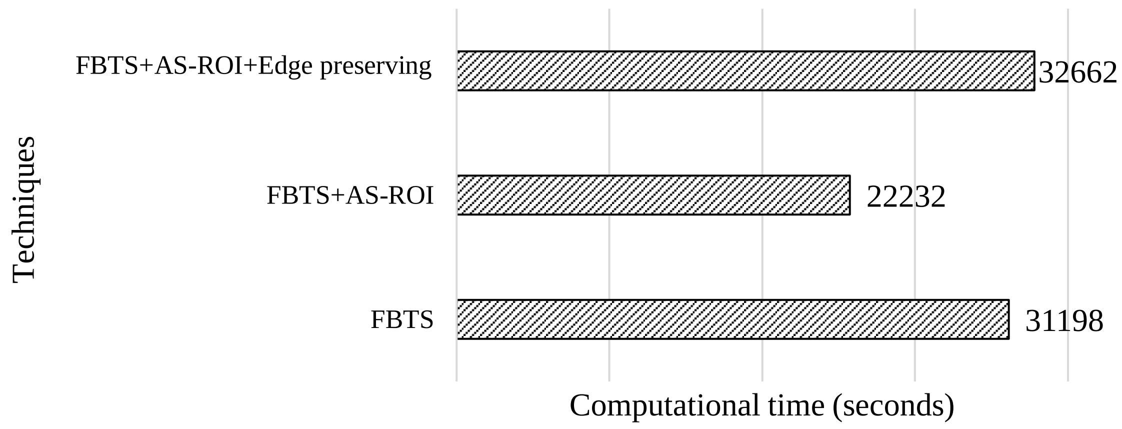

Figure 4.34: Comparison in computational time

4.8 Concluding Remarks

Based on preliminary findings, signal frequency for electromagnetic radiation was set to 2GHz and the number of utilized antennas to encircle the embedded object were maintained at 12 units throughout all simulations. Termination criterion was predetermined at 100 iterations which also based on subjective evaluation on the preliminary simulations. Analyses were categorized into two parts to study the proposed techniques in breast and lung(s) phantom model, respectively. The first part of analyses was divided into another four sections in which each section was incorporated with FBTS. It includes edge preserving smoothing filter, edge preserving regularization, AS-ROI as well as a combined method of edge preserving smoothing filter, regularization and AS-ROI. Analyses were evaluated subjectively and numerically (MSE, RE and ED as a performance metric indicator) by means of comparison between the original object, reconstructed object by FBTS and the proposed techniques. Analyses were then resumed in the second part to test the consistency of the proposed techniques with lung(s) phantom model.

In the first section of analyses from part one, anisotropic diffusion contributed the highest accuracy improvement of 13.13% in the reconstructed object of permittivity profile.

High accuracy of anisotropic diffusion is due to the smoothing effect which only significant on homogenous areas nonetheless insignificant on the detected edges. The smoothing degree imposed on pixel is evaluated pixelwise based on the occurrence of edges. Therefore, it is efficient in eliminating artifacts without removing essential structures of an image. Nevertheless, all tested filters (median filter family) have elevated the accuracy level of at least 1.6% with respect to FBTS. The application of anisotropic diffusion towards conductivity however, have worsen the reconstructed object compared to the other tested filters that increased the MSE level about 106.58% due to improper parameter settings. Adaptive weighted median filter showed the highest accuracy of the filtered conductivity with 5.41% enhancement and second highest for relative permittivity with increment of 3.64%. High performance of the adaptive weighted median filter may due to its capability in identifying corrupted pixels prior filtering process. Only selected pixels are smoothed and important structures can be preserved without being eliminated.

The second section of analyses was to test various potential functions of edge preserving regularization to eliminate artifacts in the reconstructed object. Geman & McClure potential function exhibited the highest accuracy with MSE level at 2.33 of relative permittivity and 3.63×10^{-3} of conductivity profile in 51 iterations to reconstruct the phantom model. Therefore, it was chosen to be generalized for later analyses. Ideal threshold parameter for relative permittivity was found at 1.25 and regularization coefficient attained the optimal result at 5.0×10^{-10}. Regularization coefficient which higher than 5.0×10^{-10} are too high that disrupt the FBTS solution, hence resulting higher MSE. Meanwhile coefficient which lower than 5.0×10^{-10} provide insignificant regularization effect toward the FBTS, which also resulting higher MSE values. As for the starting iteration number to initiate the regularization, it was found that ideal result was obtained under initiation at 20th iteration of the inversion technique out of 100 iterations in total.

The third section emphasize on the implementation effect of AS-ROI towards the inversion technique with relative permittivity utilized as a prior information. Analyses were carried out to detect geometrical position and size of the detected object in a circular and U-shaped pattern. As mentioned earlier, the resolution level in the rescaled reconstruction region was maintained as its original resolution. It was found that rescaling initiated at 30th iteration contribute the optimal accuracy level for image reconstruction with 100 iterations as a stopping criterion. Position placements were detected correctly for all simulations regardless of its shapes. Average RE of radius estimation for circular shape of varied sizes at offset distance (0,0) and (10,10) were 55.32% and 68.66%, respectively. Average RE of radius estimation for a U-shape pattern at fixed size and varied offset was only 4.17%. Intensity values for relative permittivity was significantly improved which reached an average enhancement of 10.33% and conductivity profile only elevated about 3.07% in average. The finding is comparable to the implementation of edge preserving smoothing filter towards the reconstructed image in which the filtering effect is less pronounced for conductivity images than relative permittivity. As discussed in Section 4.1, reconstructed conductivity profiles are less accurate than relative permittivity, which similar to findings in [54]. This could be the major cause of trivial effect of filtering and AS-ROI towards conductivity images.

The last section in the first part was to analyse the combined method of AS-ROI and edge preserving in FBTS. Empirical results showed that regularization should be initiated 20 iterations after the new reconstruction region was defined. Improvement in accuracy was indicated by relative change of MSE in negative number, in which the lower relative change signifies better result. The regularized AS-ROI in FBTS attained -0.19 in average of relative change. The non-regularized AS-ROI in FBTS only reached a relative change of -0.11 in average. In related to computational time analyses, the rescaling process by AS-ROI in FBTS had reduce the computational time about 13.06%. Implementation of regularization into AS-ROI in FBTS however, increased the computational time about 5.87%.

In the first section of the second part, three lung(s) phantom models with difference object sizes and profiles contrast were analysed with an inversion technique FBTS. Model#1 had the highest contrast profiles compared to the other two tested models consisting of 8087 image pixels. Contrast difference was computed by relative change between layer 1 (lung(s)) and layer 2 (mediastinum or tumour) with layer 2 as a reference. Accuracy indicated by MSE for Model#1 were 172.05 for relative permittivity (71.49% contrast difference) and 0.19 for conductivity profile (73.3% contrast difference). Model#2 which constitutes of 9135 pixels attained the accuracy level of 6.92 and 2.34×10^{-2} for relative permittivity (70.9% contrast difference) and conductivity (72.28% contrast difference), respectively. Model#3 had the same dimension as Model#2 exhibited even better accuracy at 1.15 for relative permittivity (52.38% contrast difference) and 1.75×10^{-3} for conductivity (44.57% contrast difference). Condition for the minimal distance between antenna and object has been violated for all three lung(s) phantom models that has been tested. It is due to reactive coupling effect is not observable for the synthetic analysis.

In the second section of part two, object (single tumour) with radius of 8mm was localized by using combined method of AS-ROI and FBTS in which the accuracy in localization was indicated by ED calculated between the original and the reconstructed object placements. Average distance for the embedded tumour in Model#2 at five coordinate placement settings was 3.91. Object in Model#3 had an average distance of 0.68 with respect to its actual coordinate. Average error of radius estimation for the embedded tumour in Model#2 and Model#3 were 2.0 and 0.63, respectively.

Multi objects (two tumours) of similar radius 8mm separated in 35.36 ED embedded in lung phantom Model#3 were analysed by FBTS, AS-ROI in FBTS along with the regularized AS-ROI in FBTS. The results showed substantial improvements in the regularized AS-ROI in FBTS which subjectively evaluated from top and side cross-sectional views. It was numerically proven by MSE in which the accuracy by FBTS was 5.23, AS-ROI in FBTS attained 3.91 and the regularized AS-ROI in FBTS reached the lowest level at 3.1. Improvement in the accuracy level provided by AS-ROI in FBTS was 25.17% and the regularized AS-ROI in FBTS successfully increased to 40.68%.

CHAPTER 5

SUMMARY, CONCLUSIONS & RECOMMENDATIONS

The aim of this research work is to reconstruct an unknown object within its detected peripheral region in high accuracy with similar resolution degree throughout the reconstruction process. Essentially it is accomplished by combining a deterministic inversion technique of Forward-Backward Time-Stepping (FBTS) with an Automated Scaling Region of Interest (AS-ROI) and edge preserving techniques. Main motivation of this research work is the nonlinearity problem of the FBTS in which volatile to changes or error in the solution. In addition to that, the research is also inspired by the computational cost which particularly expensive on condition that FBTS is combined with additional tools to mitigate the nonlinearity problem. This chapter shall conclude all findings from this research work accordingly to the prespecified objectives in achieving the research aim. Suggestions based on limitations of this research work are also discussed for future works.

5.1 Conclusions

In order to achieve the research aim, the first objective is to formulate a method which can zoom into object's region for reconstruction providing that geometrical of the object has been estimated from FBTS algorithm. This method namely as AS-ROI is functional to rescale the reconstruction region in order to reduce the nonlinearity problem and compensate the computational cost. Conclusion for the first objective can be drawn from analyses from Section 4.4 up to 4.7.2. AS-ROI relied on correct estimation of reconstructed profiles for segmentation purpose. Therefore, the initiation of AS-ROI should be carried out at certain iteration number at which the reconstruction profiles have sufficient details on the sought object. Optimal iteration number is found at 30th iteration from 100 iterations of convergence criterion. It is based on observations on MSE values and cost functional graph of various iteration number to instigate the AS-ROI, which can be referred in Section 4.4. Apart from that, the segmentation process in AS-ROI only utilizes relative permittivity due to its accuracy is higher than conductivity images.

Accuracy in object localization by AS-ROI in Section 4.4 is 100% for all tested objects in two type of shapes (circular and U-shaped object), in various sizes and at various locations. However, there is large difference in size estimation between circular and U-shaped object. For the circular shape, the average relative error (RE) between actual and detected radius size is 55.32% for object which placed at centre coordinate and 68.66% for object with offset distance of (10,10) from the centre coordinate. Meanwhile the U-shape object only attains RE of 4.17% in size estimation. Noteworthy difference in size estimation for varied shapes by AS-ROI may due to the incorrect pixels' values at the boundary of an object. Segmentation process in AS-ROI only relies on four pixels; uppermost, lowermost, rightmost and leftmost pixels. For a circular shape, only a few pixels are available in the respective directions. On condition that these pixels of a circular shape are incorrectly estimated during reconstruction, rationally it will be misclassified to incorrect cluster layer. Internal pixels of object could be misinterpreted as the background layer. Consequently, it lowers the accuracy of size estimation for a circular shape object. As for the U-shaped object analysed in this research, each side constituted of 33 connected pixels. Therefore, it lowers down the error in approximating the size supposing that several pixels in each side are incorrectly estimated.

In terms of mitigating the nonlinearity problem in FBTS, the rescaling process by AS-ROI has exhibited higher accuracy in the profiles' intensities than the FBTS. It can be observed in the reduction of MSE values for both relative permittivity and conductivity profile as well as based on subjective evaluations on the reconstructed images. It is due to better fields penetration as exterior pixels are replaced with background layer which are low in its intensities. The findings on the implementation of AS-ROI have shown great agreement with IMSA [11, 44–46]. The reduction in the number of pixels for reconstruction has successfully increase the precision level of pixels' intensity. However, rescaling in multiple stages by IMSA in FBTS has increased the cost functional and total reconstruction error at the third stage of rescaling process [11]. The increment in cost functional and total reconstruction error in [11] indicates that changing the investigation area multiple times has disrupts the solution of the FBTS. AS-ROI on the other hand has exhibited consistency in improving the accuracy of image profiles in all analyses, which can be referred from Section 4.4 up to Section 4.7.2.

It has been mentioned earlier that the research is also inspired by high computational cost which resulting from combining FBTS with additional tools to alleviate the effect of nonlinearity. Comparison of computational time taken by FBTS, rescaled FBTS by AS-ROI and regularized of rescaled FBTS has been discussed in Section 4.5 and Section 4.7.2. As anticipated, the reduction of pixels to be reconstructed by AS-ROI has reduced the computational time significantly. In Section 4.5, the combined AS-ROI with FBTS only consumes 86.94% of average time required for the FBTS. Reduction in the computational time is equivalent to 13.06%. Meanwhile in Section 4.7.2, AS-ROI reduces the computational time about 28.74% with respect to the FBTS. The inclusion of edge preserving techniques into the combined AS-ROI with FBTS however has slightly increase the computational time. In Section 4.5, it is 5.87% more time consuming than FBTS. The same outcome also can be seen in Section 4.7.2, in which shows 4.69% time increment in comparison to the FBTS. The increment in the computational time is due to more parameters and processes imposed towards the rescaled reconstruction area. Nevertheless, the combined method of FBTS, AS-ROI and edge preserving techniques compensates the computational cost for image reconstruction for achieving higher accuracy of image profiles.

The second objective of this research is to evaluate the combined algorithm of the FBTS, AS-ROI and edge preserving techniques in minimizing relative change of mean squared error (MSE) between dielectric properties in actual and reconstructed object. From discussion in Section 4.3, edge preserving regularization does not necessarily imposed on all profiles available. In contrast to common practise as applied in [13, 18, 29, 50], edge preserving regularization in this research work is only applied towards relative permittivity. It is proven that unregularized conductivity would not affect the regularized relative permittivity in its precision level. Plus, it would reduce the complexity in determine regularization parameter settings.

Edge preserving filter and regularization method are alternately applied into a combined method of FBTS and AS-ROI to elevate the precision of the reconstructed object. In Section 4.5, analyses were carried out on phantom model which based on breast dielectric profiles. Accuracy of the reconstructed dielectric profiles is further increased with the implementation of edge preserving techniques. The increment in accuracy is shown in the decrement of relative change. From results in Section 4.5, the average of relative change by AS-ROI in relative to FBTS is -0.1. The edge preserving techniques contribute even lower average value of relative change, which is at -0.19. The improvement is consistent to findings of lung phantom model presented in Section 4.7.2. The decrement in relative change by AS-ROI is -0.25 in comparison to edge preserving technique in the combined AS-ROI with FBTS has attained relative change of -0.41.

Meanwhile the third objective is to validate the consistency of the combined algorithm of the FBTS, AS-ROI and edge preserving techniques in improving the accuracy of reconstructed object with respect to the actual in lung(s) model. Results in Section 4.7.1 (lung phantom model) is analogous to findings discussed in Section 4.4 (breast phantom model). AS-ROI successfully extracts the tumour from the background layer, in which the initial lung(s) area is rescaled down to tumour's size and location. Localization of tumour in lung phantom model in 4.7.1 and 4.7.2 is slightly inaccurate in comparison to object localization in Section 4.4, which due to difference in precision level of the reconstructed lung and breast phantom model by FBTS.

Object in Model#3 discussed in Section 4.7.1 is better localized in which average Euclidean distance (ED) of Model#3 is considerably lower than Model#2. Average error of radius estimation for Model#3 also significantly lower than Model#2 as the efficiency of AS-ROI relies on correct estimation by FBTS. Due to high accuracy of Model#3, it is utilized to be tested with regularized AS-ROI and FBTS in Section 4.7.2. Results in cross-sectional top and side views showed that artifacts which appear as ring objects in the results obtained by FBTS and the combined AS-ROI with FBTS were successfully eliminated by the alternate integration of edge preserving smoothing filter and regularization into the combined AS-ROI and FBTS. The regularized AS-ROI with FBTS attained the highest accuracy level in pixel intensities (40.68% increment in relative to FBTS) compared to the combined AS-ROI and FBTS (25.17% increment with respect to FBTS). The decrement of MSE values in lung phantom model by AS-ROI and regularized AS-ROI in FBTS are comparable to findings obtained in analyses from Section 4.5.

It can be concluded that all three prespecified objectives for this research work have been successfully realized. The formulated AS-ROI effectively pointing out object's geometry in ROI. Nonlinearity problem assessed by profiles' precision level and computational cost are significantly reduced with rescaling process by AS-ROI. Each method of edge preserving smoothing filter, edge preserving smoothing regularization and AS-ROI has been proven can elevate the precision of profiles intensity reconstructed by the FBTS. The combined method of the three mentioned techniques in FBTS showed even better outcomes which lowering the relative change of MSE. Additionally, the combined method of FBTS, AS-ROI and edge preserving techniques have shown consistency in results for both breast and lung(s) model.

5.2 Recommendations for future works

FBTS is a deterministic inversion technique which needs proper estimation of initial guess to guide the solution. An effective and reliable inversion technique to detect an unknown embedded object should be equipped with a solution that capable to solve the inverse problem globally rather than locally converge. This would eliminate the needs of proper initial guess which supposedly unavailable and unknown. Therefore, it is highly recommended that the deterministic inversion technique FBTS should be integrated with any stochastic solution for example Particle Swarm Optimization (PSO) and Differential Evolution (DE), particularly in its early iterations.

The results shown high dependency of AS-ROI technique upon the efficacy of FBTS in estimating the reconstructed object profiles to point out object location correctly. Similar to the recommendation in regards to implement stochastic optimization into the FBTS inversion solution for future work, AS-ROI too should be integrated with stochastic search approach in its segmentation algorithm. Inaccurate patterns could be adjusted since global solution is robust to outliers that can risk the selection of cluster centroids in segmenting profiles layers. This can reduce the dependency on the inversion technique as a prior knowledge and thus AS-ROI can be initiated at any iteration number of FBTS.

Limitation of AS-ROI is delimiting the reconstruction area to object’s size with the exterior pixels are replaced with free space profiles values. This is analogous to the concept of Iterative Multi Scaling Approach (IMSA) as discussed in Chapter 2. However, this approach may contradict to real life imaging scenario in which the bombarded signals still have to penetrate the exterior layers or substances that encircled the sought object to search. This issue can be tackled in future work by adapting the concept of Discrete Algebraic Reconstruction Technique (DART) in which the exterior pixels can be regulated with threshold values [116].

Present research work only concerning the implementation of the proposed works in noise-free environment which merely focusing on tackling intrinsic issues of inverse problem. All parameters involved in the research works were determined by empirical analyses which is a formidable task to obtain optimal values. Based on review of related literatures in denoising purpose, most effective techniques require the algorithm being adaptive to local features or noise sensitivity level. It is anticipated that the algorithm of regularized AS-ROI in FBTS can be upgraded in future works that its optimal parameters can be automatically determined from noiseless and noisy spatial information.

Accuracy in distinguish contaminated pixels in an image or signal can provide substantial improvement in the denoising process. Corrupted pixels have to be identified prior smoothing, regularization as well as segmentation in order for these processes only implemented towards the selected noisy area. Thus, not only it would alleviate the computational process nevertheless this technique able to avoid missing information particularly at the edges. Successful in determining these corrupted pixels would make the overall system robust to ill-posed and nonlinearity of inverse problem as well as against the added noise in effort to preserve important features during denoising.

Edge detection plays vital role in image filtering and regularization to ensure image structures are retained in eliminating noise or artifacts. It would be ideal analyses on condition that several edge operators are employed and tested against varied conditions. It is also intriguing to know the effect of introducing non-local features from neighbourhood patches as a priori knowledge into the combined method of edge preserving filter and regularization. The concept which taken from Non-Local Means filtering has been adapted in many research studies that exhibited promising outcomes.

Accuracy of the reconstructed profiles in this research is only validated by using MSE index which taking an average of squared error for the whole profile image. It is recommended to compute the accuracy at the vicinity to improve the reliability of precision evaluation particularly in edge detection analyses. Other image quality metrics should also be considered in future works which not only able to assess the accuracy in terms of image pixels nevertheless the quality in image structure as well.

Time-effective is among efficiency measure of an inversion system. Parallel computing is often suggested to reduce significant amount of time and memory efficiently in computational process. However, it is even better to revise the whole optimization algorithm of regularized AS-ROI into fast algorithm. Incorporating parallel with fast algorithm of regularized AS-ROI surely will elevates the time efficiency in achieving convergence criterion. Integrate a stochastic search optimization into both FBTS and AS-ROI is also one factor that can improve computational cost as the solution is searched in several points in single iteration. On top of that, stochastic implementation would reduce the probability of facing false solution in inversion technique as well as in segmentation.

REFERENCES

[1] Johnson, J. E., Takenaka, T., Ping, K. A. H., Honda, S., & Tanaka, T. (2009). Advances in the 3-D forward–backward time-stepping (FBTS) inverse scattering technique for breast cancer detection. *IEEE Transactions on Biomedical Engineering*, *56*(9), 2232-2243.

[2] Scapaticci, R., Bucci, O. M., Catapano, I., & Crocco, L. (2014). Differential microwave imaging for brain stroke followup. *International Journal of Antennas and Propagation*, *2014,* 1-11.

[3] Moriyama, T., Salucci, M., Oliveri, G., Tenuti, L., Rocca, P., & Massa, A. (2014). Multi-scaling deterministic imaging for GPR survey. In *Antenna Measurements & Applications, 2014 IEEE Conference on* (pp. 1-3). IEEE.

[4] Salucci, M., Tenuti, L., Poli, L., & Massa, A. (2017). Buried object detection and imaging through innovative processing of GPR data. In *Antennas and Propagation, 2017 11th European Conference on* (pp. 1703-1706). IEEE.

[5] Catapano, I., Affinito, A., Gennarelli, G., di Maio, F., Loperte, A., & Soldovieri, F. (2014). Full three-dimensional imaging via ground penetrating radar: Assessment in controlled conditions and on field for archaeological prospecting. *Applied Physics A*, *115*(4), 1415-1422.

[6] Lai, J., Li, M., Li, P., & Li, W. (2017). A fast direct imaging method for the inverse obstacle scattering problem with nonlinear point scatterers. *arXiv preprint arXiv:1706.06949*.

[7] Hu, G., Salo, M., & Vesalainen, E. V. (2016). Shape identification in inverse medium scattering problems with a single far-field pattern. *SIAM Journal on Mathematical Analysis*, *48*(1), 152-165.

[8] Li, P. A. N. (2011). *Electromagnetic inverse scattering problems* (Doctoral dissertation). Zhejiang University.

[9] Aramini, R. (2011). *Computational inverse scattering via qualitative methods* (Doctoral

dissertation). University of Trento.

[10] Tanaka, T., Kuroki, N., & Takenaka, T. (2003). Filtered forward-backward time-stepping method applied to reconstruction of dielectric cylinders. *Journal of Electromagnetic Waves and Applications*, *17*(2), 253-270.

[11] Moriyama, T., Oliveri, G., Salucci, M., & Takenaka, T. (2014). A multi-scaling forward-backward time-stepping method for microwave imaging. *IEICE Electronics Express*, *11*(16), 1-12.

[12] Rocca, P., Benedetti, M., Donelli, M., Franceschini, D., & Massa, A. (2009). Evolutionary optimization as applied to inverse scattering problems. *Inverse Problems*, *25*(12), 1-61.

[13] Belkebir, K., Baussard, A., & Premel, D. (2005). Edge-preserving regularization scheme applied to modified gradient method to reconstruct two-dimensional targets from data laboratory-controlled. *Progress in Electromagnetics Research*, *54*, 1-17.

[14] Zakaria, A., Gilmore, C., & LoVetri, J. (2010). Finite-element contrast source inversion method for microwave imaging. *Inverse Problems*, *26*(11), 1-21.

[15] Chen, X., Xu, K., Shen, F., Ran, L., & Zhong, Y. (2015). Subspace-based optimization method coupled with multiplicative regularization for edge-preserving inversion. In *Antennas and Propagation & USNC/URSI National Radio Science Meeting, 2015 IEEE International Symposium on* (pp. 898-899). IEEE.

[16] Ye, X., Poli, L., Oliveri, G., Zhong, Y., Agarwal, K., Massa, A., & Chen, X. (2015). Multi-resolution subspace-based optimization method for solving three-dimensional inverse scattering problems. *Journal of the Optical Society of America A, 32*(11), 2218-2226.

[17] Zhong, Y., Lambert, M., Lesselier, D., & Chen, X. (2016). A new integral equation method to solve highly nonlinear inverse scattering problems. *IEEE Transactions on Antennas and Propagation*, *64*(5), 1788-1799.

[18] Yong, G., Ping, K. A. H., Sahrani, S., Marhaban, M. H., Saripan, M. I., Moriyama, T., & Takenaka, T. (2017). Profile Reconstruction Utilizing Forward-Backward Time-Stepping with the Integration of Automated Edge-Preserving Regularization Technique for Object

Detection Applications. *Progress in Electromagnetics Research*, *54*, 125-135.

[19] Ng, S. W., Ping, K. A. H., Sahrani, S., Marhaban, M. H., Saripan, M. I., Moriyama, T., & Takenaka, T. (2016). Preliminary results on estimation of the dispersive dielectric properties of an object utilizing frequency-dependent forward-backward time-stepping technique. *Progress in Electromagnetics Research*, *49*, 61-68.

[20] Rekanos, I. T., Yioultsis, T. V., & Tsiboukis, T. D. (1999). Inverse scattering using the finite-element method and a nonlinear optimization technique. *IEEE Transactions on Microwave Theory and Techniques*, *47*(3), 336-344.

[21] Moriyama, T., & Takenaka, T. (2015). Filtered forward-backward time-stepping method without information on incident field. In *Microwave Symposium, 2015 IEEE 15th Mediterranean* (pp. 1-4). IEEE.

[22] Pastorino, M. (2007). Stochastic optimization methods applied to microwave imaging: A review. *IEEE Transactions on Antennas and Propagation*, *55*(3), 538-548.

[23] Garcia-Fernandez, M., Garcia, C., Alvarez, Y., & Las-Heras, F. (2015). Influence of contour smoothness and electric size on the profile reconstruction of metallic objects using hybrid optimization. In *EUROCON 2015-International Conference on Computer as a Tool, IEEE* (pp. 1-6). IEEE.

[24] Moriyama, T., Salucci, M., Tanaka, T., & Takenaka, T. (2016). Image reconstruction from total electric field data with no information on incident field. *Journal of Electromagnetic Waves and Applications*, *30*(9), 1162-1170.

[25] Rekanos, I. T. (2008). Shape reconstruction of a perfectly conducting scatterer using differential evolution and particle swarm optimization. *IEEE Transactions on Geoscience and Remote Sensing*, *46*(7), 1967-1974.

[26] Donelli, M., Franceschini, G., Martini, A., & Massa, A. (2006). An integrated multiscaling strategy based on a particle swarm algorithm for inverse scattering problems. *IEEE Transactions on Geoscience and Remote Sensing*, *44*(2), 298-312.

[27] Karaboga, N. (2005). Digital IIR filter design using differential evolution

algorithm. *EURASIP Journal on Applied Signal Processing*, *2005*, 1269-1276.

[28] Takenaka, T., Tanaka, T., Harada, H., & He, S. (1997). FDTD approach to time-domain inverse scattering problem for stratified lossy media. *Microwave and Optical Technology Letters*, *16*(5), 292-296.

[29] Takenaka, T., Jia, H., & Tanaka, T. (2000). Microwave imaging of electrical property distributions by a forward-backward time-stepping method. *Journal of Electromagnetic Waves and Applications*, *14*(12), 1609-1626.

[30] Sun, J., Zhang, Q., & Tsang, E. P. (2005). DE/EDA: A new evolutionary algorithm for global optimization. *Information Sciences*, *169*(3-4), 249-262.

[31] Gürbüz, T. U., Aslanyürek, B., Yapar, A., Şahintürk, H., & Akduman, I. (2014). A nonlinear microwave breast cancer imaging approach through realistic body–breast modeling. *IEEE Transactions on Antennas and Propagation*, *62*(5), 2596-2605.

[32] Scapaticci, R., Di Donato, L., Catapano, I., & Crocco, L. (2012). A feasibility study on microwave imaging for brain stroke monitoring. *Progress in Electromagnetics Research*, *40*, 305-324.

[33] Bao, G., Li, P., Lin, J., & Triki, F. (2015). Inverse scattering problems with multi-frequencies. *Inverse Problems*, *31*(9), 1-21.

[34] Russell Luke, D., & Potthast, R. (2006). The point source method for inverse scattering in the time domain. *Mathematical Methods in The Applied Sciences*, *29*(13), 1501-1521.

[35] Elizabeth, M. A, Ping, K. A. H., Wei, N. S., Wan Zainal Abidin, W. A., Masri, T., Othman, A. K., Moriyama, T., & Takenaka, T. (2012). 2-D reconstruction of breast image using Forward-Backward Time-Stepping method for breast tumour detection. In *Applied Electromagnetics, 2012 IEEE Asia-Pacific Conference on* (pp. 70-73). IEEE.

[36] Zhou, H., & Zhang, H. J. (2011). Increasing the efficiency of forward–backward time-stepping reconstruction method. In *Proceedings of Progress in Electromagnetics Research Symposium* (pp. 878-881).

[37] Takenaka, T., Moriyama, T., Ping, K. A. H., & Yamasaki, T. (2010). Microwave breast

imaging by the filtered forward-backward time-stepping method. In *Electromagnetic Theory, 2010 URSI International Symposium on* (pp. 946-949). IEEE.

[38] Ibrahim, P. M., Ping, K. A. H., Wei, N. S., Guang, Y., Rajaee, N., & Anyi, M. (2016). Elliptic filter and iterative inversion method for buried object detection applications. *Applied Mechanics and Materials*, *833*, 164–169.

[39] Jamali, N. H., Ping, K. A. H., Sahrani, S., Mat, D. A. A., Marhaban, M. H., Saripan, M. I., & Takenaka, T. (2017). Image reconstruction based on combination of inverse scattering technique and total variation regularization method. *Indonesian Journal of Electrical Engineering and Computer Science*, *5*(3), 569-576.

[40] Chie, A. S. C., Ping, K. A. H., Guang, Y., Wei, N. S., & Rajaee, N. (2016). Preliminary results of integrating Tikhonov's regularization in Forward-Backward Time-Stepping technique for object detection. *Applied Mechanics and Materials*, *833*, 170-175.

[41] Ping, K. A. H., Moriyama, T., Takenaka, T., & Tanaka, T. (2009). Two-dimensional Forward-Backward Time-Stepping approach for tumor detection in dispersive breast tissues. In *2009 Mediterrannean Microwave Symposium* (pp. 1-4). IEEE.

[42] Moriyama, T., & Takenaka, T. (2015). Inverse scattering approach with measurement of only total electric field. *Microwave and Optical Technology Letters*, *57*(1), 137-141.

[43] Moriyama, T., Oliveri, G., Massa, A., & Takenaka, T. (2011). Iterative multiscaling strategy incorporated into time domain inverse scattering method for cross-borehole imaging. In *Geoscience and Remote Sensing Symposium, 2011 IEEE International* (pp. 846-849). IEEE.

[44] Caorsi, S., Donelli, M., Franceschini, D., & Massa, A. (2002). An iterative multiresolution approach for microwave imaging applications. *Microwave and Optical Technology Letters*, *32*(5), 352-356.

[45] Caorsi, S., Donelli, M., Franceschini, D., & Massa, A. (2003). A new methodology based on an iterative multiscaling for microwave imaging. *IEEE Transactions on Microwave Theory and Techniques*, *51*(4), 1162-1173.

[46] Caorsi, S., Donelli, M., & Massa, A. (2004). Detection, location, and imaging of multiple scatterers by means of the iterative multiscaling method. *IEEE Transactions on Microwave Theory and Techniques*, *52*(4), 1217-1228.

[47] Brown, J.Q., Bydlon, T.M., Richards, L.M., Yu, B., Kennedy, S.A., Geradts, J., Wilke, L.G., Junker, M.K., Gallagher, J., Barry, W.T. and Ramanujam, N. (2010). Optical assesssment of tumor resection margins in the breast. *IEEE Journal of Selected Topics in Quantum Electronics*, *16*(3), 530-544.

[48] Grzegorczyk, T. M., Meaney, P. M., & Paulsen, K. D. (2014). Microwave tomographic imaging for breast cancer chemotherapy monitoring. In *Antennas and Propagation, 2014 8th European Conference on* (pp. 702-703). IEEE.

[49] Yong, G., Ping, K. A. H., Chie, A. S. C., Ng, S. W., & Masri, T. (2015). Preliminary study of Forward-Backward Time-Stepping technique with edge-preserving regularization for object detection applications. In *BioSignal Analysis, Processing and Systems, 2015 International Conference on* (pp. 77-81). IEEE.

[50] Charbonnier, P., Blanc-Féraud, L., Aubert, G., & Barlaud, M. (1997). Deterministic edge-preserving regularization in computed imaging. *IEEE Transactions on Image Processing*, *6*(2), 298-311.

[51] Siang, K. C. and John, C. K. M. (2016). A review of lung cancer research in Malaysia. *Medical J Malaysia*, *71*(1), 70–78.

[52] Bray, F., Ferlay, J., Soerjomataram, I., Siegel, R. L., Torre, L. A., & Jemal, A. (2018). Global cancer statistics 2018: GLOBOCAN estimates of incidence and mortality worldwide for 36 cancers in 185 countries. *CA: A Cancer Journal for Clinicians*, *68*(6), 394–424.

[53] Tanaka, T., Takenaka, T., & He, S. (1999). An FDTD approach to the time-domain inverse scattering problem for an inhomogeneous cylindrical object. *Microwave and Optical Technology Letters*, *20*(1), 72-77.

[54] Johnson, J. E., Takenaka, T., & Tanaka, T. (2008). Two-dimensional time-domain inverse scattering for quantitative analysis of breast composition. *IEEE Transactions on Biomedical*

Engineering, *55*(8), 1941-1945.

[55] Elizabeth, M. A., Ping, K. A. H., Rajaee, N. B., & Moriyama, T. (2015). Chebyshev filter applied to an inversion technique for breast tumour detection. *International Journal of Research in Engineering & Technology*, *4*(6), 210–218.

[56] Qiu, D., Zhou, H., Takenaka, T., & Tanaka, T. (2006). Source-group method to speed up the reconstruction of objects from radar data by using the FBTS method. *Microwave and Optical Technology Letters*, *48*(1), 67-71.

[57] Moriyama, T., Yamaguchi, Y., Ping, K. A. H., Tanaka, T., & Takenaka, T. (2008). Parallel processing of forward-backward time-stepping method for time domain inverse scattering. *PIERS Online*, *4*(6), 695-700.

[58] Nawawi, J., Sahrani, S., Ping, K. A. H., Awang Mat, D. A., & Abang Zaidel, D. N. (2016). Iterative refinement in inverse scattering technique with median filter. In *Applied Electromagnetics, 2016 IEEE Asia-Pacific Conference on* (pp. 62-67). IEEE.

[59] Azman, A., Sahrani, S., Ping, K. A. H., & Mat, D. A. A. (2017). A New Approach for Solving Inverse Scattering Problems with Overset Grid Generation Method. *Telecommunication Computing Electronics and Control*, *15*(2), 820-828.

[60] Yee, K. (1966). Numerical solution of initial boundary value problems involving Maxwell's equations in isotropic media. *IEEE Transactions on Antennas and Propagation*, *14*(3), 302-307.

[61] Schneider, J. B. (2017). Understanding the finite-difference time-domain method. *School of Electrical Engineering and Computer Science Washington State University.* Retrieved from https://www.eecs.wsu.edu/~schneidj/ufdtd/ufdtd

[62] Chevalier, M. W., Luebbers, R. J., & Cable, V. P. (1997). FDTD local grid with material traverse. *IEEE Transactions on Antennas and Propagation*, *45*(3), 411-421.

[63] Samimi, A., & Simpson, J. J. (2016). Parallelization of 3-D Global FDTD Earth-Ionosphere Waveguide Models at Resolutions on the Order of∼ 1 km and Higher. *IEEE Antennas and Wireless Propagation Letters*, *15*, 1959-1962.

[64] Shankar, V., Mohammadian, A. H., & Hall, W. F. (1990). A time-domain, finite-volume treatment for the Maxwell equations. *Electromagnetics*, *10*(1-2), 127-145.

[65] Chen, Z., Fan, W., & Yang, S. (2016). Towards the wave-equation based explicit FDTD method without numerical instability. In *Computational Electromagnetics, 2016 IEEE International Conference on* (pp. 265-267). IEEE.

[66] Nieter, C., Cary, J. R., Werner, G. R., Smithe, D. N., & Stoltz, P. H. (2009). Application of Dey–Mittra conformal boundary algorithm to 3D electromagnetic modeling. *Journal of Computational Physics*, *228*(21), 7902-7916.

[67] Shi, R., Yang, H., & Gao, L. (2015). An Adaptive Time Step FDTD Method for Maxwell's Equations. *IEEE Antennas and Wireless Propagation Letters*, *14*, 1706-1709.

[68] Sarris, C. D. (2011). Extending the stability limit of the FDTD method with spatial filtering. *IEEE Microwave and Wireless Components Letters*, *21*(4), 176-178.

[69] Wei, X. K., Diamanti, N., Zhang, X., Annan, A. P., & Sarris, C. D. (2017). Spatially-filtered FDTD subgridding for ground penetrating radar numerical modeling. In *Advanced Ground Penetrating Radar, 2017 9th International Workshop on* (pp. 1-4). IEEE.

[70] Berenger, J. P. (1994). A perfectly matched layer for the absorption of electromagnetic waves. *Journal of Computational Physics*, *114*(2), 185-200.

[71] Reuter, C. E., Joseph, R. M., Thiele, E. T., Katz, D. S., & Taflove, A. (1994). Ultrawideband absorbing boundary condition for termination of waveguiding structures in FD-TD simulations. *IEEE Microwave and Guided Wave Letters*, *4*(10), 344-346.

[72] Salmasi, M., & Potter, M. E. (2016). FDTD discretization of Maxwell's equations on a face-centered-cubic grid. In *Antennas and Propagation, 2016 IEEE International Symposium on* (pp. 2017-2018). IEEE.

[73] Zygiridis, T. T., Kantartzis, N. V., & Tsiboukis, T. D. (2016). Development of optimized operators based on spherical-harmonic expansions for 3D FDTD schemes. *International Journal of Applied Electromagnetics and Mechanics*, *51*(s1), S57-S66.

[74] Van Londersele, A., De Zutter, D., & Ginste, D. V. (2016). A new hybrid implicit–explicit

FDTD method for local subgridding in multiscale 2-D TE scattering problems. *IEEE Transactions on Antennas and Propagation*, *64*(8), 3509-3520.

[75] Sandeep, S., & Gasiewski, A. J. (2012). Electromagnetic analysis of radiometer calibration targets using dispersive 3D FDTD. *IEEE Transactions on Antennas and Propagation*, *60*(6), 2821-2828.

[76] Wanjun, S., & Hou, Z. (2016). Analysis of electromagnetic wave propagation and scattering characteristics of plasma shealth via high order ADE-ADI FDTD. *Journal of Electromagnetic Waves and Applications*, *30*(10), 1321-1333.

[77] Mo, Q., Yeh, H., Lin, M., & Manocha, D. (2017). Outdoor sound propagation with analytic ray curve tracer and Gaussian beam. *The Journal of the Acoustical Society of America*, *141*(3), 2289-2299.

[78] Chen, J., Hao, G., & Liu, Q. H. (2017). Using the ADI-FDTD method to simulate graphene-based FSS at terahertz frequency. *IEEE Transactions on Electromagnetic Compatibility*, *59*(4), 1218-1223.

[79] Chungang, J., Lixin, G., & Wei, L. (2016). Parallel FDTD method for EM scattering from a rough surface with a target. In *Antennas, Propagation and EM Theory, 2016 11th International Symposium on* (pp. 569-572). IEEE.

[80] Kourtzanidis, K., Rogier, F., & Boeuf, J. P. (2015). ADI-FDTD modeling of microwave plasma discharges in air towards fully three-dimensional simulations. *Computer Physics Communications*, *195*, 49-60.

[81] Ireland, D., & Abbosh, A. (2013). Modeling human head at microwave frequencies using optimized Debye models and FDTD method. *IEEE Transactions on Antennas and Propagation*, *61*(4), 2352-2355.

[82] Luo, Z., Fan, D., Farmer, P., & Martin, G. (2017). Obtaining geologically conformable tomographic models through anisotropic-diffusion preconditioning. In *SEG Technical Program Expanded Abstracts 2017* (pp. 5691-5695). Society of Exploration Geophysicists.

[83] Blackledge, J., Hamalainen, T., & Joutsensalo, J. (2009). Inverse Scattering Solutions with

Applications to Electromagnetic Signal Processing. *ISAST Transactions on Electronics and Signal Processing*, *1*(4), 1-18.

[84] Shrestha, S. (2014). Image denoising using new adaptive based median filters. *Signal & Image Processing : An International Journal, 5*(4), 1-13.

[85] Zhu, J., Wen, J., & Zhang, Y. (2013). A new algorithm for SAR image despeckling using an enhanced lee filter and median filter. In *Image and Signal Processing*, *2013 6th International Congress on* (1, pp. 224-228). IEEE.

[86] Fan, W., Wang, K., Cayre, F., & Xiong, Z. (2015). Median filtered image quality enhancement and anti-forensics via variational deconvolution. *IEEE Transactions on Information Forensics and Security*, *10*(5), 1076-1091.

[87] Chou, H. H., Lin, H. W., & Chang, J. R. (2014). A sparsity-ranking edge-preservation filter for removal of high-density impulse noises. *AEU-International Journal of Electronics and Communications*, *68*(11), 1129-1135.

[88] Gir, R., Jain, L., & Rai, R. (2015). Speckle reduction of synthetic aperture radar images using median filter and savitzky-golay filter. *International Journal of Computer Applications*, *113*(11), 38-43.

[89] Zheng, Y., Zhang, X., Hou, B., & Liu, G. (2014). Using combined difference image and k-Means clustering for SAR image change detection. *IEEE Geoscience and Remote Sensing Letters*, *11*(3), 691-695.

[90] Hong, G., Zhang, A., Zhou, F., & Brisco, B. (2014). Integration of optical and synthetic aperture radar (SAR) images to differentiate grassland and alfalfa in Prairie area. *International Journal of Applied Earth Observation and Geoinformation*, *28*, 12-19.

[91] Zhao, Y., Liu, J. G., Zhang, B., Hong, W., & Wu, Y. R. (2015). Adaptive total variation regularization based SAR image despeckling and despeckling evaluation index. *IEEE Transactions on Geoscience and Remote Sensing*, *53*(5), 2765-2774.

[92] Agrawal, A., & Mishra, P. K. (2016). Restoration and de-noising of digital image based on non-linear diffusion filter for different type of noises. *International Journal of Engineering*

Science and Computing, *6*(10), 2608-2610.

[93] Moll, J., Kelly, T. N., Byrne, D., Sarafianou, M., Krozer, V., & Craddock, I. J. (2014). Microwave radar imaging of heterogeneous breast tissue integrating a priori information. *Journal of Biomedical Imaging*, *2014*(17), 1-10.

[94] Khare, C., & Nagwanshi, K. K. (2012). Image restoration technique with non linear filter. *International Journal of Advanced Science and Technology*, *39*, 67-74.

[95] Ma, Z., He, K., Wei, Y., Sun, J., & Wu, E. (2013). Constant time weighted median filtering for stereo matching and beyond. In *Proceedings of the IEEE International Conference on Computer Vision* (pp. 49-56).

[96] Pang, J., Zhang, S., & Zhang, S. (2016). A median filter based on the proportion of the image variance. In *Information Technology, Networking, Electronic and Automation Control Conference, IEEE* (pp. 123-127). IEEE.

[97] Agarwal, S., Singh, O. P., & Nagaria, D. (2017). Encrypted Image Denoising using Adaptive Weighted Median Filter. *Indian Journal of Science and Technology*, *10*(18), 1-8.

[98] Bhateja, V., Tripathi, A., & Gupta, A. (2014). An improved local statistics filter for denoising of SAR images. In *Recent Advances in Intelligent Informatics* (pp. 23-29). Springer, Cham.

[99] Rahimi, M., & Yazdi, M. (2015). A new hybrid algorithm for speckle noise reduction of SAR images based on mean-median filter and SRAD method. In *Pattern Recognition and Image Analysis, 2015 2nd International Conference on* (pp. 1-6). IEEE.

[100] Zhang, Q., Xu, L., & Jia, J. (2014). 100+ times faster weighted median filter (WMF). In *Proceedings of the IEEE Conference on Computer Vision and Pattern Recognition* (pp. 2830-2837).

[101] Kulkarni, R. N., & Bhaskar, P. C. (2014). Decision based median filter algorithm using resource optimized FPGA to extract impulse noise. *International Journal of Reconfigurable and Embedded Systems*, *3*(1), 1-10.

[102] Bhateja, V., Rastogi, K., Verma, A., & Malhotra, C. (2014). A non-iterative adaptive median filter for image denoising. In *Signal Processing and Integrated Networks, 2014 International*

Conference on (pp. 113-118). IEEE.

[103] Bhateja, V., Verma, A., Rastogi, K., Malhotra, C., & Satapathy, S. C. (2014). Performance improvement of decision median filter for suppression of salt and pepper noise. In *Advances in Signal Processing and Intelligent Recognition Systems* (pp. 287-297). Springer, Cham.

[104] Liang, J., He, W., Ji, D., & Wang, L. (2015). Image reconstruction algorithm for modified SART based on PM model. In *Computational Intelligence and Security, 2015 11th International Conference on* (pp. 175-178). IEEE.

[105] Correia, T., & Arridge, S. (2016). Patch-based anisotropic diffusion scheme for fluorescence diffuse optical tomography—part 1: technical principles. *Physics in Medicine & Biology*, *61*(4), 1439-1451.

[106] Tsiotsios, C., & Petrou, M. (2013). On the choice of the parameters for anisotropic diffusion in image processing. *Pattern Recognition*, *46*(5), 1369-1381.

[107] Ji, D., Hu, C., & Yang, H. (2015). Image reconstruction algorithm for in-line phase contrast imaging computed tomography with an improved anisotropic diffusion model. *Journal of X-ray Science and Technology*, *23*(3), 311-320.

[108] Guan, F., Ton, P., Ge, S., & Zhao, L. (2014). Anisotropic diffusion filtering for ultrasound speckle reduction. *Science China Technological Sciences*, *57*(3), 607-614.

[109] Zhang, X., Feng, X., Wang, W., Zhang, S., & Dong, Q. (2013). Gradient-based Wiener filter for image denoising. *Computers & Electrical Engineering*, *39*(3), 934-944.

[110] Xu, J., Jia, Y., Shi, Z., & Pang, K. (2016). An improved anisotropic diffusion filter with semi-adaptive threshold for edge preservation. *Signal Processing*, *119*, 80-91.

[111] Rafati, M., Arabfard, M., Zadeh, M. R. R., & Maghsoudloo, M. (2016). Assessment of noise reduction in ultrasound images of common carotid and brachial arteries. *IET Computer Vision*, *10*(1), 1-8.

[112] Mendrik, A. M., Vonken, E. J., Witkamp, T., Prokop, M., Van Ginneken, B., & Viergever, M. A. (2014). Using the fourth dimension to distinguish between structures for anisotropic diffusion filtering in 4D CT perfusion scans. In *International Workshop on Spatio-temporal*

Image Analysis for Longitudinal and Time-Series Image Data (pp. 79-87). Springer, Cham.

[113] Abdallah, M. B., Malek, J., Azar, A. T., Belmabrouk, H., Monreal, J. E., & Krissian, K. (2016). Adaptive noise-reducing anisotropic diffusion filter. *Neural Computing and Applications*, *27*(5), 1273-1300.

[114] Garg, A., & Goyal, K. (2014). Regularization Methods to Solve Various Inverse Problems. *International Journal of Science and Research*, *3*(8), 1840–1845.

[115] Niu, S., Gao, Y., Bian, Z., Huang, J., Chen, W., Yu, G., Liang, Z. and Ma, J. (2014). Sparse-view x-ray CT reconstruction via total generalized variation regularization. *Physics in Medicine & Biology*, *59*(12), 2997–3017.

[116] Zhuge, X., Palenstijn, W. J., & Batenburg, K. J. (2016). TVR-DART: a more robust algorithm for discrete tomography from limited projection data with automated gray value estimation. *IEEE Transactions on Image Processing*, *25*(1), 455-468.

[117] Sanders, T., Gelb, A., Platte, R. B., Arslan, I., & Landskron, K. (2017). Recovering fine details from under-resolved electron tomography data using higher order total variation ℓ1 regularization. *Ultramicroscopy*, *174*, 97-105.

[118] Mehranian, A., Rahmim, A., Ay, M. R., Kotasidis, F., & Zaidi, H. (2013). An ordered-subsets proximal preconditioned gradient algorithm for edge-preserving PET image reconstruction. *Medical Physics*, *40*(5), 1-14.

[119] Gerace, I., Martinelli, F., & Tonazzini, A. (2014). Demosaicing of noisy color images through edge-preserving regularization. In *Computational Intelligence for Multimedia Understanding, 2014 International Workshop on* (pp. 1-5). IEEE.

[120] Gong, G., Zhang, H., & Yao, M. (2014). Construction model for total variation regularization parameter. *Optics Express*, *22*(9), 10500-10508.

[121] Gu, X., & Gao, L. (2009). A new method for parameter estimation of edge-preserving regularization in image restoration. *Journal of Computational and Applied Mathematics*, *225*(2), 478-486.

[122] Bahy, R. M., Salama, G. I., & Mahmoud, T. A. (2014). Adaptive regularization-based super

resolution reconstruction technique for multi-focus low-resolution images. *Signal Processing*, *103*, 155-167.

[123] Cho, W., Seo, S., & You, J. (2014). Edge-preserving denoising method using variation approach and gradient distribution. In *Big Data and Smart Computing, 2014 International Conference on* (pp. 139-144). IEEE.

[124] Boudaoud, A., Burian, A., Borowska-Wykręt, D., Uyttewaal, M., Wrzalik, R., Kwiatkowska, D., & Hamant, O. (2014). FibrilTool, an ImageJ plug-in to quantify fibrillar structures in raw microscopy images. *Nature Protocols*, *9*(2), 457-463.

[125] Chen, L. Y., Pan, M. C., & Pan, M. C. (2013). Flexible near-infrared diffuse optical tomography with varied weighting functions of edge-preserving regularization. *Applied Optics*, *52*(6), 1173-1182.

[126] Jung, J. E., & Lee, S. J. (2015). Edge-preserving iterative reconstruction for transmission tomography using convex weighted median priors. In *Nuclear Science Symposium and Medical Imaging Conference, 2015 IEEE* (pp. 1-3). IEEE.

[127] Rudin, L. I., Osher, S., & Fatemi, E. (1992). Nonlinear total variation based noise removal algorithms. *Physica D: Nonlinear Phenomena*, *60*(1-4), 259-268.

[128] Zhang, J., Liu, S., Xiong, R., Ma, S., & Zhao, D. (2013). Improved total variation based image compressive sensing recovery by nonlocal regularization. In *Circuits and Systems, 2013 IEEE International Symposium on* (pp. 2836-2839). IEEE.

[129] Tourbier, S., Bresson, X., Hagmann, P., Thiran, J. P., Meuli, R., & Cuadra, M. B. (2014). Efficient total variation algorithm for fetal brain MRI reconstruction. In *International Conference on Medical Image Computing and Computer-Assisted Intervention* (pp. 252-259). Springer, Cham.

[130] Matakos, A., Ramani, S., & Fessler, J. A. (2013). Accelerated edge-preserving image restoration without boundary artifacts. *IEEE Transactions on Image Processing*, *22*(5), 2019-2029.

[131] Bhujle, H., & Chaudhuri, S. (2014). Novel speed-up strategies for non-local means denoising

with patch and edge patch based dictionaries. *IEEE Transactions on Image Processing*, *23*(1), 356-365.

[132] Chan, R. H., Liang, H., Wei, S., Nikolova, M., & Tai, X. C. (2015). High-order total variation regularization approach for axially symmetric object tomography from a single radiograph. *Inverse Problems & Imaging*, *9*(1), 55–77.

[133] Dong, W., Zhang, L., Shi, G., & Li, X. (2013). Nonlocally centralized sparse representation for image restoration. *IEEE Transactions on Image Processing*, *22*(4), 1620-1630.

[134] Zhang, K., Tao, D., Gao, X., Li, X., & Xiong, Z. (2015). Learning multiple linear mappings for efficient single image super-resolution. *IEEE Transactions on Image Processing*, *24*(3), 846-861.

[135] Khan, A., Waqas, M., Ali, M. R., Altalhi, A., Alshomrani, S., & Shim, S. O. (2016). Image de-noising using noise ratio estimation, K-means clustering and non-local means-based estimator. *Computers & Electrical Engineering*, *54*, 370-381.

[136] Jia, L., Li, M., Zhang, P., Wu, Y., & Zhu, H. (2016). SAR image change detection based on multiple kernel K-means clustering with local-neighborhood information. *IEEE Geoscience and Remote Sensing Letters*, *13*(6), 856-860.

[137] Salucci, M., Sartori, D., Anselmi, N., Randazzo, A., Oliveri, G., & Massa, A. (2013). Imaging buried objects within the second-order Born approximation through a multiresolution-regularized inexact-Newton method. In *Electromagnetic Theory, Proceedings of 2013 URSI International Symposium on* (pp. 116-118). IEEE.

[138] Salucci, M., Rocca, P., Oliveri, G., & Massa, A. (2014). An innovative Frequency Hopping multi-zoom inversion strategy for GPR subsurface imaging. In *Ground Penetrating Radar, 2014 15th International Conference on* (pp. 619-623). IEEE.

[139] Salucci, M., Poli, L., Anselmi, N., & Massa, A. (2017). Multifrequency particle swarm optimization for enhanced multiresolution GPR microwave imaging. *IEEE Transactions on Geoscience and Remote Sensing*, *55*(3), 1305-1317.

[140] Dixit, A. (2014). Adaptive Kmeans Clustering for Color and Gray Image [Source Code].

Retrieved from https://www.mathworks.com/matlabcentral/fileexchange/45057-adaptive-kmeans-clustering-for-color-and-gray-image

[141] Bhatia, S. K. (2004). Adaptive K-Means Clustering. In *FLAIRS Conference* (pp. 695-699).

[142] Grove, O., Berglund, A. E., Schabath, M. B., Aerts, H. J., Dekker, A., Wang, H., & Gillies, R. J. (2015). Data from: Quantitative computed tomographic descriptors associate tumour shape complexity and intratumor heterogeneity with prognosis in lung adenocarcinoma. *The Cancer Imaging Archive*.

[143] Anderson, V., & Rowley, J. (1998). Tissue dielectric properties calculator. *Clayton, Victoria, Australia: Telstra Research Laboratories*.

[144] Holman, B. F., Cuplov, V., Millner, L., Hutton, B. F., Maher, T. M., Groves, A. M., & Thielemans, K. (2015). Improved correction for the tissue fraction effect in lung PET/CT imaging. *Physics in Medicine & Biology*, *60*(18), 7387-7402.

[145] Hartsgrove, G., Kraszewski, A., & Surowiec, A. (1987). Simulated biological materials for electromagnetic radiation absorption studies. *Bioelectromagnetics: Journal of the Bioelectromagnetics Society, The Society for Physical Regulation in Biology and Medicine, The European Bioelectromagnetics Association*, *8*(1), 29-36.

[146] Chen, X., Wang, H., Zhao, B., & Shi, X. (2009). Lung ventilation functional monitoring based on electrical impedance tomography. *Transactions of Tianjin University*, *15*(1), 7-12.

[147] Ketata, M., Dhieb, M., Hmida, G. B., Ghariani, H., & Lahiani, M. (2015). UWB pulse propagation in human tissue: Comparison between Gaussian and square waves shape. In *Sciences and Techniques of Automatic Control and Computer Engineering, 2015 16th International Conference on* (pp. 158-162). IEEE.

[148] Babarinde, O. J., Jamlos, M. F., Soh, P. J., Schreurs, D. P., & Beyer, A. (2016). Microwave imaging technique for lung tumour detection. In *Microwave Conference, 2016 German* (pp. 100-103). IEEE.

[149] Wang, J. R., Sun, B. Y., Wang, H. X., Pang, S., Xu, X., & Sun, Q. (2014). Experimental study of dielectric properties of human lung tissue in vitro. *Journal of Medical and Biological*

Engineering, *34*(6), 598-604.

[150] Nawawi, J., Sahrani, S., & Ping, K. A. H. (2017). Automated Scaling Region of Interest (AS-ROI) in inverse scattering method for tomographic image reconstruction. In *Progress in Electromagnetics Research Symposium-Fall, 2017* (pp. 1648-1653). IEEE.

[151] Joseph, E. J., Ping, K. A. H., Kipli, K., Awang Mat, D. A., Sahrani, S., Abang Zaidel, D. N., ... & Marhaban, M. H. (2017). Integration of Image Segmentation Method in Inverse Scattering for Brain Tumour Detection. *Progress in Electromagnetics Research*, *61*, 111-122.

[152] Komarov, V., Wang, S., & Tang, J. (2005). Permittivity and measurements. *Encyclopedia of RF and Microwave Engineering*. Hoboken, N.J.: John Wiley & Sons, Inc.

[153] Lee, H., & Um, S. W. (2015). Probability of lung cancer based on the size threshold and volume-doubling time for lung nodules detected in low-dose CT screening. *Annals of Translational Medicine*, *3*(2), 1-2.

APPENDIX

LIST OF AWARD AND PUBLICATIONS

Award:

1. Silver Medal in UNIMAS Innovative and Technology Exposition 2017 for project titled "Automated scaling region of interest (AS-ROI) in inverse scattering method for tomographic image reconstruction".

Conference Publications:

1. Nawawi, J., Sahrani, S., Ping, K. A. H., Awang Mat, D. A., & Abang Zaidel, D. N. (2016). Iterative refinement in inverse scattering technique with median filter. In *Applied Electromagnetics, 2016 IEEE Asia-Pacific Conference on* (pp. 62-67). IEEE.
2. Nawawi, J., Sahrani, S., & Ping, K. A. H. (2017). Automated Scaling Region of Interest (AS-ROI) in inverse scattering method for tomographic image reconstruction. In *Progress in Electromagnetics Research Symposium-Fall, 2017* (pp. 1648-1653). IEEE.

Journal Publication:

1. Nawawi, J., Sahrani, S., & Ping, K. A. H. (2018). Automated Scaling Region of Interest with Iterative Edge Preserving in Forward-Backward Time-Stepping. *Progress in Electromagnetics Research*, 67, 177-188.